Atomic modification of graphene on silicon carbide: adsorption and intercalation

by

Amy Chenge Qu

B.Sc., University of Toronto, 2014

M.S., Columbia University, 2015

A THESIS SUBMITTED IN PARTIAL FULFILLMENT
OF THE REQUIREMENTS FOR THE DEGREE OF

Doctor of Philosophy

in

THE FACULTY OF GRADUATE AND POSTDOCTORAL STUDIES
(Physics)

The University of British Columbia
(Vancouver)

August 2021

The following individuals certify that they have read, and recommend to the Faculty of Graduate and Postdoctoral Studies for acceptance, the thesis entitled:

Atomic modification of graphene on silicon carbide: adsorption and intercalation

submitted by **Amy Chenge Qu** in partial fulfillment of the requirements for the degree of **Doctor of Philosophy** in **Physics**.

Examining committee:

Andrea Damascelli, Professor, Physics and Astronomy, University of British Columbia

Supervisor

Sarah A. Burke, Associate Professor, Physics and Astronomy, Chemisty, University of British Columbia

Supervisory committee member

Andrew MacFarlane, Professor, Chemistry, University of British Columbia

University examiner

Alireza Nojeh, Professor, Electrical and Computer Engineering, University of British Columbia

University examiner

Abhay N. Pasupathy, Associate Professor, Physics, Columbia University

External examiner

Additional supervisory committee members:

Marcel Franz, Professor, Physics and Astronomy, University of British Columbia

Supervisory committee member

David J. Jones, Professor, Physics and Astronomy, University of British Columbia

Supervisory committee member

Abstract

Graphene, the first truly 2D material to be isolated, is host to a wealth of remarkable properties. It can be modified in a variety of ways—strained, twisted, stacked, placed on a substrate, decorated with adatoms, etc.—to further enhance these properties or introduce new ones. In this thesis, we use several complementary surface characterization techniques to study two methods of modifying epitaxial graphene on a silicon carbide (SiC) substrate via the addition of other atoms.

In the first method, we induce the Kekulé distortion—a periodic distortion of the bonds in graphene—using a small number of lithium atoms ($< 0.2\%$ monolayer) adsorbed on the graphene surface. Mediated by the graphene, the adatoms interact over large distances, leading to symmetry breaking between graphene unit cells and a $(\sqrt{3} \times \sqrt{3})$ R30° superstructure. Using angle-resolved photoemission spectroscopy (ARPES), we observe the formation of the superstructure in the appearance of a new Dirac cone in the centre of the Brillouin zone due to band folding. The same superstructure was confirmed by the appearance of new spots in low-energy electron diffraction (LEED) experiments. ARPES data also reveals a gap opening $2\Delta_{kek} = (238 \pm 3)$ meV at the Dirac point. Using a Monte Carlo toy model, we study the importance of deposition parameters in the formation of the Kekulé phase. Finally, we show that this phase is generic to other graphene systems, regardless of charge carrier type or density.

In the second method, we intercalate copper atoms between the graphene and the SiC substrate by contacting it with copper paste and annealing in vacuum. Using scanning tunnelling microscopy (STM), we observe the

formation of 2.2 Å tall islands under the graphene, which modify the observed graphene/SiC superstructure from SiC (6×6) to SiC $(6\sqrt{3} \times 6\sqrt{3})$ R30°. The same periodicity is observed in LEED, and the intercalation of copper is confirmed by the appearance of additional bands in ARPES. The resulting material is stable for years even in ambient conditions.

These two methods produce simple, robust new phases in graphene grown on a wafer-sized insulating substrate, suggesting great promise for the eventual widespread use of graphene in everyday electronics.

Lay Summary

Graphene is a one-atom-thick layer of common graphite. It has many remarkable properties: strong, flexible, light, an excellent conductor of heat and electricity, and almost transparent. The behaviour of its electrons is particularly interesting, similar to massless particles moving at the speed of light. Since its Nobel-Prize-winning experimental realization in 2004, physicists have tried to modify graphene in a variety of ways to induce even more interesting properties: straining, twisting, stacking, placing on a substrate, etc. In this thesis, we modify graphene on a silicon carbide substrate by adding lithium or copper atoms and study the electronic behaviour of the resulting materials. A small number of lithium atoms deposited on the graphene produces a large-scale periodic distortion of the graphene bonds, while copper between the graphene and the substrate forms ordered islands on the sample surface. These results show great promise for the widespread use of graphene in electronics.

Preface

In Chapter 4, the acceptance tests for the ARPES/SPM system were performed by E. Schrenk and D. Stahl at UBC on behalf of Scienta Omicron GmbH, with assistance from A. C. Qu, J. Kim, and S. A. Burke. The additional tests were performed by A. C. Qu, J. Kim, E. Mårsell, J. Bannies, and T. Matthé, with support from E. Schrenk and D. Stahl. The ARPES and UPS data were analyzed by A. C. Qu and T. Matthé. The ZrSiSe sample was grown by M. Oudah at UBC. The dual-source evaporator was designed and built by A. C. Qu with input from M. Schneider and J. Kim. The instrument was commissioned by S. A. Burke and D. A. Bonn.

Chapter 5 is based on the manuscript in preparation *Global density wave formation in graphene via local symmetry-breaking* by A. C. Qu *et al.* (2021). The graphene samples were grown by S. Link and U. Starke at the Max Planck Institute for Solid State Research in Stuttgart, Germany. ARPES and LEED experiments were performed by A. C. Qu and P. Nigge at UBC, with support from G. Levy, M. Michiardi, M. Schneider, and S. Zhdanovich. The ARPES data was analyzed by A. C. Qu with input from P. Nigge, C. Gutiérrez, and G. Levy. The LEED data was analyzed by C. Gutiérrez. The theoretical modelling was performed by A. C. Qu and T. Matthé. The manuscript was written by A. C. Qu, C. Gutiérrez, and G. Levy with input from all authors. The project was supervised and managed by C. Gutiérrez and A. Damascelli.

In Chapter 6, the graphene samples were grown by S. Link and U. Starke at MPI Stuttgart. The STM experiments were performed by A. C. Qu, J. Kim, E. Mårsell, P. Nigge, and G. Tom; the ARPES experiments were

performed by A. C. Qu and J. Bannies; and the LEED experiments were performed by A. Tully and R. Greenwood, all at UBC. The XPS experiments were performed by R. Sutarto at the Canadian Light Source in Saskatoon, Canada. All data was analyzed by A. C. Qu. The project was supervised and managed by S. A. Burke and D. A. Bonn.

Table of Contents

List of Tables

List of Figures

Glossary

2DEG	2D electron gas
AFM	Atomic force microscope/microscopy
ARPES	Angle-resolved photoemission spectroscopy
ARTOF	Angle-resolved time-of-flight
BLG	Bilayer graphene
BZ	Brillouin zone
CDW	Charge density wave
CO	Carbon monoxide
CVT	Chemical vapour transport
DOS	Density of states
hBN	Hexagonal boron nitride
H.c.	Hermitian conjugate
HOPG	Highly oriented pyrolytic graphite
JT	Joule-Thomson
LDOS	Local density of states
LEED	Low-energy electron diffraction

LHe	Liquid helium
LL	Landau level
LN_2	Liquid nitrogen
MDC	Momentum distribution curve
MLG	Monolayer graphene
PBN	Pyrolytic boron nitride
PES	Photoemission spectroscopy
QHE	Quantum Hall effect
QPI	Quasiparticle interference
SDW	Spin density wave
SiC	Silicon carbide
SPM	Scanning probe microscopy
STM	Scanning tunnelling microscope/microscopy
STS	Scanning tunnelling spectroscopy
TEM	Transmission electron microscopy
TSP	Titanium sublimation pump
UPS	Ultraviolet photoelectron spectroscopy
VHS	Van Hove singularity
WKB	Wentzel-Kramers-Brillouin
XPS	X-ray photoelectron spectroscopy
ZLG	Zero-layer graphene

Acknowledgments

This thesis is the culmination of the biggest project I have ever undertaken, and it would never have happened without the support of many people.

First and foremost, my parents: thank you for sacrificing so much to bring me to Canada so that I could have more freedom to pursue what I wanted. Thank you for always loving me, supporting me, believing in me, and being on my side no matter what.

Next, Neil Janssen, Henri van Bemmel, Robert Staruch, Joseph Thywissen, and the many other mentors in my life who led me to grad school in the first place: thank you for raising me to become the scientist I am now.

The majority of the work described in this thesis was done in my two research groups at UBC, ARPES and LAIR. Both groups taught me, helped me, and encouraged me throughout my grad school journey. Thank you.

In particular from the ARPES group, Andrea Damascelli: thank you for giving me so much freedom and support to drive my own project. Thank you for giving me room to explore and grow. Giorgio Levy: thank you for all your help with my experiments over the years. Christopher Gutiérrez: thank you for being patient with me and always making time to discuss science with me. Michael Schneider: thank you for teaching me almost everything I know about UHV design.

And from LAIR, Sarah Burke: thank you for the most special research group I've ever had the pleasure of being a part of. Thank you for recognizing that my life is more than grad school, for encouraging me to ask "stupid" questions, for your graciousness when I make mistakes. Jisun Kim: thank you for teaching me so much about STM, for helping me with Tesla every

single step of the way, and for always listening to me. James Day: thank you for being someone I can always go to. Brandon Stuart: thank you for your company on the long thesis-writing journey. Tiffany Matthé: thank you for being the best summer student I could have asked for, despite the circumstances. And Crossword Crew: thank you for some of the best (worst?) lunch breaks ever at Lamb Data U.

I am also grateful for many other people I was able to meet through grad school. Eike Schrenk and Dirk Stahl: thank you for always patiently answering all my questions about Tesla. I'm looking forward to working with you. Marcel Franz: thank you for teaching me everything I know about the theory of graphene. Michelle Ng: thank you for always making time for me, and for all the IKEA runs, late night chats, and food adventures (potato emoji). David Jones and Jennifer Stamp: thank you for being two of the kindest and most generous people I've ever met. Thank you for sharing Hobbes's love with me. Hobbes Jones: thank you for all your love. You are the goodest boy in the whole world.

Of course there are also my friends from outside of school. Charissa Poon: remember when we met at the TOPS orientation in Grade 8 and you were wearing that purple sweater? Thank you for being my best friend, for growing with me in all my science years, and for always keeping in touch even though we live so far apart. My Art Club friends: thank you for giving me a space to become an artist. My art was able to come so far because of you all. I wish we had more time together.

And finally, Pascal Nigge, *lieber* Pascal: thank you for being there with me from beginning to end. Thank you for always helping me and encouraging me with everything from ARPES experiments to scuba diving. I am braver and stronger because I met you. I could never have done this without you.

For my parents

Chapter 1

Introduction

Graphene, a single layer of common graphite, became the first 2D material to be isolated and characterized in 2004 [1]. Theorists have discussed "2D graphite" since as early as the 1940s [2, 3, 4, 5, 6], but it was believed at the time that truly 2D materials were inherently unstable and could not exist at finite temperatures [7, 8, 9, 10]. While ultrathin graphite films and even monolayer graphene had been observed by transmission electron microscopy (TEM) even before 2004 [11, 12, 13, 14], Novoselov *et al.* were the first to reliably isolate and identify graphene single crystals large enough to permit detailed studies of their properties [1], many of which would eventually prove to be quite remarkable. For this work, Novoselov and Geim were awarded the 2010 Nobel Prize in Physics, and widespread interest in graphene has continued to this day. Many excellent review articles about graphene and its properties have been published over the years [15, 16, 17, 18, 19], but a brief overview will be provided in this chapter.

Graphene consists of a lattice of carbon atoms arranged in a honeycomb structure (Figure 1.1), which arises from hybridization of the carbon atom orbitals (Figure 1.2). Each carbon atom has six electrons in the configuration $1s^2 2s^2 2p^2$. The $1s$ electrons are tightly bound; the $2s$ and $2p$ orbitals (Figure 1.2(a)) hybridize to form three sp^2 orbitals and one p_z orbital (Figure 1.2(b)). The in-plane sp^2 orbitals are responsible for the σ bonds of the honeycomb lattice; the out-of-plane p_z orbital forms the π and π^* bands

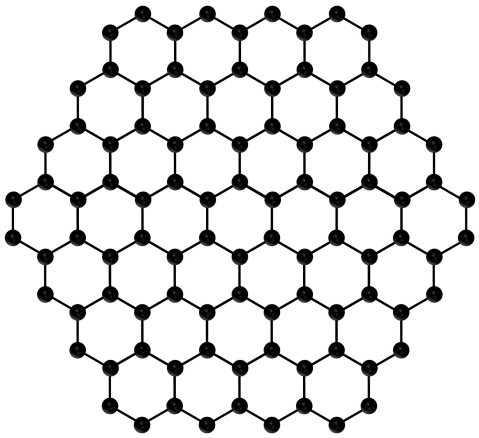

Figure 1.1: Atomic structure of graphene. Graphene, a single layer of graphite, is made of carbon atoms (black circles) arranged in a 2D honeycomb lattice. The σ bonds between adjacent atoms are indicated by the black lines.

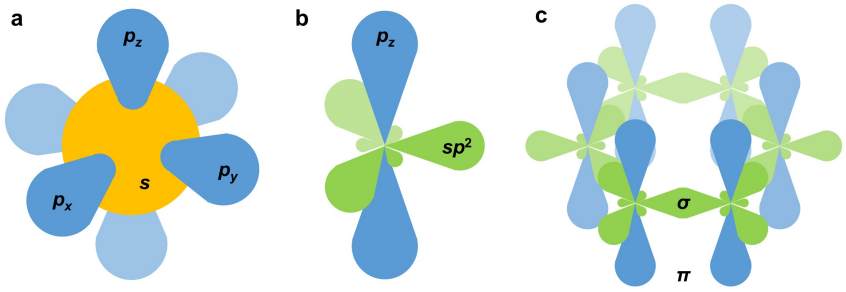

Figure 1.2: Carbon orbitals in graphene. (a) Unhybridized $2s$ (yellow) and $2p$ (blue) orbitals. **(b)** In graphene, the $2s$, $2p_x$, and $2p_y$ orbitals of the carbon atoms hybridize to form three sp^2 orbitals (green). The p_z orbital (blue) remains unhybridized. **(c)** The in-plane sp^2 orbitals form the σ bonds responsible for the characteristic honeycomb structure of graphene, while the out-of-plane p_z orbitals form the π and π^* bands giving rise to most of graphene's notable electronic properties.

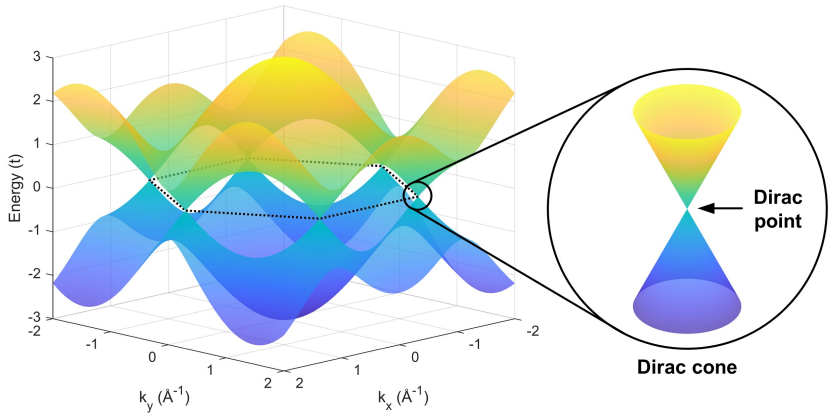

Figure 1.3: The Dirac cones of graphene. The theoretical bandstructure of graphene is calculated using a tight-binding model. The valence and conduction bands meet at six points in the $E = 0$ plane (indicated by the hexagon). Near these points, the dispersion is linear, giving rise to the characteristic Dirac cones of graphene.

which are responsible for most of graphene's notable electronic properties (Figure 1.2(c)).

The most well-known of these properties is the distinctive bandstructure of graphene (theoretically calculated in Figure 1.3), in which its valence and conduction bands meet at six points at the Fermi level. The dispersion relation is linear near these points, indicating that electrons propagating in graphene behave as massless particles [2, 5]. Thus they are described by the 2D analog of the Dirac equation of relativistic quantum mechanics rather than the non-relativistic Schrödinger equation [18], hence the names "Dirac cones" for the linear dispersion and "Dirac points" for the points at the Fermi level. In Chapter 2, we discuss how this dispersion arises in a simple tight-binding model.

This pseudo-relativistic behaviour of the electrons directly leads to the observation of an anomalous quantum Hall effect (QHE) in graphene [20, 21]. In the typical QHE, the Hall conductivity becomes quantized in the presence of a magnetic field [22]. The effect in graphene is anomalous in that the quantization is offset by half a step and multiplied by 4 compared to the

typical QHE. The half-step offset is a consequence of the half-filled zeroth Landau level (LL) at the Fermi level, which is not present in a typical 2D electron gas (2DEG), while the factor of 4 is due to spin and lattice degeneracies [20, 21].

Another consequence of the bandstructure and 2D nature of graphene is that its charge carrier type and concentration can be tuned simply by applying a gate voltage. In addition, the charge carriers have extremely high mobility, reportedly up to 10^6 cm^2/V$\cdot$s. [1].

Besides its electronic properties, graphene also exhibits many remarkable physical properties. It has a breaking strength of $\sim$40 N/m, more than 100 times stronger than steel, with a Young's modulus of $\sim$1 TPa [23]. Yet it can also be folded, or stretched elastically by up to 20% [23, 24]. It is almost optically transparent. It has an in-plane thermal conductivity of $\sim$5000 W/m/K, about 10 times better than copper [25].

In the 2004 work by Novoselov *et al.*, graphene was isolated by micromechanical cleavage, in which thin layers of highly oriented pyrolytic graphite (HOPG) were peeled apart using adhesive tape and deposited on a silicon substrate [1]. This method produces high-quality, free-standing graphene with few defects, but the crystals are small ($<$ 1 mm). As early as the 1970s, however, van Bommel *et al.* had grown graphitic layers epitaxially on silicon carbide (SiC) substrates [26], and later, Berger *et al.* would grow few-layer graphene in a similar way [27, 28]. This was particularly key as it demonstrated the feasibility of growing large graphene/SiC wafers for electronic applications. Today monolayer graphene is routinely grown on SiC [29] (for a description of the process, see Section 3.5.1), and these samples are used for the work described in this thesis.

As the characteristics of graphene became better understood, scientists moved on to modifying graphene in a variety of ways in order to alter its properties or induce new ones (Figure 1.4). The most straightforward modifications involve manipulating the graphene itself: straining, folding, stacking multiple layers, and so on.

So-called "magic-angle" twisted bilayer graphene recently attracted a great deal of attention in the condensed matter community. By stacking

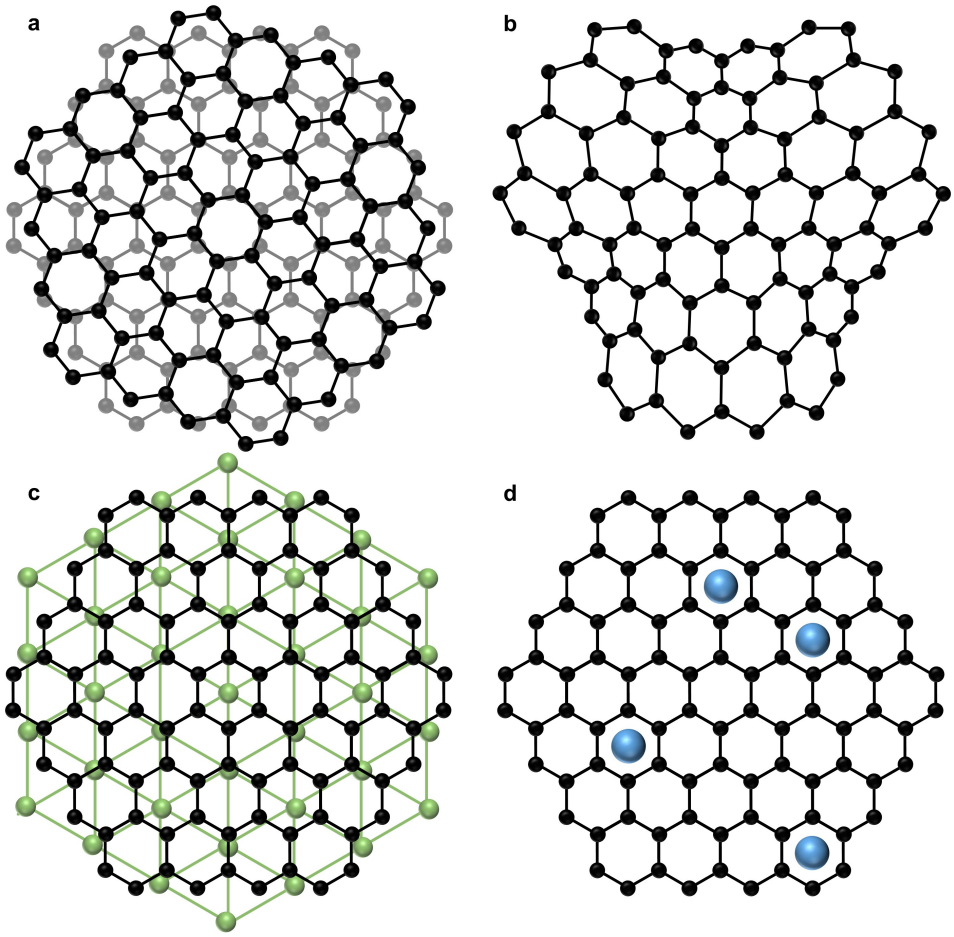

Figure 1.4: Ways to modify graphene. **(a)** Two graphene flakes are twisted with respect to each other and stacked to form a large moiré pattern. **(b)** Triaxial strain is applied to a graphene flake. Such strain patterns result in the appearance of pseudomagnetic fields in graphene [30]. **(c)** A graphene flake is stacked on a SiC substrate (green). The graphene lattice is rotated with respect to the SiC, and the lattice constant is slightly mismatched. **(d)** Several atoms are adsorbed on a graphene flake.

two sheets of graphene twisted slightly with respect to each other, large superlattices are generated by the resulting moiré patterns. This results in the formation of flat bands and thus an increase in the density of states (DOS) near the Fermi level, leading to a superconducting transition with a critical temperature of ∼1.7 K [31].

In the "magic-angle" work, Cao *et al.* prepared their twisted bilayer graphene by manually rotating the layers and stacking them together [31]. A year later, Chen *et al.* were able to achieve atomically precise control of the twist angle by folding and unfolding graphene nanoislands on graphite [32].

Due to its high strength and flexibility, graphene can be strained significantly without breaking. When the strain pattern follows certain geometries, pseudomagnetic fields can be generated, causing the graphene electrons to behave as if in the presence of a magnetic field [30, 33]. In an analog of the QHE, such strain patterns lead to the evolution of the Dirac cones into flat LLs at distinct energies increasing with $\sqrt{N}$, where N is the index of the LL. Experimentally, such strain patterns can be achieved by using select substrates: Levy *et al.* observed the formation of LLs in graphene nanobubbles formed by growth on Pt(111) [34], while Nigge *et al.* used triangular nanoprisms in SiC formed by the absence of a single layer in the substrate [35]. The effects of strain-induced pseudomagnetic fields have also been observed in artificial graphene: Gomes *et al.* manipulated single carbon monoxide (CO) molecules on Cu(111) to build a purely electronic honeycomb lattice, and when triaxial strain was "applied" by moving the CO molecules, the formation of LLs was observed [36]. Rechtsman *et al.*, meanwhile, used a strained honeycomb photonic lattice to generate "photonic LLs" in real space [37].

Besides strain, other effects can also be generated in graphene by judicious choice of substrate. A hexagonal boron nitride (hBN) substrate, for example, has been theorized to induce symmetry breaking between the two sublattices of graphene, leading to a bandgap opening at the Dirac point [38, 39]. Such a gap opening has also been predicted [40] and observed [41] in graphene on SiC substrates, as well as in artificial graphene made of cold atoms in a honeycomb optical lattice [42]. Engineering a gap opening in graphene,

which is not gapped in its pristine form, is particularly key for realizing its widespread use in electronics as a semiconductor.

The graphene substrate can also play a role through proximity effects. By stacking graphene on few-layer semiconducting tungsten disulphide, for example, its weak spin-orbit coupling [43] can be increased by three orders of magnitude [44]. Graphene on the magnetic insulator europium oxide, on the other hand, is predicted to result in spin polarization of the π bands [45]. Superconductivity has also been predicted for graphene on small superconducting islands [46]; while not a substrate, superconducting electrodes have already been observed to produce supercurrents in graphene [47, 48, 49, 50].

Graphene can even interact with defects in the substrate. Gutiérrez *et al.*, for example, observed that the vacancies in a Cu(111) substrate induced the Kekulé distortion in graphene, a phase in which the carbon-carbon bonds are periodically distorted (for more details, see Section 5.1) [51].

Yet another group of methods for modifying graphene is the addition of new atoms. These can be adsorbed on top of the graphene (adatoms), intercalated under the graphene on a substrate, or sandwiched between multiple layers of graphene. A common effect of these atoms is a shifting of the Fermi level away from the Dirac point due to charge-transfer doping: for example, intercalating hydrogen below graphene on SiC causes the graphene to become hole-doped [52], while depositing lithium on top leads to electron doping [53, 54, 55]. Very high doping levels are particularly interesting, since the Dirac cones of graphene are connected by saddle points, resulting in a Van Hove singularity (VHS) in the DOS. Theory suggests that bringing these flat bands to the Fermi level may result in various correlated phases such as superconductivity and charge or spin density waves (CDWs or SDWs) [56, 57, 58, 59]. Although such phases have not yet been observed, such highly-doped regimes have been achieved using intercalated gadolinium [60] or ytterbium [61, 62], as well as a combination of intercalated calcium plus adsorbed calcium and potassium [63].

Superconductivity may also arise through the addition of these atoms. Lithium adatoms, for example, have been predicted to induce superconduc-

tivity in graphene through enhancement of the electron-phonon coupling [64], and this was later experimentally observed below ∼5.9 K [53]. Calcium-intercalated bilayer graphene is also superconducting below ∼4 K [65, 66].

A number of other interesting physical phenomena have been observed as a result of atomic modification. Hydrogen atoms adsorbed on graphene on Ir(111), for example, prefer certain parts of the graphene/Ir(111) moiré, leading to a gap opening at the Fermi level [67, 68]. Meanwhile, a dilute amount of indium or thallium adatoms have been predicted to produce a topological phase in graphene [69]. While such a phase has not yet been observed, both indium and thallium adatoms have been found to be efficient scatterers on graphene [70, 71].

In this thesis, we explore the use of lithium and copper in modifying graphene on a SiC substrate. As previously discussed, a monolayer of lithium adatoms on graphene leads to increased electron doping and signatures of superconductivity [53]. In Chapter 5, we study a different regime of lithium on graphene: using an extremely dilute amount of lithium adatoms ($< 0.2\%$ of a monolayer), we are able to induce the Kekulé bond distortion and observe the resulting superstructure. In Chapter 6, we intercalate copper between the graphene and SiC, leading to the formation of ordered islands on the sample surface. Additionally, we also discuss a tight-binding model of the graphene bandstructure (Chapter 2), the tools and techniques used (Chapter 3), and the testing and characterization of a new instrument capable of combining several of these techniques (Chapter 4).

Chapter 2

Tight binding model of graphene

Even prior to its experimental realization, graphene was popular among theorists for its simplicity. Many key features of the graphene bandstructure, particularly its characteristic Dirac cones, can be predicted using only a simple tight-binding model with a single electron (neglecting spin). In this chapter, we derive such a model and discuss the effects of introducing terms related to symmetry breaking in the sublattice and valley degrees of freedom [72, 73, 74]. The experimental manifestations of these terms will be discussed in Chapter 5.

2.1 Pristine graphene

The honeycomb lattice can be represented by a 2-atom basis on a triangular lattice (Figure 2.1). In pristine graphene, the two carbon atoms (A and B) are equivalent. The primitive lattice vectors are

$$\begin{aligned} \boldsymbol{a}_1 &= \alpha(\sqrt{3}, 0) \\ \boldsymbol{a}_2 &= \alpha\left(\frac{\sqrt{3}}{2}, \frac{3}{2}\right). \end{aligned} \tag{2.1}$$

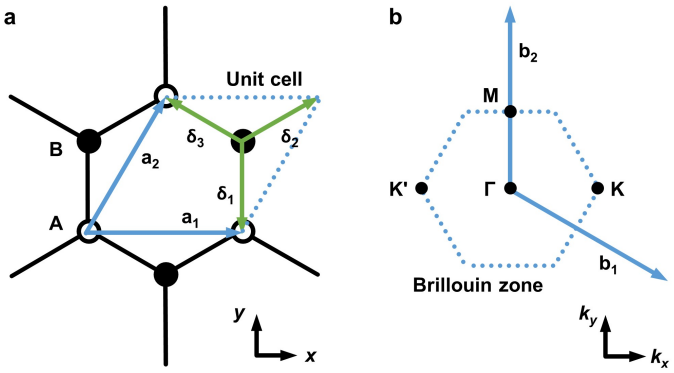

Figure 2.1: Schematic of pristine graphene. **(a)** Graphene atomic structure. The primitive lattice vectors $\mathbf{a}_1$ and $\mathbf{a}_2$ (length $\sqrt{3}\alpha = 2.46$ Å) are shown in blue. The nearest-neighbour vectors $\boldsymbol{\delta}_1$, $\boldsymbol{\delta}_2$, and $\boldsymbol{\delta}_3$ (length $\alpha = 1.42$ Å) are shown in green. Each unit cell (dotted lines) contains one A atom (hollow circles) and one B atom (solid circles). **(b)** The reciprocal lattice vectors $\mathbf{b}_1$ and $\mathbf{b}_2$ (length $4\pi/3\alpha$) are shown in blue. The BZ is indicated by the dotted lines. High-symmetry points K, K′, Γ, and M are labelled.

Note here that α is the nearest-neighbour distance (1.42 Å) and not the lattice constant (2.46 Å). The nearest-neighbour vectors are

$$\begin{aligned} \boldsymbol{\delta}_1 &= \alpha(0, -1) \\ \boldsymbol{\delta}_{2,3} &= \alpha\left(\pm\frac{\sqrt{3}}{2}, \frac{1}{2}\right). \end{aligned} \tag{2.2}$$

For reasons which will become apparent later, it is also helpful to compute

$$\boldsymbol{\delta}_{2,3} - \boldsymbol{\delta}_1 = \alpha\left(\pm\frac{\sqrt{3}}{2}, \frac{3}{2}\right). \tag{2.3}$$

The reciprocal lattice vectors are

$$\begin{aligned} \boldsymbol{b}_1 &= \frac{4\pi}{\alpha}\left(\frac{1}{2\sqrt{3}}, -\frac{1}{6}\right) \\ \boldsymbol{b}_2 &= \frac{4\pi}{\alpha}\left(0, \frac{1}{3}\right). \end{aligned} \tag{2.4}$$

We can write the Hamiltonian H by allowing electrons to hop to nearest-neighbour sites:

$$H = -t \sum_{<ij>} \left[a^\dagger(\boldsymbol{R_i}) b(\boldsymbol{R_j}) + b^\dagger(\boldsymbol{R_j}) a(\boldsymbol{R_i}) \right]. \tag{2.5}$$

Here t is the hopping parameter between adjacent sites (in real graphene, this is approximately 3 eV [18]); $\sum_{<ij>}$ indicates summation over all nearest-neighbours; $a^\dagger(\boldsymbol{R_i})$ and $a(\boldsymbol{R_i})$ ($b^\dagger(\boldsymbol{R_i})$ and $b(\boldsymbol{R_i})$) are fermionic operators that create and annihilate an electron on a(n) A (B) site at position $\boldsymbol{R_i}$. Note that for now we've neglected any on-site terms (which would be in the form of $a^\dagger a$ and $b^\dagger b$); we will discuss these later in this chapter.

We can rewrite the sum over nearest-neighbour sites using the nearest-neighbour vectors (Equation 2.2):

$$H = -t \sum_i \sum_{\boldsymbol{\delta}} \left[a^\dagger(\boldsymbol{R_i}) b(\boldsymbol{R_i} + \boldsymbol{\delta}) + b^\dagger(\boldsymbol{R_i} + \boldsymbol{\delta}) a(\boldsymbol{R_i}) \right]. \tag{2.6}$$

The Fourier transforms of $a^\dagger$ and a are

$$\begin{aligned} a^\dagger(\boldsymbol{R_i}) &= \frac{1}{\sqrt{N}} \sum_{\boldsymbol{k}} e^{-i\boldsymbol{k}\cdot\boldsymbol{R_i}} a^\dagger_{\boldsymbol{k}} \\ a(\boldsymbol{R_i}) &= \frac{1}{\sqrt{N}} \sum_{\boldsymbol{k}} e^{i\boldsymbol{k}\cdot\boldsymbol{R_i}} a_{\boldsymbol{k}} \end{aligned} \tag{2.7}$$

where N is the total number of lattice points (that is, the total number of carbon atoms is $2N$). Thus the first term of Equation 2.6 is

$$\begin{aligned} a^\dagger(\boldsymbol{R_i})b(\boldsymbol{R_i}) &= \frac{1}{\sqrt{N}}\left(\sum_{\boldsymbol{k}} e^{-i\boldsymbol{k}\cdot\boldsymbol{R_i}} a^\dagger_{\boldsymbol{k}}\right)\left(\sum_{\boldsymbol{k'}} e^{i\boldsymbol{k'}\cdot\boldsymbol{R_i}+\boldsymbol{\delta}} b_{\boldsymbol{k'}}\right) \\ &= \frac{1}{\sqrt{N}}\sum_{\boldsymbol{k},\boldsymbol{k'}} e^{-i(\boldsymbol{k}-\boldsymbol{k'})\cdot\boldsymbol{R_i}} e^{i\boldsymbol{k'}\cdot\boldsymbol{\delta}} a^\dagger_{\boldsymbol{k}} b_{\boldsymbol{k'}} \end{aligned} \tag{2.8}$$

and the second term gives its Hermitian conjugate (H.c.). Now the Hamiltonian is

$$\begin{aligned} H &= -\frac{t}{N}\sum_i \sum_{\boldsymbol{\delta},\boldsymbol{k},\boldsymbol{k'}} \left[e^{-i(\boldsymbol{k}-\boldsymbol{k'})\cdot\boldsymbol{R_i}} e^{i\boldsymbol{k'}\cdot\boldsymbol{\delta}} a^\dagger_{\boldsymbol{k}} b_{\boldsymbol{k'}} + \text{H.c.}\right] \\ &= -t\sum_{\boldsymbol{\delta},\boldsymbol{k}} \left[e^{i\boldsymbol{k}\cdot\boldsymbol{\delta}} a^\dagger_{\boldsymbol{k}} b_{\boldsymbol{k}} + e^{-i\boldsymbol{k}\cdot\boldsymbol{\delta}} b^\dagger_{\boldsymbol{k}} a_{\boldsymbol{k}}\right], \end{aligned} \tag{2.9}$$

since

$$\frac{1}{N}\sum_i e^{-i(\boldsymbol{k}-\boldsymbol{k'})\cdot\boldsymbol{R_i}} = \delta_{\boldsymbol{k},\boldsymbol{k'}}. \tag{2.10}$$

Now, if we define

$$\Psi^\dagger = \begin{pmatrix} a^\dagger_{\boldsymbol{k}} & b^\dagger_{\boldsymbol{k}} \end{pmatrix}, \ \Psi = \begin{pmatrix} a_{\boldsymbol{k}} \\ b_{\boldsymbol{k}} \end{pmatrix}, \text{ and } \mathcal{H}(\boldsymbol{k}) = -t\begin{pmatrix} 0 & \Delta_{\boldsymbol{k}} \\ \Delta^*_{\boldsymbol{k}} & 0 \end{pmatrix} \tag{2.11}$$

where $\Delta_{\boldsymbol{k}} = \sum_{\boldsymbol{\delta}} e^{i\boldsymbol{k}\cdot\boldsymbol{\delta}}$, then we can rewrite Equation 2.9 as

$$H = \sum_{\boldsymbol{k}} \Psi^\dagger \mathcal{H}(\boldsymbol{k}) \Psi. \tag{2.12}$$

The eigenenergies of this Hamiltonian are given by diagonalizing $\mathcal{H}(\boldsymbol{k})$:

$$E^2 - t^2 \Delta_{\boldsymbol{k}} \Delta^*_{\boldsymbol{k}} = 0. \tag{2.13}$$

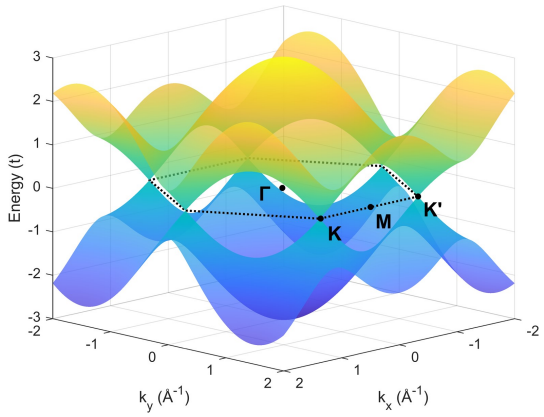

Figure 2.2: Tight binding bandstructure of pristine graphene. The two bands given by Equation 2.16 are plotted in and around the first BZ. The zone boundaries are indicated by the dotted lines; high-symmetry points are labelled. The top and bottom bands meet at the corners of the BZ.

We can expand $\Delta_{\boldsymbol{k}}$ using the nearest-neighbour vectors (Equation 2.2) and their differences (Equation 2.3):

$$\begin{aligned}
\Delta_{\boldsymbol{k}} &= \sum_{\boldsymbol{\delta}} e^{i\boldsymbol{k}\cdot\boldsymbol{\delta}} \\
&= e^{i\boldsymbol{k}\cdot\boldsymbol{\delta}_1} + e^{i\boldsymbol{k}\cdot\boldsymbol{\delta}_2} + e^{i\boldsymbol{k}\cdot\boldsymbol{\delta}_3} \\
&= e^{i\boldsymbol{k}\cdot\boldsymbol{\delta}_1}\left(e^{i\boldsymbol{k}\cdot(\boldsymbol{\delta}_2-\boldsymbol{\delta}_1)} + e^{i\boldsymbol{k}\cdot(\boldsymbol{\delta}_3-\boldsymbol{\delta}_1)}\right) \\
&= e^{ik_xa}\left(1 + e^{i\left(\frac{\sqrt{3}}{2}k_xa+\frac{3}{2}k_ya\right)} + e^{i\left(-\frac{\sqrt{3}}{2}k_xa+\frac{3}{2}k_ya\right)}\right) \\
&= e^{ik_xa}\left(1 + e^{i\frac{3}{2}k_ya}\left(e^{i\frac{\sqrt{3}}{2}k_xa} + e^{-i\frac{\sqrt{3}}{2}k_xa}\right)\right) \\
&= e^{ik_xa}\left(1 + 2e^{i\frac{3}{2}k_ya}\cos\left(\frac{\sqrt{3}}{2}k_xa\right)\right) \qquad (2.14)
\end{aligned}$$

and thus

$$\begin{aligned}
\Delta_{\boldsymbol{k}}\Delta_{\boldsymbol{k}}^{*} &= e^{ik_x a}\left(1+2e^{i\frac{3}{2}k_y a}\cos\left(\frac{\sqrt{3}}{2}k_x a\right)\right) \\
&\qquad \cdot e^{-ik_x a}\left(1+2e^{-i\frac{3}{2}k_y a}\cos\left(\frac{\sqrt{3}}{2}k_x a\right)\right) \\
&= 1+2e^{i\frac{3}{2}k_y a}\cos\left(\frac{\sqrt{3}}{2}k_x a\right)+2e^{-i\frac{3}{2}k_y a}\cos\left(\frac{\sqrt{3}}{2}k_x a\right) \\
&\qquad +4\cos^2\left(\frac{\sqrt{3}}{2}k_x a\right) \\
&= 1+4\cos\left(\frac{\sqrt{3}}{2}k_x a\right)\cos\left(\frac{3}{2}k_y a\right)+4\cos^2\left(\frac{\sqrt{3}}{2}k_x a\right). \qquad (2.15)
\end{aligned}$$

So the two energy bands associated with this model are

$$E(\boldsymbol{k}) = \pm t\sqrt{1+4\cos\left(\frac{\sqrt{3}}{2}k_x a\right)\cos\left(\frac{3}{2}k_y a\right)+4\cos^2\left(\frac{\sqrt{3}}{2}k_x a\right)}. \qquad (2.16)$$

This produces the bandstructure shown in Figure 2.2. In particular, the upper and lower bands meet at the K and K′ points on the six corners of the hexagonal Brillouin zone (BZ).

2.2 Low-energy behaviour

We can expand Equation 2.14 near $\boldsymbol{K} = (4\pi/3\sqrt{3}a, 0)$ to study the low-energy behaviour of the Hamiltonian near the Dirac points. Substituting $\boldsymbol{k} = \boldsymbol{K} + \boldsymbol{q}$, we get

$$\begin{aligned}
\Delta_{\boldsymbol{K}+\boldsymbol{q}} &= e^{iK_x a}e^{iq_x a}\left(1+2e^{i\frac{3}{2}q_y a}\cos\left(\frac{\sqrt{3}}{2}K_x a+\frac{\sqrt{3}}{2}q_x a\right)\right) \qquad (2.17) \\
&= e^{i\frac{4\pi}{3\sqrt{3}}}e^{iq_x a}\left(1+2e^{i\frac{3}{2}q_y a}\cos\left(\frac{2\pi}{3}+\frac{\sqrt{3}}{2}q_x a\right)\right) \qquad (2.18)
\end{aligned}$$

Expanding in small $\boldsymbol{q}$ to first order,

$$\Delta_{\boldsymbol{K}+\boldsymbol{q}} = e^{i\frac{4\pi}{3\sqrt{3}}}\frac{3}{2}a(-q_x + iq_y). \tag{2.19}$$

So now

$$\mathcal{H}(\boldsymbol{K}+\boldsymbol{q}) = -\frac{3}{2}at\begin{pmatrix} 0 & e^{i\frac{4\pi}{3\sqrt{3}}}(-q_x+iq_y) \\ e^{-i\frac{4\pi}{3\sqrt{3}}}(-q_x-iq_y) & 0 \end{pmatrix}. \tag{2.20}$$

Neglecting the overall phase $\exp(\pm i4\pi/3\sqrt{3})$ and defining the Fermi velocity $v_F = 3at/2$, we get

$$\mathcal{H}(\boldsymbol{K}+\boldsymbol{q}) = v_F\begin{pmatrix} 0 & q_x - iq_y \\ q_x + iq_y & 0 \end{pmatrix}. \tag{2.21}$$

Now Equation 2.16 becomes

$$E(\boldsymbol{K}+\boldsymbol{q}) = \pm v_F\sqrt{q_x^2+q_y^2}, \tag{2.22}$$

and similarly near K′. That is, near K and K′, the dispersion is linear with slope v_F in all directions, forming the characteristic Dirac cones of graphene. This is particularly interesting as it indicates that electrons in graphene behave as massless particles: that is, their energy is linear and not quadratic in momentum, and they are described by a 2D analog of the Dirac equation rather than the Schrödinger equation [18].

2.3 On-site terms

In the Dirac description of graphene, the analog of spin is a "pseudospin" related to the A and B sublattices of graphene rather than real spins. In this section, we briefly discuss the addition of on-site terms on the A and B sublattices, and the subsequent pseudospin "polarization" via sublattice symmetry breaking.

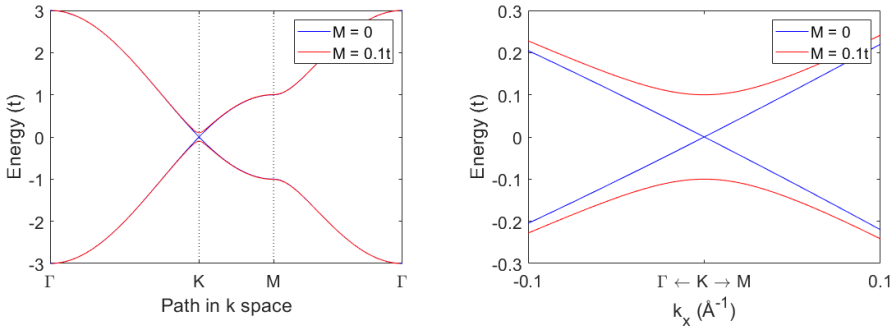

(a) **(b)**

Figure 2.3: Graphene bandstructure with a sublattice term. (a) Graphene bands are calculated along a path ΓKMΓ for $M = 0$ (blue) and $M = 0.1t$ (red). The two mostly overlap except a small gap opening at the Dirac point. **(b)** A close-up of the gap opening at the Dirac point. The full gap size is $2\Delta_{ab} = 2M$.

The simplest on-site term is a constant energy $-M$ for every site on both A and B sublattices. We can modify Equation 2.5 to:

$$H = -M \sum_{i,j} \left[a^\dagger(\boldsymbol{R_i}) a(\boldsymbol{R_i}) + b^\dagger(\boldsymbol{R_j}) b(\boldsymbol{R_j}) \right] - t \sum_{<ij>} \left[a^\dagger(\boldsymbol{R_i}) b(\boldsymbol{R_j}) + b^\dagger(\boldsymbol{R_j}) a(\boldsymbol{R_i}) \right]. \tag{2.23}$$

Following the previous derivation, Equation 2.9 becomes

$$H = -M \sum_{\boldsymbol{k}} \left[a^\dagger_{\boldsymbol{k}} a_{\boldsymbol{k}} + b^\dagger_{\boldsymbol{k}} b_{\boldsymbol{k}} \right] - t \sum_{\boldsymbol{\delta},\boldsymbol{k}} \left[e^{i\boldsymbol{k}\cdot\boldsymbol{\delta}} a^\dagger_{\boldsymbol{k}} b_{\boldsymbol{k}} + e^{-i\boldsymbol{k}\cdot\boldsymbol{\delta}} b^\dagger_{\boldsymbol{k}} a_{\boldsymbol{k}} \right]. \tag{2.24}$$

We can still write this in the form of Equation 2.12, but now

$$\mathcal{H}(\boldsymbol{k}) = - \begin{pmatrix} M & t\Delta_{\boldsymbol{k}} \\ t\Delta^*_{\boldsymbol{k}} & M \end{pmatrix}. \tag{2.25}$$

This results in an overall offset of Equation 2.16 by M, but is otherwise not particularly interesting.

However, while A and B sublattices are equivalent on pristine graphene, it is also possible to break this symmetry and introduce a different on-site term on each sublattice. If we define the on-site energy to be $-M$ on A sites and $+M$ on B sites, Equation 2.12 now becomes

$$\mathcal{H}(\boldsymbol{k}) = -\begin{pmatrix} M & t\Delta_{\boldsymbol{k}} \\ t\Delta_{\boldsymbol{k}}^* & -M \end{pmatrix} \tag{2.26}$$

and Equation 2.16 becomes

$$E(\boldsymbol{k}) = \pm t\sqrt{1 + 4\cos\left(\frac{\sqrt{3}}{2}k_x a\right)\cos\left(\frac{3}{2}k_y a\right) + 4\cos^2\left(\frac{\sqrt{3}}{2}k_x a\right) + \left(\frac{M}{t}\right)^2}. \tag{2.27}$$

This opens up a gap of size $2\Delta_{ab} = 2M$ at the Dirac points (Figure 2.3), and the graphene undergoes a metal-to-insulator transition. Indeed, sublattice symmetry-driven bandgap opening has been predicted for graphene on a hexagonal boron nitride (hBN) substrate [38, 39] and realized experimentally on a silicon carbide (SiC) substrate [41], and even in artificial graphene made of cold atoms in a honeycomb optical lattice [42].

2.4 Kekulé graphene

In Chapter 5, we describe a method to induce Kekulé bond order in graphene, in which the carbon-carbon bonds are periodically distorted (for more details, see Section 5.1). We can model Kekulé graphene using two hopping parameters $t_1 = t - \delta t$ and $t_2 = t + \delta t$ on a $(\sqrt{3} \times \sqrt{3})$ R30° supercell with a 6-atom basis (Figure 2.4). The new primitive lattice vectors are

$$\boldsymbol{a}_{1,2} = 3\alpha\left(\frac{\sqrt{3}}{2}, \pm\frac{3}{2}\right) \tag{2.28}$$

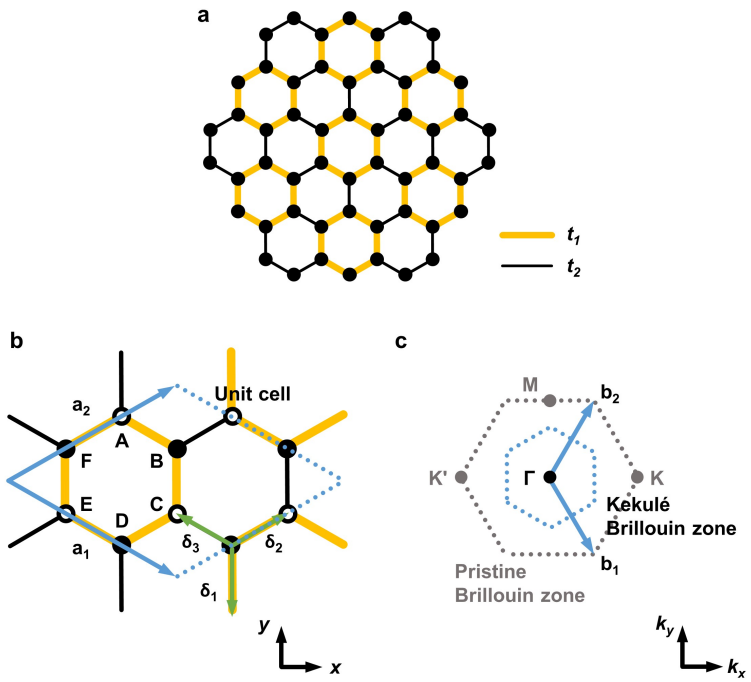

Figure 2.4: Schematic of Kekulé graphene. **(a)** A flake of graphene exhibiting Kekulé bond order. Two-thirds of the bonds have hopping energy t_1 (yellow lines) and the remaining one-third t_2 (black lines). **(b)** The $\sqrt{3} \times \sqrt{3}R30°$ Kekulé supercell. The primitive lattice vectors (blue arrows) are now 4.26 Å and rotated 30°. The nearest-neighbour vectors (green arrows) remain the same. Each unit cell (blue dotted lines) contains six atoms (A through F). **(c)** The reciprocal lattice vectors (blue arrows) now have length $4\pi/\sqrt{3}\alpha$. The BZ (blue dotted lines) is also reduced. The K and K′ points of the original BZ (grey dotted lines) are now reflected across the new zone boundaries to Γ.

and the nearest-neighbour vectors are Equation 2.2 as before. The new reciprocal lattice vectors are

$$\boldsymbol{b}_{1,2} = \frac{2\pi}{3\alpha}\left(\frac{1}{\sqrt{3}}, \pm 1\right). \tag{2.29}$$

Now Equation 2.6 becomes

$$\begin{aligned} H = -t_1 \sum_i \Big[& a^\dagger(\boldsymbol{R}_i) d(\boldsymbol{R}_i + \boldsymbol{\delta}_1) + d^\dagger(\boldsymbol{R}_i + \boldsymbol{\delta}_1) a(\boldsymbol{R}_i) \\ & + c^\dagger(\boldsymbol{R}_i) f(\boldsymbol{R}_i + \boldsymbol{\delta}_2) + f^\dagger(\boldsymbol{R}_i + \boldsymbol{\delta}_2) c(\boldsymbol{R}_i) \\ & + e^\dagger(\boldsymbol{R}_i) b(\boldsymbol{R}_i + \boldsymbol{\delta}_3) + b^\dagger(\boldsymbol{R}_i + \boldsymbol{\delta}_3) e(\boldsymbol{R}_i) \Big] \\ - t_2 \sum_i \Big[& a^\dagger(\boldsymbol{R}_i) b(\boldsymbol{R}_i + \boldsymbol{\delta}_2) + b^\dagger(\boldsymbol{R}_i + \boldsymbol{\delta}_2) a(\boldsymbol{R}_i) \\ & + c^\dagger(\boldsymbol{R}_i) b(\boldsymbol{R}_i + \boldsymbol{\delta}_1) + b^\dagger(\boldsymbol{R}_i + \boldsymbol{\delta}_1) c(\boldsymbol{R}_i) + \ldots \\ & + a^\dagger(\boldsymbol{R}_i) f(\boldsymbol{R}_i + \boldsymbol{\delta}_3) + f^\dagger(\boldsymbol{R}_i + \boldsymbol{\delta}_3) a(\boldsymbol{R}_i) \Big] \end{aligned} \tag{2.30}$$

where $a^\dagger(\boldsymbol{R_i})$, $a(\boldsymbol{R_i})$, $b^\dagger(\boldsymbol{R_i})$, $b(\boldsymbol{R_i})$, …, $f^\dagger(\boldsymbol{R_i})$, $f(\boldsymbol{R_i})$ are the creation/annihilation operators on sites A through F. Following Section 2.1, we take the Fourier transform and get

$$\begin{aligned} H = -t_1 \sum_i & \left[e^{i\boldsymbol{k}\cdot\boldsymbol{\delta}_1} a^\dagger_{\boldsymbol{k}} d_{\boldsymbol{k}} + e^{i\boldsymbol{k}\cdot\boldsymbol{\delta}_2} c^\dagger_{\boldsymbol{k}} f_{\boldsymbol{k}} + e^{i\boldsymbol{k}\cdot\boldsymbol{\delta}_3} e^\dagger_{\boldsymbol{k}} b_{bmk} + \text{H.c.} \right] \\ - t_2 \sum_i & \Big[e^{i\boldsymbol{k}\cdot\boldsymbol{\delta}_2} a^\dagger_{\boldsymbol{k}} b_{\boldsymbol{k}} + e^{i\boldsymbol{k}\cdot\boldsymbol{\delta}_1} c^\dagger_{\boldsymbol{k}} b_{\boldsymbol{k}} + e^{i\boldsymbol{k}\cdot\boldsymbol{\delta}_3} c^\dagger_{\boldsymbol{k}} d_{\boldsymbol{k}} \\ & + e^{i\boldsymbol{k}\cdot\boldsymbol{\delta}_2} e^\dagger_{\boldsymbol{k}} d_{\boldsymbol{k}} + e^{i\boldsymbol{k}\cdot\boldsymbol{\delta}_1} e^\dagger_{\boldsymbol{k}} f_{\boldsymbol{k}} + e^{i\boldsymbol{k}\cdot\boldsymbol{\delta}_3} a^\dagger_{\boldsymbol{k}} f_{\boldsymbol{k}} + \text{H.c.} \Big]. \end{aligned} \tag{2.31}$$

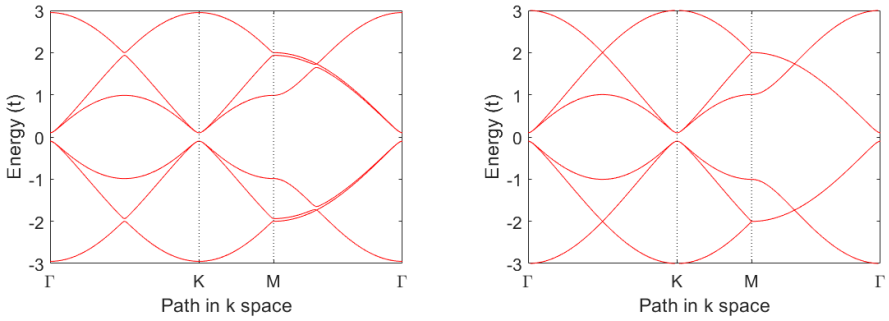

(a) **(b)**

Figure 2.5: Tight binding bandstructure of Kekulé graphene. (a) Bandstructure of Kekulé graphene calculated by diagonalizing Equation 2.32 with $\delta t = 0.05t$. The Dirac cones at K and K′ are folded to Γ and a gap of size $2\Delta_{kek} = 0.2t$ opens up at the Dirac point. **(b)** Bandstructure of Kekulé graphene calculated by diagonalizing Equation 2.33 with $\delta t = 0$ and $M = 0.1t$. As a result, a sublattice gap of size $2\Delta_{ab} = 0.2t$ opens up at the Dirac point, but there is no splitting of the bands near M as in (a). The band folding here is completely artificial, a result of choosing the Kekulé unit cell instead of the "true" graphene unit cell.

Again, we can write this in the form of Equation 2.12, with

$$\mathcal{H}(\boldsymbol{k}) = -\begin{pmatrix} 0 & t_2 e^{i\boldsymbol{k}\cdot\boldsymbol{\delta}_2} & 0 & t_1 e^{i\boldsymbol{k}\cdot\boldsymbol{\delta}_1} & 0 & t_2 e^{i\boldsymbol{k}\cdot\boldsymbol{\delta}_3} \\ t_2 e^{-i\boldsymbol{k}\cdot\boldsymbol{\delta}_2} & 0 & t_2 e^{-i\boldsymbol{k}\cdot\boldsymbol{\delta}_1} & 0 & t_1 e^{-i\boldsymbol{k}\cdot\boldsymbol{\delta}_3} & 0 \\ 0 & t_2 e^{i\boldsymbol{k}\cdot\boldsymbol{\delta}_1} & 0 & t_2 e^{i\boldsymbol{k}\cdot\boldsymbol{\delta}_3} & 0 & t_1 e^{i\boldsymbol{k}\cdot\boldsymbol{\delta}_2} \\ t_1 e^{-i\boldsymbol{k}\cdot\boldsymbol{\delta}_1} & 0 & t_2 e^{-i\boldsymbol{k}\cdot\boldsymbol{\delta}_3} & 0 & t_2 e^{-i\boldsymbol{k}\cdot\boldsymbol{\delta}_2} & 0 \\ 0 & t_1 e^{i\boldsymbol{k}\cdot\boldsymbol{\delta}_3} & 0 & t_2 e^{i\boldsymbol{k}\cdot\boldsymbol{\delta}_2} & 0 & t_2 e^{i\boldsymbol{k}\cdot\boldsymbol{\delta}_1} \\ t_2 e^{-i\boldsymbol{k}\cdot\boldsymbol{\delta}_3} & 0 & t_1 e^{-i\boldsymbol{k}\cdot\boldsymbol{\delta}_2} & 0 & t_2 e^{-i\boldsymbol{k}\cdot\boldsymbol{\delta}_1} & 0 \end{pmatrix}. \tag{2.32}$$

This is of course difficult to diagonalize as an analytic function of $\boldsymbol{k}$, but for any one particular $\boldsymbol{k}$ we can diagonalize numerically to obtain the bandstructure in Figure 2.5(a). Note that an additional Dirac cone appears at Γ due to band folding across the new BZ boundaries (Figure 2.4(b)). Additionally, a gap of $2\Delta_{kek} = 4\delta t$ opens at the Dirac points, once again

leading to a metal-to-insulator transition.

Here it is also important to note that *two* insulating phases with the same bandstructure exist: $\delta t > 0$ and $\delta t < 0$, separated by the metallic phase $\delta t = 0$. The $\delta t > 0$ case in particular has been predicted to host topological properties, while the $\delta t < 0$ case is topologically trivial [75] in a 2D analog of polyacetylene [76].

It is of course also possible to add on-site terms to the Kekulé Hamiltonian:

$$\mathcal{H}(\boldsymbol{k}) = -\begin{pmatrix} M & t_2 e^{i\boldsymbol{k}\cdot\boldsymbol{\delta}_2} & 0 & t_1 e^{i\boldsymbol{k}\cdot\boldsymbol{\delta}_1} & 0 & t_2 e^{i\boldsymbol{k}\cdot\boldsymbol{\delta}_3} \\ t_2 e^{-i\boldsymbol{k}\cdot\boldsymbol{\delta}_2} & -M & t_2 e^{-i\boldsymbol{k}\cdot\boldsymbol{\delta}_1} & 0 & t_1 e^{-i\boldsymbol{k}\cdot\boldsymbol{\delta}_3} & 0 \\ 0 & t_2 e^{i\boldsymbol{k}\cdot\boldsymbol{\delta}_1} & M & t_2 e^{i\boldsymbol{k}\cdot\boldsymbol{\delta}_3} & 0 & t_1 e^{i\boldsymbol{k}\cdot\boldsymbol{\delta}_2} \\ t_1 e^{-i\boldsymbol{k}\cdot\boldsymbol{\delta}_1} & 0 & t_2 e^{-i\boldsymbol{k}\cdot\boldsymbol{\delta}_3} & -M & t_2 e^{-i\boldsymbol{k}\cdot\boldsymbol{\delta}_2} & 0 \\ 0 & t_1 e^{i\boldsymbol{k}\cdot\boldsymbol{\delta}_3} & 0 & t_2 e^{i\boldsymbol{k}\cdot\boldsymbol{\delta}_2} & M & t_2 e^{i\boldsymbol{k}\cdot\boldsymbol{\delta}_1} \\ t_2 e^{-i\boldsymbol{k}\cdot\boldsymbol{\delta}_3} & 0 & t_1 e^{-i\boldsymbol{k}\cdot\boldsymbol{\delta}_2} & 0 & t_2 e^{-i\boldsymbol{k}\cdot\boldsymbol{\delta}_1} & -M \end{pmatrix}. \tag{2.33}$$

Here both δt and M produce a gap opening at the Dirac point, and they add in quadrature, $\Delta_{tot}^2 = \Delta_{ab}^2 + \Delta_{kek}^2$. However, only δt leads to the reduced BZ and hence the additional Dirac cone at Γ. Note that in Figure 2.5(b) we see the additional cone despite setting $\delta t = 0$: this is a consequence of the artificial definition of the unit cell. For $\delta t = 0$, the "true" unit cell is the graphene unit cell, but this calculation was performed using the Kekulé unit cell instead. In practice, no folded bands would be observed, since we can define the unit cell to be any arbitrary superstructure we like.

Near the Dirac points, we can once again write the low-energy Hamiltonian Equation 2.21, using a basis that allows the coupling of the K and K$'$ valleys:

$$\Psi = \begin{pmatrix} a_{\boldsymbol{K}+\boldsymbol{q}} \\ b_{\boldsymbol{K}+\boldsymbol{q}} \\ a_{\boldsymbol{K}'+\boldsymbol{q}} \\ b_{\boldsymbol{K}'+\boldsymbol{q}} \end{pmatrix}. \tag{2.34}$$

Finally, we have

$$\mathcal{H}(\boldsymbol{q}) = -\begin{pmatrix} M & v_F(q_x - iq_y) & 2\delta_t & 0 \\ v_F(q_x + iq_y) & -M & 0 & 2\delta_t \\ 2\delta_t^* & 0 & M & v_F(q_x - iq_y) \\ 0 & 2\delta_t^* & v_F(q_x + iq_y) & -M \end{pmatrix}, \tag{2.35}$$

where we have used δt^* to force the matrix to remain Hermitian. This allows for the coupling of the A and B sublattices via M, and the coupling of the K and K$'$ valleys via δt.

While this simple tight-binding model is capable of predicting many key features of the graphene bandstructure, we note that it does not consider many factors which can affect the bandstructure of a real material. By using a single electron, we inherently neglect all many-body effects (e.g. spin/Coulomb interactions, electron-phonon coupling, or any correlated behaviour). Charge-density modulations in particular may be important in our model, as they can naturally result from the periodic bond distortions we described in Section 2.4.

In this chapter, we derived a simple single-electron tight-binding model capable of predicting many key features of the graphene bandstructure. Starting from pristine graphene, we introduced on-site potentials which break the symmetry between the two sublattices, followed by a periodic distortion in the hopping parameters associated with the graphene bonds. While both terms lead to the opening of a gap at the Dirac point, they are not equivalent in the Hamiltonian, and the two gaps add in quadrature. In Chapter 5, this theoretical understanding will help us interpret our experimental results.

Chapter 3

Experimental methods

This chapter describes the experimental tools and techniques used in this thesis. Section 3.1 describes angle-resolved photoemission spectroscopy (ARPES). Section 3.2 describes several scanning probe microscopy (SPM) methods, including scanning tunnelling microscopy/spectroscopy (STM/STS) and atomic force microscopy (AFM). Section 3.3 describes low-energy electron diffraction (LEED). Section 3.4 describes the specific instruments used in this thesis. Section 3.5 describes the samples used and how they are prepared.

3.1 Angle-resolved photoemission spectroscopy

ARPES is an extremely powerful technique which essentially allows for direct visualization of the electronic bandstructure of a material. At its heart, ARPES is based on the photoelectric effect, first observed by Hertz in 1887 [77] and theoretically explained by Einstein in 1905 [78], in which a photon with sufficient energy strikes a material and ejects an electron. By studying the energy and momentum of these ejected electrons, we can gain deep insights about how they behave inside the material. In this section, we will present a brief overview of the technique, but extensive literature on the topic is available [79, 80, 81, 82, 83, 84, 85, 86, 87].

In the photoelectric effect, a photon of energy $h\nu$ incident upon a material ejects an electron with maximum kinetic energy $E_{kin} = h\nu - \phi$. Here h is the

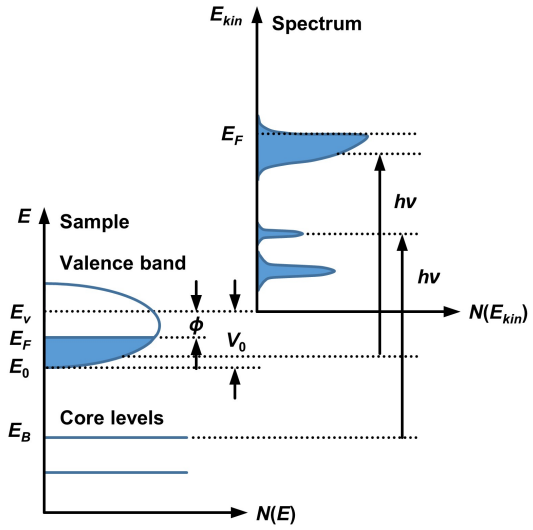

Figure 3.1: Photoemission energy schematic. In the sample, the valence band is filled up to E_F. The vacuum level near the sample is higher than E_F by ϕ, the sample work function. The binding energy E_B of an electron in the sample is usually referenced to E_F. When a photon with energy $h\nu$ ejects an electron at binding energy E_B, it loses $|E_B| + h\nu$ to freeing the electron. The remaining energy becomes the kinetic energy of the electron E_{kin}. The features of the sample spectrum become broader due to temperature and resolution effects. Adapted from [79] and [82].

Planck constant, ν is the frequency of the photon, and ϕ is the work function of the material, the potential barrier at the material surface (typically 4–5 eV in metals). If the electron was originally at some binding energy E_B below the Fermi level, it costs an additional $|E_B|$ to liberate it, $E_{kin} = h\nu - |E_B| - \phi$. Figure 3.1 shows a schematic of the energies associated with this process. If ν and ϕ are known, then by measuring the number of electrons with a particular E_{kin}, we can determine the DOS at the corresponding E_B by simple conservation of energy. This is the basis for (non-angle-resolved) photoemission spectroscopy (PES).

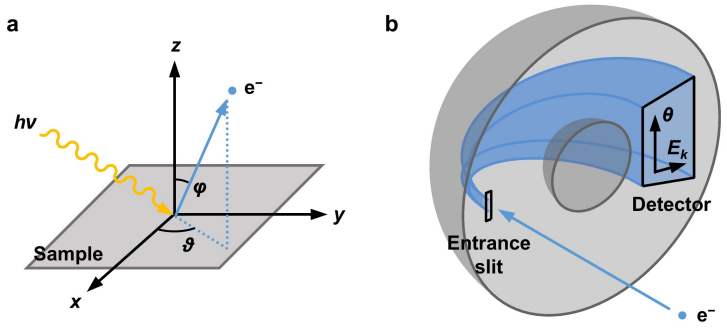

Figure 3.2: ARPES geometry. (a) A photon with energy $h\nu$ (yellow) strikes the sample and ejects an electron (blue). By measuring the trajectory of the electron, its energy and momentum can be determined. Adapted from [82]. **(b)** Simplified schematic of the hemispherical analyzer. Electrons ejected from sample pass through the entrance slit into the deflector, where two concentric hemispheres are held at a potential difference ΔV apart. During travel through the deflector, electrons are spread apart by their energy and angle. When they exit the deflector and arrive at the detector, they form a 2D distribution with energy along one axis and angle along the other.

The "angle-resolved" part of ARPES determines the momentum of the emitted electron. The magnitude of the momentum vector (in vacuum) is $K = \sqrt{2mE_{kin}}/\hbar$, split between components in and out of the sample plane, $\boldsymbol{K}_{\parallel} = K_x\hat{\boldsymbol{x}} + K_y\hat{\boldsymbol{y}}$ and $\boldsymbol{K}_{\perp} = K_z\hat{\boldsymbol{z}}$, respectively. Using the geometry in Figure 3.2(a), the components of the momentum vector are

$$K_x = \frac{1}{\hbar}\sqrt{2mE_{kin}}\,\sin\varphi\,\cos\vartheta \tag{3.1}$$

$$K_y = \frac{1}{\hbar}\sqrt{2mE_{kin}}\,\sin\varphi\,\sin\vartheta \tag{3.2}$$

$$K_z = \frac{1}{\hbar}\sqrt{2mE_{kin}}\,\cos\varphi. \tag{3.3}$$

For typical ARPES experiments with photon energies below 100 eV, the photon momentum can be neglected. It is straightforward to recover the

in-plane crystal momentum components $k_x = K_x$ and $k_y = K_y$, since they are conserved during the photoemission process due to the preserved translational symmetry across the sample-vacuum interface. However, since the potential changes abruptly at the sample surface, k_z is not conserved. Typically, it is determined by assuming a nearly-free-electron description of the final bulk state:

$$k_z = \frac{1}{\hbar}\sqrt{2m(E_{kin}\cos^2\varphi + V_0)}. \tag{3.4}$$

$V_0 = |E_0| + \phi$ is called the *inner potential*, the energy difference between the bottom of the valence band E_0 and the vacuum level (Figure 3.1). V_0 is typically determined by matching to results from theoretical calculations, or varying the photon energy and observing the periodicity in $E(k_z)$ [82]. For the work detailed in this thesis, however, this is mostly irrelevant as there is no dispersion in k_z for 2D materials such as graphene.

A more formal description of the photoemission process starts from Fermi's golden rule:

$$w_{fi} = \frac{2\pi}{\hbar}\left|\langle\Psi_f^N|H_{int}|\Psi_i^N\rangle\right|^2 \delta\left(E_f^N - E_i^N - h\nu\right). \tag{3.5}$$

Here w_{fi} is the transition probability between the N-electron ground state Ψ_i^N and final state Ψ_f^N and $\delta(E_f^N - E_i^N - h\nu)$ accounts for energy conservation. H_{int} is treated as a perturbation due to interaction with the photon:

$$H_{int} = \frac{e}{mc}\left(\boldsymbol{A}\cdot\boldsymbol{p}\right), \tag{3.6}$$

where $\boldsymbol{A}$ is the electromagnetic vector potential and $\boldsymbol{p} = i\hbar\boldsymbol{\nabla}$ is the momentum operator. This expression has been simplified by choosing the gauge where the scalar potential is 0, neglecting two-photon processes (i.e. the quadratic term, only relevant for extremely high photon intensities), and assuming that $\boldsymbol{A}$ is constant over atomic distances (valid in the UV regime) [79, 82].

Now, we can break down the photoemission process into three independent steps in what is known as the *three-step model* [88]:

1. The photon produces an optical excitation of the electron in the bulk.

2. The excited electron travels to the surface of the material.

3. The electron escapes from the material into vacuum.

The total photoemission intensity is given by the product of the probabilities involved in each step: the transition between the initial and final Bloch states, the electron travelling to the surface without scattering (i.e. mean free path), and transmission through the surface potential barrier (i.e. work function).

Here we note that while the three-step model is an extremely successful and useful approximation, a more rigorous approach is to use the *one-step model*, in which all three steps are treated as a single process. However, this becomes very complicated since the bulk, surface, and vacuum all have to be described at once, including surface and evanescent states.

To evaluate the first step, it is helpful to be able to write the N-electron final state as the antisymmetric product of the excited 1-electron state $\phi_f^{\boldsymbol{k}}$ and the remaining $(N-1)$-electron state Ψ_f^{N-1},

$$\Psi_f^N = \mathcal{A}\phi_f^{\boldsymbol{k}}\Psi_f^{N-1}, \tag{3.7}$$

where $\mathcal{A}$ is an operator that antisymmetrizes the N-electron wavefunction. This is the *sudden approximation*, in which we assume that the time it takes the electron to leave the sample is much shorter than the time scale of the system relaxation (valid for electrons with high kinetic energy).

We can factor the initial state Ψ_i^N similarly by assuming that it can be written as a single Slater determinant,

$$\Psi_i^N = \mathcal{A}\phi_i^{\boldsymbol{k}}\Psi_i^{N-1}. \tag{3.8}$$

Then the matrix element from Equation 3.5 can be written as

$$\langle \Psi_f^N | H_{int} | \Psi_i^N \rangle = \langle \phi_f^{\boldsymbol{k}} | H_{int} | \phi_i^{\boldsymbol{k}} \rangle \langle \Psi_f^{N-1} | \Psi_i^{N-1} \rangle . \tag{3.9}$$

Here $\langle \phi_f^{\boldsymbol{k}} | H_{int} | \phi_i^{\boldsymbol{k}} \rangle$ is the one-electron dipole matrix element $M_{f,i}^{\boldsymbol{k}}$, a function of electron momentum, photon energy, and photon polarization (often referred

to as "matrix element effects").

Besides the electronic dispersion $\epsilon_{\boldsymbol{k}}$, ARPES also captures many-body effects. For this it is helpful to go to the Green's function formalism [82, 89, 90, 91, 92, 93, 94], which describes the propagation of an electron in a many-body system:

$$G(\boldsymbol{k},\omega) = \frac{1}{\omega - \epsilon_{\boldsymbol{k}} - \Sigma(\boldsymbol{k},\omega)}, \tag{3.10}$$

which is a function of the self-energy

$$\Sigma(\boldsymbol{k},\omega) = \Sigma'(\boldsymbol{k},\omega) + i\Sigma''(\boldsymbol{k},\omega). \tag{3.11}$$

The real part $\Sigma'(\boldsymbol{k},\omega)$ describes band renormalization, while the imaginary part $\Sigma''(\boldsymbol{k},\omega)$ describes lifetime or linewidth. This is related to the one-particle spectral function

$$A(\boldsymbol{k},\omega) = -\frac{1}{\pi}\frac{\Sigma''(\boldsymbol{k},\omega)}{\left[\omega - \epsilon_{\boldsymbol{k}} - \Sigma'(\boldsymbol{k},\omega)\right]^2 + \left[\Sigma''(\boldsymbol{k},\omega)\right]^2} \tag{3.12}$$

which finally gives the intensity of the measured spectra in ARPES:

$$I(\boldsymbol{k},\omega) = I_0(\boldsymbol{k},\nu,\boldsymbol{A})f(\omega)A(\boldsymbol{k},\omega) \tag{3.13}$$

where $I_0(\boldsymbol{k},\nu,\boldsymbol{A})$ is proportional to $|M^{\boldsymbol{k}}_{f,i}|^2$ and $f(\omega) = (\exp(\omega/k_BT)+1)^{-1}$ is the Fermi function, since electrons can only be emitted from occupied states.

In a typical ARPES experiment, a sample surface is first prepared in ultra-high vacuum (UHV) by sputtering/annealing or cleaving. Alternatively, the sample can be grown *in situ*. It is crucial that the sample surface remains clean throughout the experiment, as the electron mean free path in most materials is only a few nm for kinetic energies between 10 and 100 eV [79], i.e. ARPES is only able to probe the topmost atomic layers. This also implies that the bulk electronic structure may not always be well-represented; however, it also makes ARPES an ideal technique for studying 2D materials such as graphene.

Next, a monochromatized beam of photons is focused on the sample. This can come from a variety of sources: gas discharge lamps, lasers, or synchrotron light. All of the ARPES data presented in this thesis are collected using a helium discharge lamp with the He I line (21.2 eV).

The emitted electrons are then collected by the analyzer. First, an electrostatic lens focuses the electrons onto the entrance slit of a hemispherical deflector. Here, electrons pass through two concentric hemispheres held at a potential difference. As they travel through the deflector, electrons are spaced apart by their kinetic energy in one direction and their angle in the other, and eventually land on a 2D detector consisting of a phosphor plate read out by a camera (Figure 3.2), producing an intensity map as a function of E_{kin} and ϑ. This is the type of analyzer used for all of the work in this thesis. Older analyzers without such a 2D detector usually use an exit slit to select only one energy at a time. Angle-resolved time-of-flight (ARTOF) analyzers also exist: rather than determining the electron kinetic energy by their location on the detector, they instead measure the speed of an electron using its arrival time. With this information, the analyzer can measure kinetic energy and a wide range of angles all at once, providing an extremely fast way to map the electronic bandstructure of a material, although at a cost in intensity and resolution [95].

To interpret this data, we need to infer E_B from E_{kin} (Figure 3.3). E_{kin} measured by the analyzer is different from E_{kin} shown in Figure 3.1, as the work function of the analyzer also comes into play. Since both the sample and analyzer are connected to the same ground, their Fermi levels must match. If their work functions ϕ_s and ϕ_a are different (typically ϕ_a is larger), then the vacuum level near the sample and the analyzer will be different. By moving through this difference in energy, the electron loses an additional $\phi_a - \phi_s$, so that E_{kin} measured at the analyzer is

$$E_{kin} = h\nu - |E_B| - \phi_s - (\phi_a - \phi_s) = h\nu - |E_B| - \phi_a. \tag{3.14}$$

Since ϕ_a is a constant independent of the sample measured, we can obtain E_B by comparing with a known sample. Typically polycrystalline gold

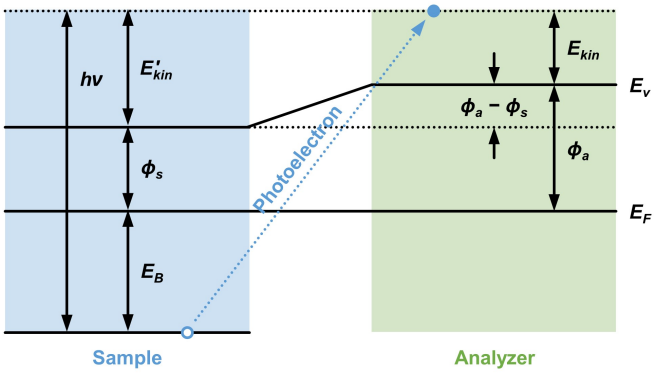

Figure 3.3: Sample and analyzer energy schematic. The Fermi levels of the sample and analyzer are forced to be equivalent by electrically grounding them together. For calculating E_B from E_{kin} as measured at the analyzer, it is the analyzer work function ϕ_a that is relevant, not the sample work function ϕ_s. Adapted from [79].

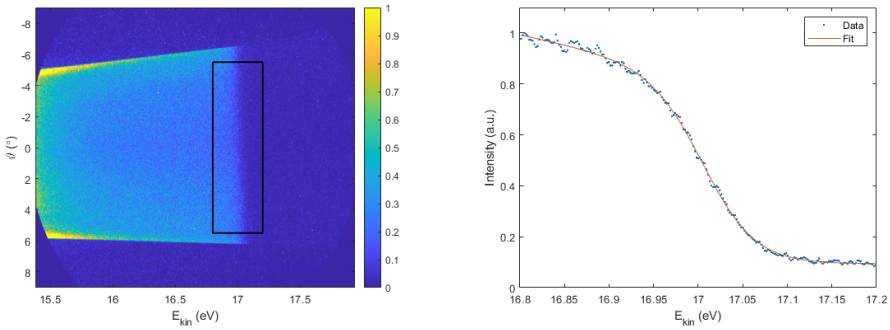

(a) **(b)**

Figure 3.4: Gold reference measurement. (a) ARPES data taken on a polycrystalline gold sample at 5 K. No bands are visible, and the intensity is relatively flat near the Fermi level. **(b)** An integrated spectrum calculated by summing over all angles in the region indicated by the box in (a). The Fermi edge is broadened by temperature, resolution, and detector effects. By fitting the position of the Fermi edge, the relationship between E_{kin} and E_B can be determined.

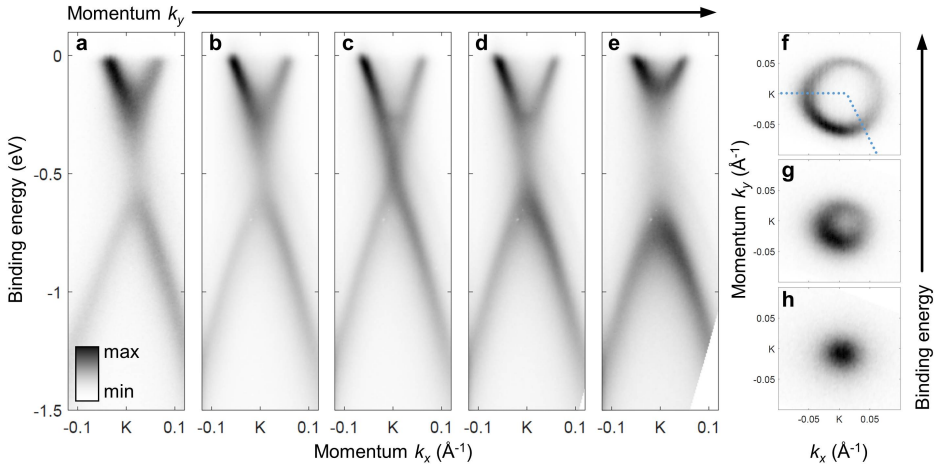

Figure 3.5: ARPES data example. In a typical ARPES experiment, spectra are collected for a range of angles, which is then converted to momentum-space coordinates via Equation 3.3. Here, a volume of intensity data (k_x, k_y, E) is collected near one of the Dirac points of graphene. Panels **(a)** through **(e)** are energy vs. momentum cuts taken through the cone for a range of k_y between $K_y - 0.02$ Å^{-1} and $K_y + 0.02$ Å^{-1}. Note that no intensity is measured above the Fermi level. Panels **(f)**, **(g)**, and **(h)** are isoenergy cuts taken at $E_B = -0.01, -0.2$, and -0.4 eV respectively. The BZ boundary is overlaid in blue dotted lines.

is used, since it has a relatively flat DOS near E_F and does not become superconducting at low temperatures. By comparing to the gold spectra, we can precisely determine E_B for the sample spectra (Figure 3.4).

Example spectra taken on a graphene sample are shown in Figure 3.5. Intensity data was collected for a volume (ϑ, φ, E) near one of the Dirac points, which was then converted to (k_x, k_y, E) using Equation 3.3. E_{kin} was converted to E_B via Equation 3.14 and spectra taken on polycrystalline gold. Cuts can be taken in either momentum or energy to visualize the dispersion or iso-energy contours. Note that the intensity is anisotropic about the $\boldsymbol{K}$ point due to ARPES matrix element effects.

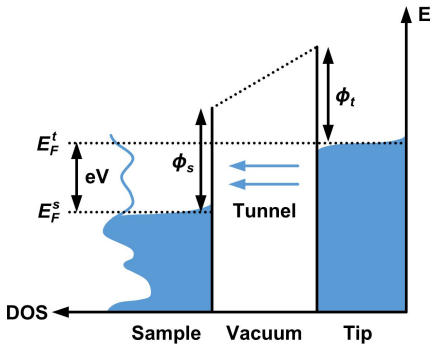

Figure 3.6: Energy schematic of the tunnelling process. By applying a bias V, E_F^t is shifted to eV above E_F^s. In the range of energies where the tip states are occupied but the sample states are not, electrons can tunnel through the potential barrier formed by the work functions of the tip and sample (indicated by the dotted line; in practice, the potential is not necessarily linear in distance). The DOS of the tip is assumed to be flat. Adapted from [99].

3.2 Scanning probe microscopy

SPM covers the family of techniques that rely on physically scanning an atomically sharp probe over a sample in order to map out its local properties with sub-angstrom resolution. SPM was born in 1982, when Binnig and Rohrer of IBM first invented the scanning tunnelling microscope (STM) [96, 97], which relies on the quantum phenomenon of tunnelling to image surfaces of metallic and semiconducting samples using a metallic tip. Additionally, an STM also provides information about the local DOS (LDOS) of the sample via STS. For this work, Binnig and Rohrer were awarded the 1986 Nobel Prize in Physics. Also in 1986, Binnig, Quate, and Gerber invented the atomic force microscope (AFM) [98], which relies on the forces between tip and sample to image even insulating surfaces. This section provides a brief overview of STM/STS and AFM.

3.2.1 Scanning tunnelling microscopy

In STM, a metallic, atomically sharp tip is used to probe a metallic or semiconducting sample. Normally, the work functions of the tip and sample prevent the electrons inside the tip and sample from escaping into vacuum, but if the tip is positioned very close (a few angstroms) to the sample surface, electrons can tunnel through this vacuum barrier. When a voltage difference ("bias") is applied between the tip and sample, these electrons produce a small but measurable *tunnelling current* (Figure 3.6). This current, to a first approximation, is proportional to the integrated DOS of the sample. By scanning the tip over the sample surface and measuring the tunnelling current, we can gain information about both the surface height and local electronic properties of the sample.

For a formal description of the tunnelling process [100, 101, 102, 103, 104, 105, 106], we once again start from Fermi's golden rule:

$$w_{\mu\nu} = \frac{2\pi}{\hbar}|M_{\mu\nu}|^2\delta\left(E_\mu^S - E_\nu^T\right). \tag{3.15}$$

Analogous to the ARPES case, $w_{\mu\nu}$ is the transition probability between the sample and tip states ψ_μ^S and ψ_ν^T. $M_{\mu\nu}$ is the tunnelling matrix element obtained by treating the tip-sample barrier as a perturbation [101]. For this discussion, we consider only elastic tunnelling, ensured by $\delta(E_\mu^S - E_\nu^T)$.

The tunnelling current I is proportional to $ew_{\mu\nu}$ summed over all states μ and ν where tunnelling can occur, that is, from an occupied state to an unoccupied state as described by the Fermi function

$$f(E - E_F) = \frac{1}{e^{(E-E_F)/k_BT} + 1}. \tag{3.16}$$

With a bias V between the tip and sample, the tunnelling current from the occupied states of the sample $f(E_\mu^s - E_F^s)$ to the unoccupied states of the tip $1 - f(E_\nu^t - E_F^t)$ tip is

$$I_{s\to t} = \frac{4\pi e}{\hbar}\sum_{\mu\nu} f\left(E_\mu^s - E_F^s\right)\left[1 - f\left(E_\nu^t - E_F^t\right)\right]|M_{\mu\nu}|^2\delta\left(E_\nu^t - E_\mu^s - eV\right). \tag{3.17}$$

The extra factor of 2 accounts for the two spin states of the electron. Regardless of the sign of V, tunnelling also occurs in the reverse direction:

$$I_{t\to s} = \frac{4\pi e}{\hbar}\sum_{\mu\nu} f\left(E_\mu^t - E_F^t\right)\left[1 - f\left(E_\nu^s - E_F^s\right)\right]|M_{\mu\nu}|^2\delta\left(E_\nu^t - E_\mu^s - eV\right). \tag{3.18}$$

The measured tunnelling current is then given by the difference between the two directions:

$$I = \frac{4\pi e}{\hbar}\sum_{\mu\nu}\left[f\left(E_\mu^s - E_F^s\right) - f\left(E_\mu^t - E_F^t\right)\right]|M_{\mu\nu}|^2\delta\left(E_\nu^t - E_\mu^s - eV\right). \tag{3.19}$$

The summation can be re-written as an integral $\int n(\epsilon)\, d\epsilon$:

$$\begin{aligned} I = \frac{4\pi e}{\hbar}\int d\epsilon\left[f\left(E_F^t - eV + \epsilon\right) - f\left(E_F^s - eV + \epsilon\right)\right] \\ \cdot\, n_t\left(E_F^t - eV + \epsilon\right) n_s\left(E_F^s + \epsilon\right)\left|M\left(E_F^s + \epsilon, E_F^t - eV + \epsilon\right)\right|^2 \end{aligned} \tag{3.20}$$

where n_s and n_t are the DOS of the sample and tip, respectively. To simplify this expression, we can approximate the Fermi distributions by a step function (i.e. k_BT is small compared to the features in the DOS, valid for most cryogenic STM measurements):

$$I = \frac{4\pi e}{\hbar}\int_0^{eV} d\epsilon\; n_t\left(E_F^t - eV + \epsilon\right) n_s\left(E_F^s + \epsilon\right)|M|^2. \tag{3.21}$$

Here we can see that the tunnelling current is dependent on both the density of states of the sample and the tip. In general, the DOS of the tip is neither known nor easy to determine, but by comparing to a known sample, the tip can be prepared such that it has a relatively flat DOS (i.e. is energy-independent) near the Fermi level:

$$I = \frac{4\pi e}{\hbar} n_t(0)\int_0^{eV} d\epsilon\; n_s\left(E_F^s + \epsilon\right)|M|^2. \tag{3.22}$$

The matrix element can also be pulled out of the integral if we assume it to be constant in energy (valid for energy ranges where the tip and sample

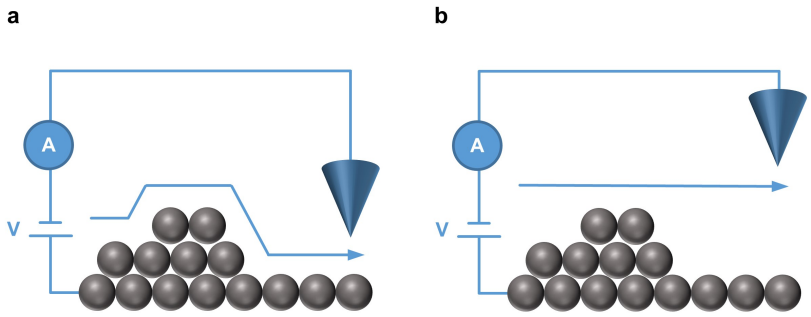

Figure 3.7: STM operation modes. **(a)** Constant current scanning mode. The tip-sample distance is adjusted so that the tunnelling current is always equal to the set current. **(b)** Constant height scanning mode. The tip height is fixed and the tunnelling current is monitored instead. This is less popular since samples are often not perfectly flat, so there is the risk of crashing the tip or losing the tunnelling current since it falls off exponentially as the tip moves away from the sample.

wavefunctions are orthogonal) [101]. If we assume that the tip has an s-like wavefunction (valid for most metals), we can model the matrix element using the Wentzel-Kramers-Brillouin (WKB) approximation for tunnelling through a rectangular barrier:

$$|M|^2 = e^{-\kappa z} \tag{3.23}$$

where z is the tip-sample separation and κ is a constant related to the work functions of the tip and sample. This exponential dependence of current on distance is one of the reasons that STM is capable of such high spatial resolution. Finally, then, we can shift the energy scale to $E_F^s = 0$ and obtain

$$I \propto e^{-\kappa z} \int_0^{eV} d\epsilon \; n_s(\epsilon). \tag{3.24}$$

To measure this tunnelling current experimentally, we also start by preparing an atomically clean sample surface in UHV. The tip is positioned precisely by the use of piezoelectric scanners, which deflect by small amounts

when a voltage is applied. A bias can be applied to either the tip or the sample; the sign of the bias determines whether the occupied or unoccupied states of the sample are being probed.

Two scanning modes are commonly used (Figure 3.7): in *constant-current mode*, a set current (typically tens to hundreds of pA) is selected by the user, and a feedback loop adjusts the tip-sample distance until the tunnelling current matches the set current. While scanning, the tip height is recorded at each position. However, it should be noted that this is not simply the surface height, but its convolution with the local integrated DOS; if the integrated DOS changes, for example, the tip will also move to compensate, and this effect may be bias dependent. At different biases, features may appear differently.

An alternative, less common scan mode is *constant-height mode*, where the tip is scanned at a fixed height and the tunnelling current is recorded instead. However, if the sample surface is not perfectly flat, this mode runs the risk of crashing the tip into the sample, or the tip moving too far away from the sample to measure a tunnelling current, since the tunnelling current falls off exponentially with tip-sample distance.

Another result of the exponential dependence on the tip-sample distance is that the outermost atom in the tip will contribute most strongly to the signal. Aside from providing high spatial resolution, this also means that the larger features of the tip are not particularly important for the experiment. However, it is usually non-trivial to prepare a stable, metallic, and atomically sharp tip.

First, a tip must be prepared in air before entering the UHV system. Typically, tips are made from platinum-iridium, silver, or tungsten wire, either by cutting with a pulling motion or electrochemical etching. Once the tip is in vacuum, several tip-conditioning techniques are available. The tip can be annealed to remove oxides, either by bombarding with electrons ("*e*-beam") or resistive heating with a filament. Metallic samples (typically gold, silver, copper, or aluminum, either single-crystal or polycrystalline) can also be used for tip treatment: by applying a high bias across the tip-sample junction, the resulting electric field and heating tends to reshape the tip, or

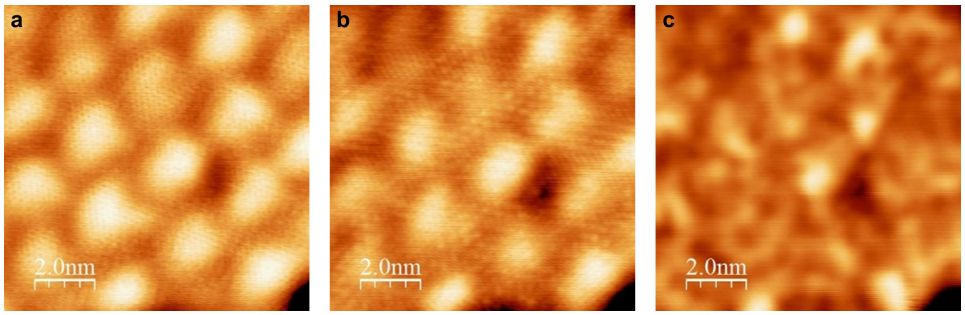

Figure 3.8: STM data example. Topography taken on a graphene sample in constant-current mode at **(a)** 0.1 V, **(b)** 0.4 V, and **(c)** 1.0 V. The set current is 10 pA for all three images. Even though the same area is scanned in all three panels, different features appear and disappear due to the change in bias. (For details, see Chapter 6.)

the tip can be gently pushed into the sample by a few nm to coat the end in metallic atoms. In cases where contact with the sample is undesirable, the bias can be pulsed sharply (a few volts over tens of ms) in order to encourage small changes in the tip.

Another crucial factor in STM experiments is vibration isolation. Since the tip and sample must stay only a few angstroms apart, this can present a great challenge. Typically, the STM head is suspended on springs inside the UHV chamber, and magnetic coupling provides eddy current damping. Additionally, the entire STM can be supported by pneumatic isolators, hung from elastic cords, or placed inside an isolation facility (for details on our setup, see Section 3.4.2). Any mechanical pumps (such as scroll/turbo pumps) must be turned off or decoupled from the system during STM operation; thus, ion getter pumps are commonly used for STM systems.

Some examples of typical STM data are shown in Figure 3.8. The three panels are taken on the same area with different biases; the vastly different topography showcases the dependence of the tunnelling current on both the physical height and the integrated DOS. No post-processing was performed on these images; however, plane-subtraction to account for sample tilt or frequency filtering to remove noise are common techniques. To visualize the periodicities present in an image, Fourier analysis is commonly used.

3.2.2 Scanning tunnelling spectroscopy

Since the tunnelling current is proportional of the integrated LDOS of the sample (Equation 3.24), we should be able to recover the local DOS by measuring $I(V)$ and taking the derivative, $n_s = dI/dV$. The measured spectra may also be modified due to other effects. In graphene, for example, no states are available near $\mathbf{\Gamma}$, so elastic tunnelling is forbidden; however, inelastic tunnelling through a phonon is possible, and as a result, the spectra becomes gapped at the Fermi level [107, 108, 109]. Since we started our discussion of STM by assuming elastic tunnelling in Equation 3.15, however, such effects are not captured.

Typically, $I(V)$ is measured by fixing the tip-sample separation and sweeping over a range of V while measuring the resulting I. A reference sample, typically single-crystal metals with a known distinctive surface state, can be used to check that the tip produces the expected behaviour (i.e. has a flat density of states near E_F). As an alternative to sweeping V, lock-in amplification can also be used to measure dI/dV directly. Here, a small sinusoidal component (typically a few mV and a few hundred Hz) is added to the bias, and a lock-in amplifier can be used to measure the resulting oscillation in the tunnelling current. dI/dV can then be quickly obtained from ratio of the oscillation amplitudes. A higher bias amplitude improves the signal to noise ratio, but at the cost of energy resolution. This technique is commonly used to obtain spatial dI/dV maps, since it is much faster than measuring $I(V)$ at each point in the scan. Such maps can even be used to obtain information on the bandstructure of the sample via quasiparticle interference (QPI) [110, 111].

3.2.3 Atomic force microscopy

As AFM is only used briefly for the work detailed in this thesis, we will only qualitatively describe its operation. In essence, AFM is very similar to STM, but instead of the tunnelling current, AFM uses a sensor attached to the tip to measure the force between the tip and the sample [98]. This means that unlike STM, even insulating samples can be probed.

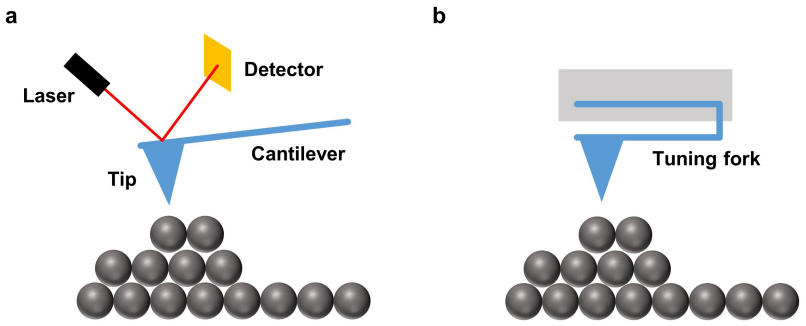

Figure 3.9: AFM sensors. (a) A cantilever sensor is deflected by atomic forces. The deflection is read out by a laser beam reflected off the end of the cantilever. **(b)** The resonance frequency of a tuning fork sensor changes as a function of the forces on the tip. No optical access is required to read out the change in frequency.

The force measured in AFM comes from a combination of sources: electrostatic (due to bias and capacitance of the tip-sample junction), Van der Waals, and chemical (such as Pauli repulsion and the dispersion force) [112]. Typically, the sensor is a silicon cantilever or a quartz tuning fork, which deflect or change in resonance frequency when force is applied (Figure 3.9). The cantilever deflection is usually read out by a laser beam reflected off the end; thus, the tuning fork sensors are more popular for cryogenic applications where optical access may be limited.

Three modes of AFM operation are commonly used. In *contact mode*, a cantilever is pushed against the sample, resulting in a strong repulsive force, and the cantilever deflection is measured. In *non-contact mode*, either an oscillating cantilever or a tuning fork can be used to measure the frequency shift due to a weak attractive force [113]. In *tapping mode*, an oscillating cantilever intermittently contacts the sample, and the oscillation amplitude is measured.

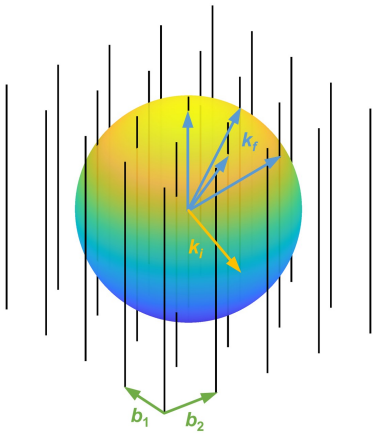

Figure 3.10: Ewald sphere construction. As only elastic scattering is considered in LEED, the momenta of the incoming ($\boldsymbol{k}_i$) and outgoing ($\boldsymbol{k}_f$) electrons are equal in magnitude, and all scattering vectors must connect two points on a sphere of radius $|\boldsymbol{k}|$. Reciprocal lattice rods (rather than points), separated by reciprocal lattice vectors $\boldsymbol{b}_1$ and $\boldsymbol{b}_2$ are shown due to the highly 2D nature of the technique.

3.3 Low-energy electron diffraction

LEED is yet another extremely surface-sensitive technique for characterizing the structure of a material. It relies fundamentally on the wavelike character of electrons: by elastically scattering electrons off the sample surface, they interfere constructively and destructively, resulting in a pattern corresponding to the periodicities present in the sample [114, 115].

Constructive interference occurs when the Laue condition is satisfied [116]:

$$\boldsymbol{k}_f - \boldsymbol{k}_i = \boldsymbol{G}_{hkl} = h\boldsymbol{b}_1 + k\boldsymbol{b}_2 + l\boldsymbol{b}_3, \tag{3.25}$$

where $\boldsymbol{k}_i$ is the momentum of the incoming electron, $\boldsymbol{k}_f$ is the momentum of the scattered electron, and $\boldsymbol{G}_{hkl}$ is an integer combination of reciprocal space lattice vectors $\boldsymbol{b}_{1,2,3}$. As we saw in Section 3.1, electrons cannot travel freely very far in most materials: for typical LEED electron energies of 20–100 eV,

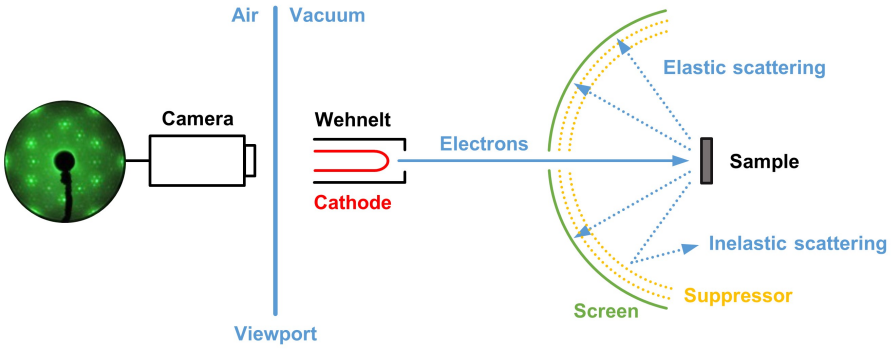

Figure 3.11: Schematic of a LEED instrument. Electrons are emitted from a cathode filament and focussed by a Wehnelt cylinder. Inelastically scattered electrons are blocked by a suppressor grid, while elastically scattered electrons are allowed to reach the fluorescent screen. A camera is used to record the screen intensity. A typical image of a LEED screen is shown; the center area of the screen is blocked by the electron gun. Adapted from [117].

this is further reduced to only a few angstroms [79], which is equivalent to only one or two atomic layers. Thus periodicity in the out-of-plane direction is ill-defined, and the Laue condition is reduced to 2D only:

$$\boldsymbol{k}_f^{\parallel} - \boldsymbol{k}_i^{\parallel} = \boldsymbol{G}_{hk} = h\boldsymbol{b}_1 + k\boldsymbol{b}_2 \tag{3.26}$$

As with Laue diffraction, this can be visualized using the Ewald sphere construction, using reciprocal lattice rods instead of points in the out-of-plane direction (Figure 3.10) [116]. $|\boldsymbol{k}_f| = |\boldsymbol{k}_i| = |\boldsymbol{k}|$ is required by elastic scattering, so all scattering vectors must lie on the surface of a sphere of radius $|\boldsymbol{k}|$. When a scattering vector connects two intersections of the sphere with the reciprocal lattice rods, constructive interference occurs, corresponding to a bright spot in the LEED pattern.

Due to its surface-sensitive nature, LEED also must be performed in UHV on an atomically clean sample. A schematic of a typical LEED instrument is shown in Figure 3.11. A monochromatic beam of electrons is produced by a cathode filament and focused by a Wehnelt cylinder onto the sample (typical

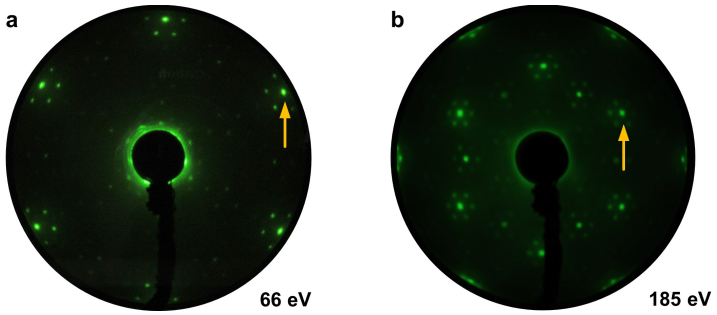

Figure 3.12: LEED data example. LEED pattern on graphene using electrons with **(a)** 66 eV and **(b)** 185 eV. The primary graphene spots are indicated by the yellow arrows.

emission is on the order of 10^{14} electrons per second). Since LEED requires elastically scattered electrons, inelastically scattered electrons with lower energy are blocked by suppressor grids, and only those with high enough energy are allowed to reach the screen. The diffraction pattern can then be directly viewed on the hemispherical fluorescent screen, and images can be taken through a viewport using a camera. Example LEED patterns taken on graphene/SiC are shown in Figure 3.12. Higher-energy electrons allow a greater area of reciprocal space to be probed, but at a cost of damaging the sample surface over time.

3.4 Description of instruments used

3.4.1 Home-built ARPES system

A home-built ARPES system was used for the work detailed in Chapter 5 (Figure 3.13). It is equipped with a SPECS Phoibos 150 Hemispherical Analyzer, a SPECS UVS300 Monochromatized Gas Discharge Lamp (capable of producing both *s*- and *p*-polarized light), and a SPECS ErLEED 1000A. A cryostat cooled by liquid helium (LHe) is able to produce sample temperatures as low as 5 K. For the settings used in these experiments, the energy and momentum resolution were better than 50 meV and 0.01 Å^{-1}, respectively.

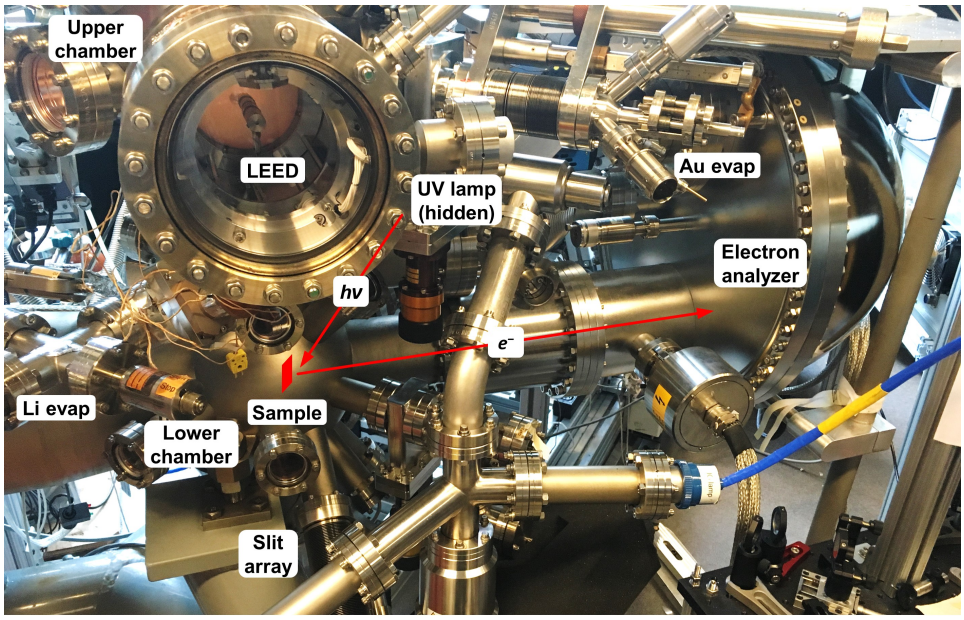

Figure 3.13: Home-built ARPES instrument. A photo of the ARPES instrument used for the work in Chapter 5. Key components are labelled; the helium UV lamp is hidden behind the chamber and cannot be seen from this angle. The paths of the photon and ejected electron are shown. Lithium and gold can be deposited *in situ* by moving the sample up and down and rotating; LEED is available as well. A slit array, used to correct for imperfections in the analyzer (see Appendix A), can be inserted in front of the analyzer entrance.

Samples are introduced to the system through a load lock (typical pressure 10^{-7} mbar) pumped by a turbomolecular (turbo) pump. They then are moved into the preparation chamber (typical pressure 10^{-9} mbar), pumped by a turbo pump and a titanium sublimation pump (TSP). Here samples can be annealed up to ∼900°C by a heater, and gadolinium or copper can be deposited by e-beam evaporation. Next, the sample can be loaded into the cryostat in the two interconnected main chambers (typical pressure 10^{-11} mbar), the upper and lower chamber. In the upper chamber, pumped by a turbo pump, samples can be cleaved or analyzed using LEED, and gold can be deposited via e-beam evaporation. In the lower chamber, pumped by a

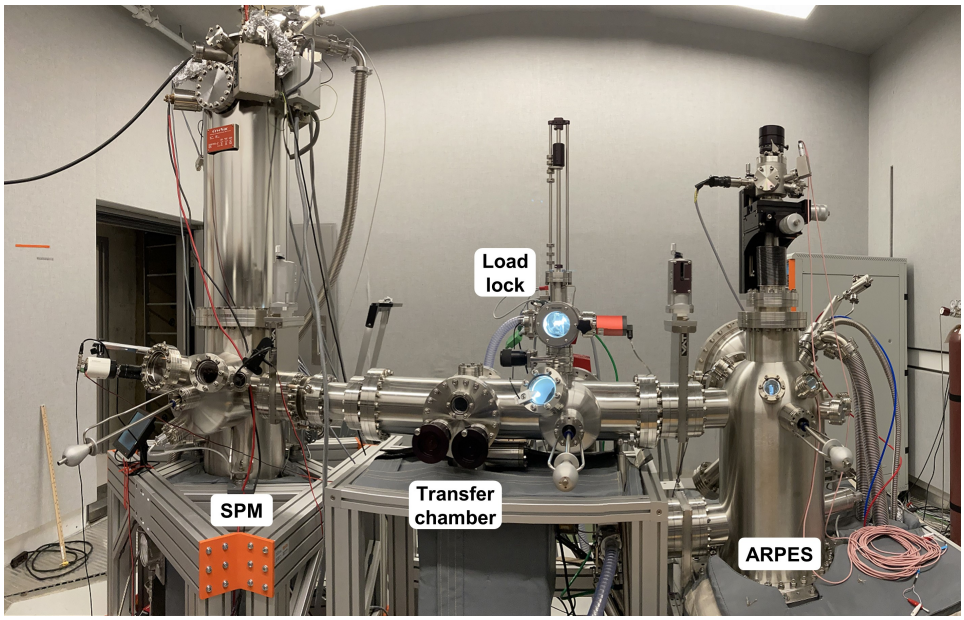

Figure 3.14: Scienta Omicron combined system. A photo of the Scienta Omicron ARPES/SPM combined system. The ARPES (right) and SPM (left) instruments are separated by a long transfer chamber.

cryopump, lithium can be deposited using a SAES alkali metal dispenser, and ARPES is performed using the UV lamp and electron analyzer. Additionally, a slit array can be inserted in front of the sample to calibrate the analyzer.

3.4.2 Scienta Omicron ARPES/SPM combined system

A commercial system manufactured by Scienta Omicron was used for the work detailed in Chapter 4 and Chapter 6 (Figure 3.14). It consists of a Scienta Omicron Tesla Joule-Thomson (JT) SPM and an ARPES instrument equipped with a Scienta Omicron R3000 Hemispherical Analyzer and a FOCUS VUV Source HIS 13 lamp. The two instruments are connected by a transfer chamber, allowing the same sample to be characterized by both techniques without leaving UHV.

For this system, samples are also introduced through a load lock (typical pressure 10^{-7} mbar, maintained by a turbo pump). Next, samples enter

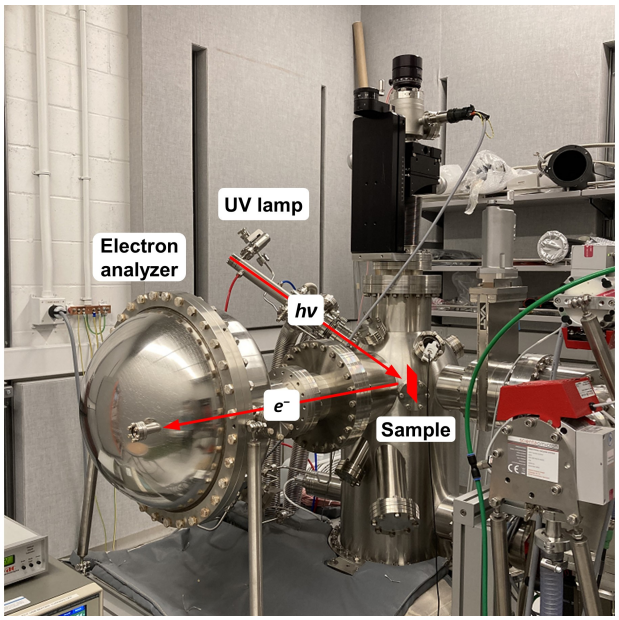

Figure 3.15: Scienta Omicron ARPES instrument. A photo of the ARPES instrument in the combined system. Key components are labelled, and the paths of the photon and ejected electron are shown. The transfer chamber to the right connects to the SPM instrument.

into the long transfer chamber (typical pressure 10^{-9} mbar, maintained by a turbo pump and an ion pump), where samples can be cleaved and a long rail carries them to either the ARPES or the SPM instrument. UHV storage for multiple samples is also available inside the transfer chamber (3 slots) and SPM chamber (6 slots).

The ARPES instrument (Figure 3.15) is equipped with a cryostat (Figure 3.16) which can be cooled to below 140 K using liquid nitrogen (LN_2). Alternatively, a built-in heater can also heat the sample to temperatures as high as 800°C, which can also be used to prepare samples for SPM. Pressures in the ARPES chamber during measurements are typically on the order of 10^{-9} to 10^{-10} mbar, maintained by a turbo pump, an ion pump, and a TSP.

The SPM instrument is equipped with a JT cryostat capable of producing temperatures below 1.2 K. Here LHe or helium gas is forced through a narrow capillary by a pump (called a "throttling process"), and cooling occurs due

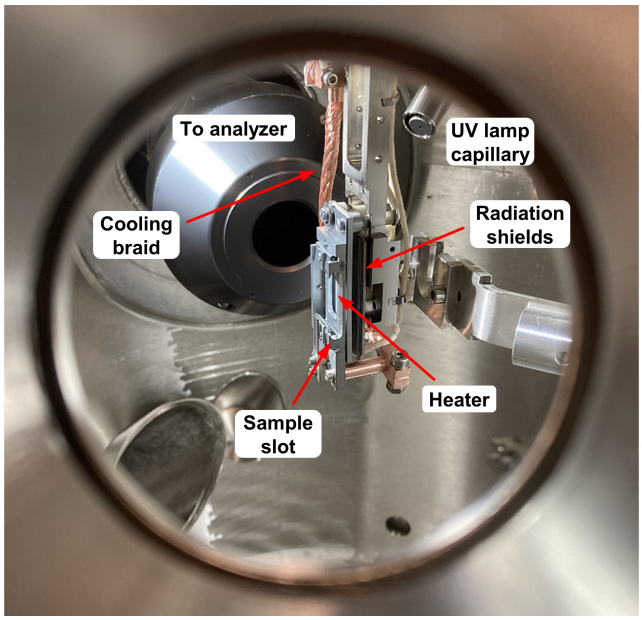

Figure 3.16: Scienta Omicron ARPES cryostat. View inside the ARPES chamber. The UV lamp capillary and the nose of the analyzer are visible. The heater is located behind the sample; radiation shields are used to separate the heater from the nitrogen cooling stage. The entire cryostat is mounted to a rotational feedthrough and can also be translated in the horizontal plane.

to the Joule-Thomson effect and the non-ideal nature of the helium [118]. Since the cooling power due to the Joule-Thomson effect is low, the SPM head is additionally cooled passively by a LHe reservoir at 4 K. It is also surrounded by radiation shields at 4 K and 77 K, cooled by LHe and LN_2 reservoirs respectively. The shields are equipped with small windows and shutters to allow access for cameras and evaporators. The SPM chamber is equipped with a homebuilt dual lithium/calcium evaporator that is able to deposit directly onto the sample inside the head. Pressures in the SPM chamber during measurements are typically on the order of 10^{-10} mbar, maintained by an ion pump and a TSP. The true pressure inside the head, however, is likely lower due to cryopumping by the cryostat shields, allowing the sample surface to stay atomically clean for weeks to months.

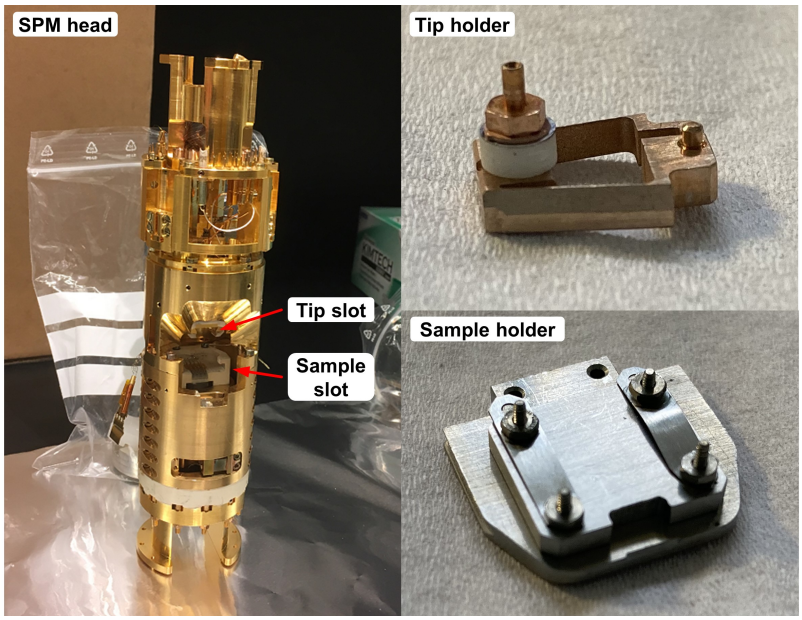

Figure 3.17: Inside the Tesla JT SPM. The SPM head, removed from the instrument, is shown in the left photo. The tip and sample slots are indicated. The corresponding holders are shown on the right.

Inside the SPM head (Figure 3.17), piezoelectric motors ("piezos") are used to position the tip and sample. The "fine" piezo, with a range of a few hundred nm depending on temperature, is used for scanning the tip with sub-angstrom precision; the "coarse" piezo, with a range of several mm, is used to bring the sample up to the tip for scanning, or away from the tip for transferring. Tips and samples are carried by the holders also shown in Figure 3.17. For the STM work described in this thesis, a cut platinum-iridium tip was used; for the AFM work, a Scienta Omicron qPlus sensor (tuning fork type) with an etched tungsten tip was used instead. Samples were mounted to the sample holder using copper paste, silver epoxy, or the built-in molybdenum foil clamps; details are described in Section 3.5. While the instrument can be configured to apply bias to either the tip or the sample, all of the work described in this thesis was done by biasing the tip and grounding the sample. The SPM is also equipped with a superconducting split-pair dry

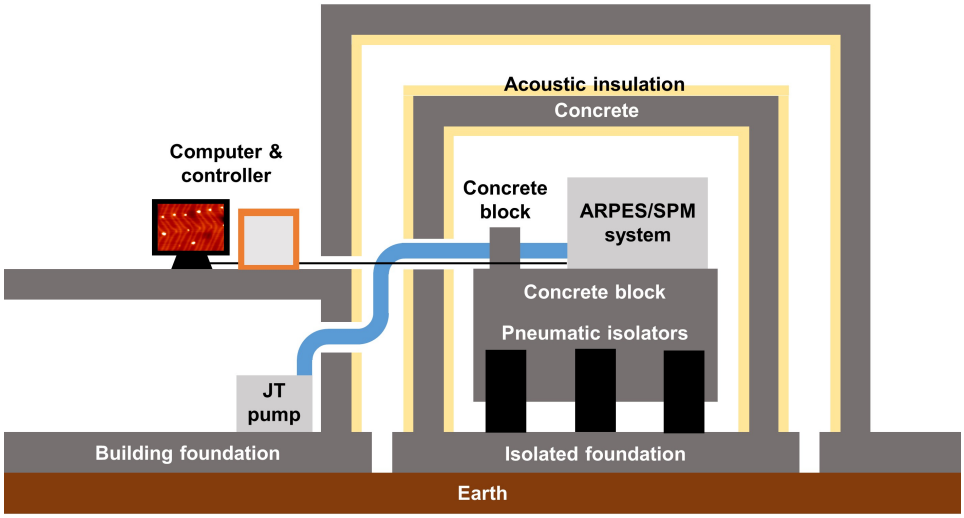

Figure 3.18: Isolation facility schematic. The ARPES/SPM combined system is housed in a room completely decoupled from the rest of the building. A separate foundation, acoustic isolation material, and pneumatic supports all help keep vibrations inside the SPM head at a minimum.

magnet that is capable of providing fields up to ±3 T perpendicular to the sample surface.

Since SPM is highly sensitive to vibrations, the entire system is housed inside an acoustically and mechanically isolated facility (Figure 3.18). The system is placed on a large concrete block supported by pneumatic isolators. The entire room ("pod") is built on a foundation isolated from the rest of the building, and is physically separated by an air gap lined with acoustic insulation. Inside the pod, the walls are also lined with soft material. Since the JT cooling is provided by a scroll pump, the pump itself is housed in a different room and the pumping line is routed through a concrete block to decouple it from the system. The SPM itself is also internally protected from vibration. During operation, the SPM head is suspended inside the cryostat on soft springs, and gold-plated copper fins positioned between magnets provide eddy current damping.

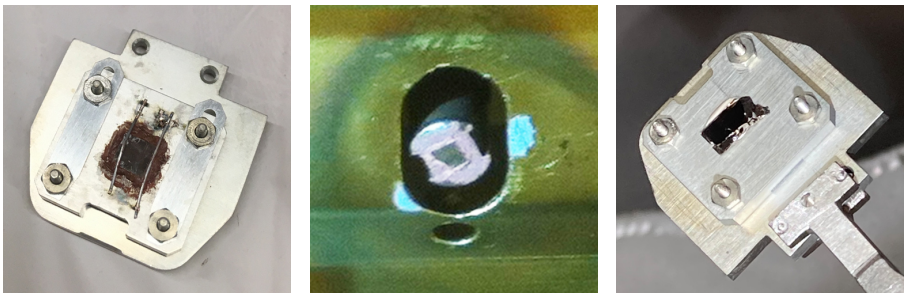

(a) **(b)** **(c)**

Figure 3.19: Sample photos. Some of the samples used in this work. **(a)** MLG/SiC mounted to a Scienta Omicron Tesla JT SPM sample plate. Tantalum wires have been spot welded to the sample plate to protect the sample from falling. **(b)** Gadolinium-intercalated graphene on SiC mounted to a bullet-style sample holder for ARPES. **(c)** A cleaved ZrSiSe sample mounted on a Tesla JT SPM sample plate.

3.5 Samples and preparation

3.5.1 Graphene on SiC

All graphene samples used in this work were grown on silicon carbide (SiC) by the group of Ulrich Starke at the Max Planck Institute for Solid State Research (Figure 3.20). For all samples, commercial 6H-SiC(0001) substrates were first hydrogen-etched to remove polishing damage. Next, the substrates were annealed in an argon atmosphere at 1400°C. After approximately 10 minutes, the sublimation of silicon produces a carbon-rich surface layer which structurally resembles graphene [119, 120]. However, as it is tightly bound to the substrate, this buffer layer does not show any of the distinctive electronic properties of graphene, and is referred to as *zero-layer graphene* (ZLG). From these samples, three types of graphene samples were produced:

1. **Graphene on SiC (Gr/SiC).** To produce a decoupled graphene layer, a second carbon layer is grown by annealing at 1450°C for 10 minutes [119]. The top layer is then decoupled and behaves as monolayer graphene (MLG) both structurally and electronically; the bottom layer

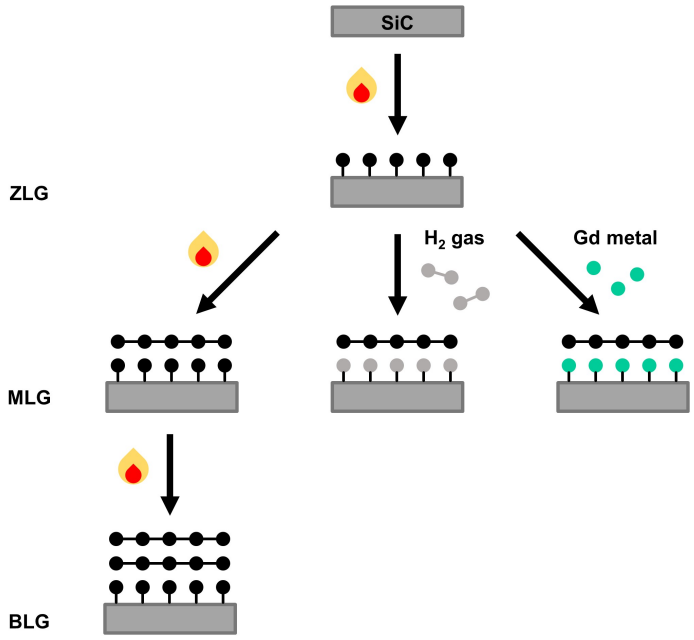

Figure 3.20: Growing graphene. Polished SiC substrates are heated to produce carbon layers by silicon sublimation. The first layer of carbon atoms (ZLG) is bound to the substrate and does not behave like graphene. With further heating, MLG and BLG samples can also be grown. Alteratively, the zeroth layer can also be decoupled from the substrate to form MLG by intercalating hydrogen through annealing in H_2 gas, or gadolinium through evaporation and heating.

remains bound to the substrate. With additional annealing, more carbon layers can be grown to produce bilayer graphene (BLG) and other multilayer graphene samples. Due to charge-transfer doping from the substrate, the Dirac point in these samples is shifted below the Fermi level: in the case of the MLG samples, this is approximately 450 meV.

2. **Hydrogen-intercalated graphene on SiC (Gr/H/SiC).** Another method to decouple the zeroth layer from the SiC substrate is by intercalating other atoms below the buffer layer. In the case of hydrogen, this is done by annealing the graphitized SiC in molecular hydrogen at

atmospheric pressure between 600°C and 1000°C. Unlike the MLG with a buffer layer, the resulting hydrogen-intercalated graphene is slightly hole-doped, with the Dirac point shifted to approximately 100 meV above E_F [52].

3. **Gadolinium-intercalated graphene on SiC (Gr/Gd/SiC).** Alternatively, gadolinium atoms can also be intercalated between the buffer layer and substrate. This is achieved by first depositing gadolinium by electron-beam evaporation while the sample is held at 600°C. Next, the sample is flashed to 1000°C to allow the gadolinium atoms to intercalate below the graphene. In this case, the Dirac point is shifted by about 1.6 eV below E_F [60].

For both ARPES and STM experiments, these samples were mounted to the sample holders using copper paste. As the SiC substrates are insulating, it is important that the copper paste makes direct contact between the graphene and sample holder. Immediately before experiments were performed, the samples were cleaned by annealing in UHV at ∼600°C for several hours.

Lithium was deposited between 5–20 K using a SAES alkali metal evaporator (ARPES experiments) or at 2 K using an AlfaVakuo AlfaSource lithium metal vapour source (STM experiments). A shutter (ARPES) or radiation shield (STM) was used to control the rate and time of deposition.

3.5.2 Samples for testing and calibration

1. **Gold film on mica (Au/mica).** A commercial gold-coated mica sample (provided by Scienta Omicron GmbH) was used to test both the ARPES and STM systems, as well as tip treatment in STM experiments. These samples consist of a thin layer (typically a few hundred nm) of gold evaporated onto a cleaved mica substrate. The resulting surface tends to show the Au(111) orientation with its characteristic $22 \times \sqrt{3}$ "herringbone" reconstruction [121], making it a cheaper alternative to a single crystal Au(111) sample.

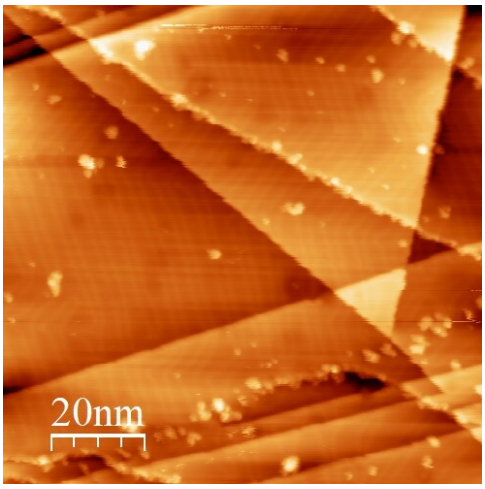

Figure 3.21: Au(111) on mica. Typical Au/mica topography as seen in STM. While the gold on these samples is polycrystalline, the Au(111) orientation is preferred, and the characteristic "herringbone" reconstruction is commonly observed.

This sample was cleaned by repeated argon sputtering and annealing in a different UHV system followed by transfer in air. It is annealed an additional time after transfer into vacuum for ~ 2 hours around 200°C to 300°C.

2. **Polycrystalline gold.** Polycrystalline gold was used to both calibrate the ARPES data and treat the tip in STM measurements.

   For ARPES measurements, a gold-coated bullet with a flat end was used. A fresh layer of gold ($\sim$1 nm thick) was deposited on the surface using an *e*-beam evaporator after transfer into vacuum.

   For STM measurements, a small strip of ultra-high purity gold was flame-annealed with a hydrogen torch in air, mounted to a sample plate, then annealed again around for ~ 2 hours around 200°C to 300°C in vacuum.

3. **Zirconium silicon selenide (ZrSiSe).** A ZrSiSe sample was used to test the Scienta Omicron ARPES system. It was grown by chemical

vapour transport (CVT) starting from stochiometric mixtures of Zr, Si, and Se powder [122], and cleaved in vacuum shortly before the experiment.

4. **Sodium chloride (NaCl).** An NaCl crystal was used to test the AFM capabilities of the Scienta Omicron Tesla JT SPM, chosen for its insulating behaviour. It was cleaved using a razor blade immediately before entry into vacuum and annealed to remove adsorbed water before the experiment.

Chapter 4

Testing & characterization of a commercial ARPES/SPM combined system

In condensed matter physics, scientists often use an assortment of characterization techniques to study different aspects of a sample. ARPES and SPM, for example, are two commonly used techniques which provide complementary information on the electronic properties of a material: while ARPES probes the behaviour of electrons in momentum space, SPM is used to discern a spatially-resolved picture. However, due to the high degree of variability associated with many sample growths and preparations, it is often challenging to reconcile the results from different techniques.

To resolve such issues, we commissioned Scienta Omicron GmbH to design and produce a single UHV system capable of both ARPES and SPM, so that the exact same sample, following the exact same preparation, can be characterized using both techniques. This combined system, described in Section 3.4.2, was installed and tested between March and October 2019. In this chapter, we detail the testing process and present preliminary data taken using both ARPES and SPM.

4.1 Acceptance criteria

As part of the commissioning process, a list of acceptance criteria to be demonstrated during the installation was agreed upon. In this section, we detail these criteria and the related tests.

4.1.1 System

Pressure below 3×10^{-10} mbar in ARPES and SPM chambers

After the initial assembly and pumpdown using scroll and turbo pumps, the entire system is baked at temperatures above 120°C to remove adsorbed water and obtain UHV pressures. For this purpose, a bakeout tent containing built-in fan heaters is provided; using thermocouples attached to the system, the Mistral system controller is able automate the baking process.

The ARPES and transfer chambers, equipped with their own turbo pumps, can be baked independently; the SPM chamber can only be baked in conjunction with the transfer chamber. While the ARPES and transfer chambers can typically obtain good pressures after approximately 48 hours at 140°C, the SPM chamber requires at least 60 hours at 120°C. The reduced temperature is due to the sensitivity of the superconducting magnet to temperature gradients; a longer time is required as the SPM head is located inside the insulating cryostat and can only be heated using pumps to draw hot air through the liquid nitrogen and helium reservoirs.

After bakeout (typical pressures: 10^{-7} mbar at bakeout temperature, 10^{-9} mbar at room temperature), TSPs and ion getter pumps are used to further reduce the pressure in the system. This typically results in pressures in the low 10^{-10} mbar range. At this point, the turbo and roughing pumps can be switched off, and only the ion getter pumps are required to maintain UHV conditions.

Sample/tip transfer

The sample and tip holders are shown in Figure 3.17. The sample holder is held by the two small holes on its edge, which correspond to two sets

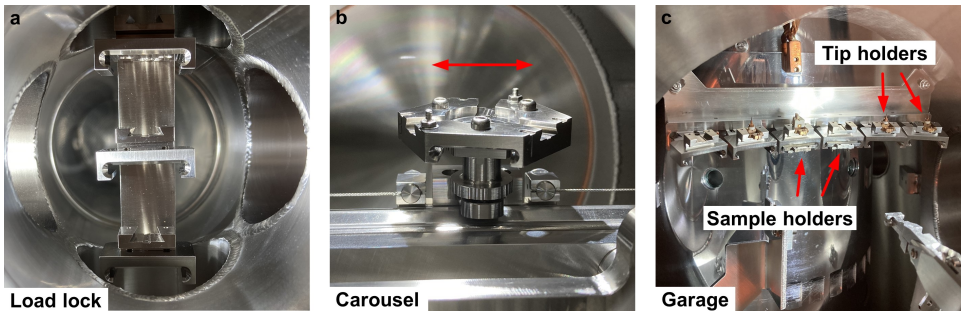

Figure 4.1: Sample and tip storage. (a) Sample and tip/sensor storage in the load lock. Sample holders fit into the wider slots facing down; tip holders fit into the smaller slots pointing up. Up to three samples and three tips can be stored here. **(b)** Storage in the transfer chamber. The carousel can store up to three samples and three tips. It can be rotated using a wobblestick or moved along the rail using a rotational feedthrough. The rail itself can be docked inside either the ARPES or Tesla chambers for sample/tip transfer. **(c)** UHV storage in the Tesla chamber. Up to six samples and six tips can be stored here. The wobblestick jaws are also visible (bottom right).

of "teeth" in the wobblestick jaws. The tip holder instead has a protruding centre pin, corresponding to a hole in the wobblestick jaws.

Samples and tips are introduced to the system through a load lock, which can hold up to three samples and three tips (Figure 4.1(a)). After pumpdown, the samples/tips can be lowered into into the transfer chamber, where a wobblestick is used to pick up the samples/tips and transfer them to a rotating carousel also capable of holding up to three samples and three tips (Figure 4.1(b)). The carousel moves along a long horizontal rail, which can be docked inside either the ARPES or SPM chambers. In each chamber, a wobblestick is used to transfer again to either the ARPES manipulator (sample only) or the SPM head, which can be locked in two different positions for sample and tip transfer. Additionally, the SPM chamber has a garage capable of storing up to six samples and six tips in UHV conditions (Figure 4.1(c)).

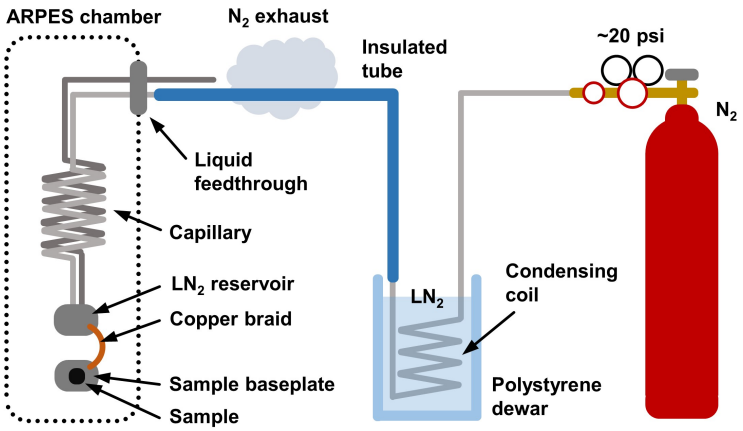

Figure 4.2: Cooling the ARPES manipulator. N_2 gas at approximately 20 psi is forced through a condensing coil submerged in LN_2, then into the ARPES chamber through an insulated inlet tube. Here, LN_2 is collected in a reservoir, which cools the sample baseplate through a thermally conductive copper braid.

4.1.2 ARPES module

Sample cooling: below 160 K

The ARPES manipulator can be cooled using LN_2 (Figure 4.2). First, N_2 gas is pushed through a condensing coil at approximately 20 psi. The condensing coil sits inside a polystyrene dewar filled with LN_2. After passing through the coil, the N_2 gas becomes liquid and enters the system through an insulated inlet tube. Inside the system, the LN_2 is forced through a capillary into a reservoir. Here, temperatures can reach as low as 100 K, and conductive copper braiding is connected to the sample baseplate, resulting in temperatures as low as 120 K after approximately 30 minutes. This corresponds to a temperature of approximately 150 K at the sample itself.

Sample heating: above 1100 K

The ARPES manipulator is also equipped with two heating modes for sample preparation. In resistive mode, a current is passed through a 30 Ω pyrolytic

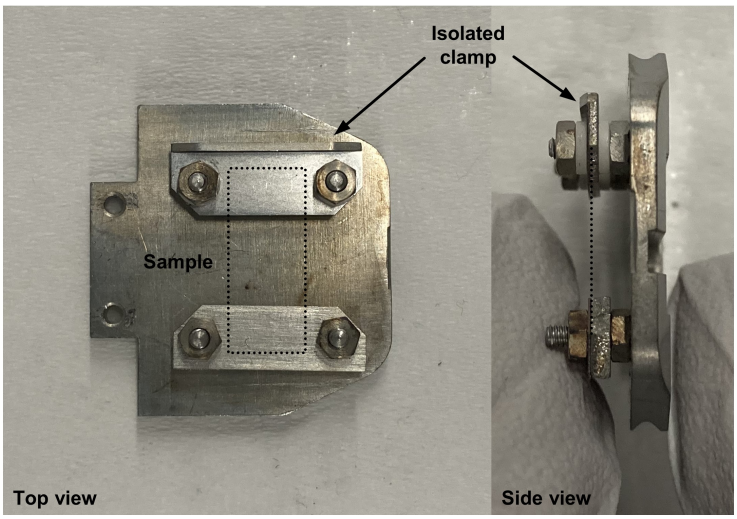

Figure 4.3: Direct heating sample plate. A special sample plate where the two foil clamps on each end of the sample (dotted lines) are electrically isolated from each other. The sample can be heated by passing a current directly through the sample.

boron nitride (PBN) heater situated behind the sample. The heater is capable of outputting up to 100 W of power (110 W temporarily), producing temperatures over 600°C at the sample baseplate, corresponding to 900°C at the sample itself.

In direct current mode, a special sample plate (Figure 4.3) is used where one of the foil clamps used to fasten the sample is electrically isolated from the rest of the sample plate. A metal brush on the manipulator makes contact with the clamp, allowing a current to be passed directly though the sample. In this mode, up to 60 V can be applied, with the output power and resulting temperature a function of the sample resistance. Thus, direct current mode is intended for use with semiconducting samples.

Measurement of the Fermi edge on a polycrystalline metal sample

The ARPES chamber is equipped with a FOCUS VUV Source HIS 13 discharge lamp and a Scienta Omicron R3000 Hemispherical Analyzer. In

our lab, the HIS 13 is operated with helium gas to produce either He I (21.2 eV) or He II (40.8 eV) photons, although other discharge gases (neon, argon, krypton, xenon, or hydrogen) can be used as well [123].

The electron analyzer is equipped with six entrance slits of varying widths, with larger slits producing higher count rates but at a cost in energy resolution. Five different lens modes are available: transmission mode for ultraviolet photoelectron spectroscopy (UPS), and four angular modes (acceptance angles of $\pm 10°, \pm 7.5°, \pm 5°, \pm 3°$) for ARPES. Additionally, the analyzer can be operated in fixed or swept energy mode: in fixed mode, a snapshot of the detector is taken for a small, fixed energy range (approximately 10% of the pass energy), while in swept mode, the pass energy window is swept through a range specified by the user. While fixed mode is faster, swept mode is able to provide a larger energy range and reduces detector effects [124].

For a first test of the lamp and analyzer, UPS data on a polycrystalline silver sample at room temperature was collected in transmission and swept energy modes using the largest entrance slit. Figure 4.4(a) shows an overview spectrum taken using a pass energy of 5 eV with 50 meV steps, while (b) details the range indicated by the grey box using a pass energy of 2 eV with 5 meV steps. While the overall shape resembles that of a silver valence band spectrum, featuring an intense d-band a few eV below the Fermi energy [125], there are several issues with this spectra.

First, the Fermi level is located at a kinetic energy of approximately 29 eV, which corresponds to neither He I (21.2 eV) or He II (40.8 eV) photons minus an analyzer work function of approximately 5 eV. The intensity does not decay immediately above E_F, instead persisting for approximately 3 eV. Additionally, the d-band should begin approximately 4 eV below E_F [125], while in this spectrum it is approximately 7 eV away. This is also accompanied by some shifting of the E_F between measurements: in Figure 4.4(a), for example, E_F corresponds to a kinetic energy of approximately 29.1 eV, while in Figure 4.4(b), it is at approximately 28.6 eV.

All of the above suggests issues with the electrical connections to the sample. However, the sample is securely grounded, not only directly but also through the 30 Ω PBN heater (all heater contacts are grounded during

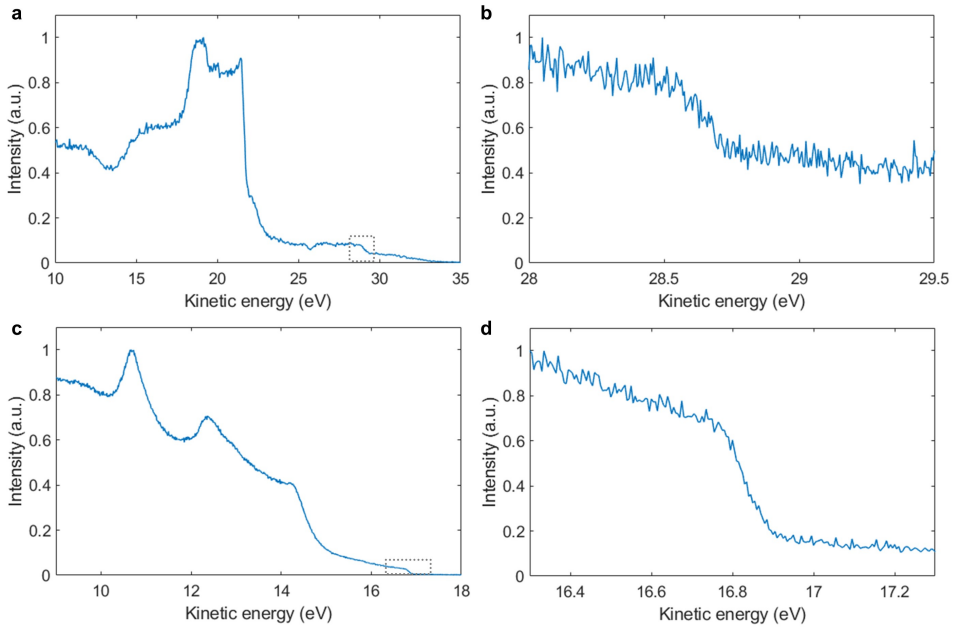

Figure 4.4: UPS and measurement of the Fermi edge. (a) Initial UPS measurement on polycrystalline silver. A Fermi edge is observed at approximately 28.7 eV, and the silver *d*-band is observed between 18–22 eV. However, these numbers do not correspond to either He I (21.2 eV) or He II (40.8 eV) photons. Additionally, a long tail of intensity is observed above the Fermi level. **(b)** Spectra taken in the energy range indicated by the grey box in (a). A Fermi edge is observed, but with high intensity above the Fermi level. **(c)** UPS measurement on polycrystalline gold after repairing grounding issues. The Fermi edge appears at approximately 16.8 eV, corresponding to the He I line minus the analyzer work function. While the background is high, the gold *d*-band appears at the correct energy relative to the Fermi level. **(d)** Spectra taken in the energy range indicated by the grey box in (c). A clear Fermi edge is observed, with low intensity above the Fermi level.

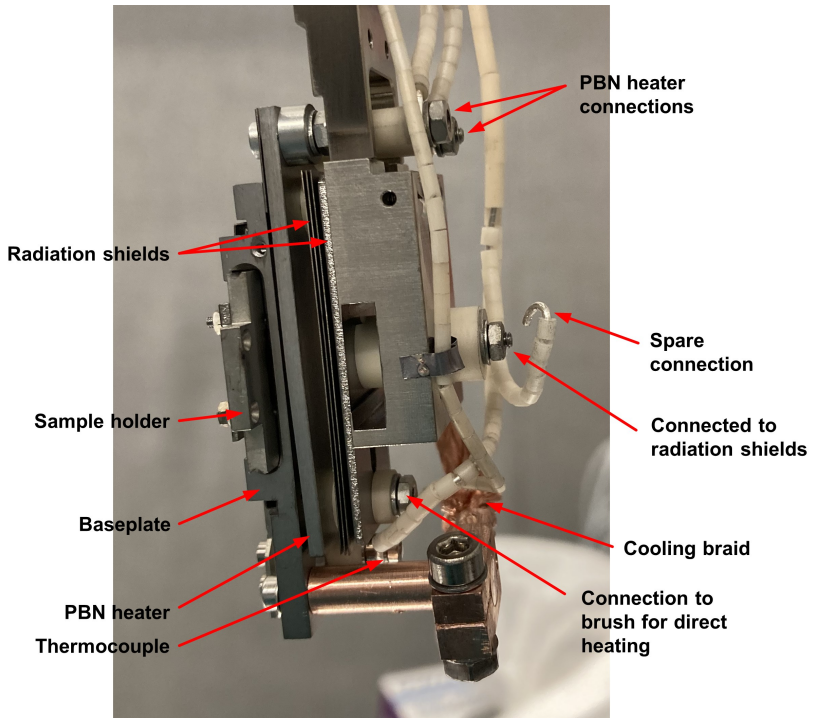

Figure 4.5: Connections at the ARPES manipulator. During ARPES experiments, all heater connections (both PBN heater connections, brush for direct heating, spare) are grounded. However, the radiation shields and thermocouple were not initially grounded, leading to issues with the detected electron energy. These issues were resolved by grounding the radiation shields through the spare connection and the thermocouple connections outside the chamber.

ARPES experiments). On closer inspections of the manipulator connections (Figure 4.5), we found that the four metal plates directly behind the PBN heater, intended for radiation shielding, are electrically isolated from the rest of the manipulator and left floating. This results in the shields becoming charged during ARPES experiments, generating electric fields near the sample and thus affecting the flight of electrons towards the analyzer. Fortunately, a spare connection was available for connecting to these radiation shields, which can then be grounded outside the chamber during ARPES experiments.

A second issue is the small voltage generated by the thermocouple, which is electrically connected to the sample baseplate, when the manipulator is heated or cooled. This is easily fixed by grounding both thermocouple contacts outside the chamber.

After resolving these two issues, we repeated the UPS experiments on a polycrystalline gold sample at room temperature, using transmission and swept energy modes, the smallest entrance slit, and a pass energy of 2 eV. Figure 4.4(c) shows an overview spectrum taken with 10 meV steps, while (d) details the range indicated by the grey box with 5 meV steps. The Fermi edge now appears at a kinetic energy of approximately 16.8 eV, corresponding to He I line minus the analyzer work function. The gold *d*-band is also at the correct energy range, beginning approximately 2 eV below E_F [126]. The relative intensity above E_F is much lower than before, without a tail; the remaining intensity is due to the He II line, which is always present at a lower intensity since the UV lamp is not equipped with a monochromator [123].

4.1.3 Tesla JT SPM module

Microscope head cooling: below 1.2 K

The Tesla JT SPM is capable of operating at temperatures as low as 1 K at the head. This is accomplished using a combination of LN_2, LHe, and the Joule-Thomson effect, in which a non-ideal fluid throttled through an impedance produces a temperature change [118]. In this case, helium gas is pushed through a narrow capillary at approximately 3 bar, such that it cools and liquefies. This liquid helium is then collected in a small reservoir with pressures around 0.1–0.01 mbar (maintained by a roughing pump), which then cools the SPM head and the surrounding 1 K shield (Figure 4.6).

The Joule-Thomson effect, however, only cools helium at cryogenic temperatures and produces heat instead at room temperature. Thus, the JT stage and SPM head are first cooled to 4 K by connecting a thermal switch to the LHe reservoir (Figure 4.6). (In practice, LN_2 is used first to cool to

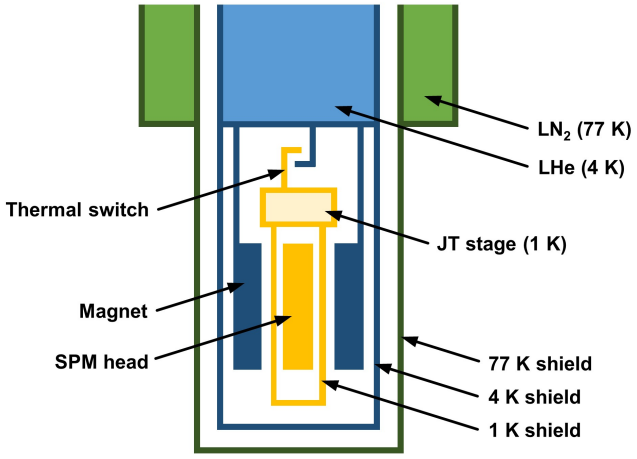

Figure 4.6: Cooling the SPM cryostat. The various stages of cooling inside the cryostat are indicated by different colours: 77 K (green), 4 K (blue), and 1 K (yellow). The entire 1 K stage (JT stage, SPM head, 1 K shield) can be moved up and down to connect or disconnect the thermal switch to the LHe reservoir: it is first cooled to 4 K by connecting the thermal switch, then further cooled to 1 K by disconnecting. The LHe reservoir also cools the superconducting magnet and the 4 K shield surrounding the magnet and 1 K stage. The LN_2 reservoir cools the 77 K shield surrounding the the 4 K shield.

77 K, then removed before further cooling with LHe.) At this point, the thermal switch can be disconnected and the JT stage will further cool the head to 1 K.

The LHe reservoir additionally cools the superconducting magnet, as well as a second radiation shield surrounding the JT stage, SPM head, and magnet to 4 K. All of the above is further enclosed by a third radiation shield held at 77 K by the LN_2 reservoir. A diagram showing the various cooling mechanisms and radiation shields is shown in Figure 4.6.

In this way, our system was able to reach a temperature of 0.996 K at the JT stage and 1.001 K at the SPM head (as measured by a Cernox sensor). It is also possible to cool by an additional $\sim$20 mK for several hours by first filling the 1 K reservoir, then pumping both sides of the JT impedance until

the reservoir is emptied. Even lower temperatures can be obtained using ^{3}He gas.

Superconducting magnet operation: 3 T for more than 2 hours

The SPM is equipped with a superconducting split pair magnet capable of producing a field of up to ±3 T perpendicular to the sample surface.

When the magnet is powered on for the first time after cooling down, the superconducting coils can shift slightly due to the high fields. The movement can result in the magnet transitioning to the normal state in what is called a *quench* below the maximum operating field, resulting in rapid heating due to the high currents involved. Thus, the magnet power supply must be equipped with quench protection, which quickly reduces the current to 0 in the event that a quench is detected.

If such a quench were to occur during normal scanning operation, with the SPM head hanging freely, significant damage can occur. To prevent this, the magnet must be conditioned ("trained") after each cooldown, in which the head is locked and the field is slowly ramped up repeatedly until it can reach the maximum field (3 T) plus a safety margin (0.03 T) without quenching. When the magnet quenches, it can heat to temperatures as high as 40 K, so it must be allowed to cool before ramping again. Typically, four or five quenches occur during the training process. Once the field has reached ±3.03 T and remains stable for approximately 20 minutes, the training process is complete. At this point, the field can be ramped back to 0 T, the head can be unlocked to hang freely, and it is safe to work at fields of up to ±3 T for long periods of time. However, the field must be reduced to zero for cryogen refilling and opening the heat shields.

STM: atomic resolution on Au(111) below 1.2 K, at 0 and 3 T and during field ramping

A demonstration of STM operation at zero field is performed on the Au(111) surface of a Au/mica sample. The sample surface is first prepared by repeated cycles of sputtering with argon and annealing in a different UHV system

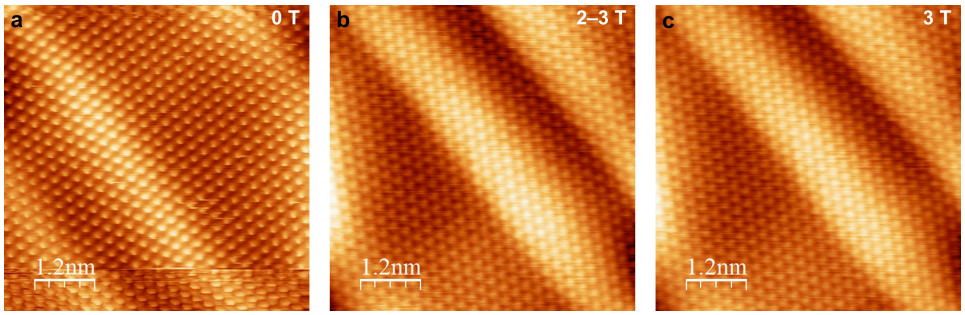

Figure 4.7: STM operation on Au(111). (a) Atomic resolution on Au(111) at 0 T, taken in constant-current mode with a bias of 0.28 V and a set current of 1 nA. The characteristic Au(111) herringbone reconstruction is visible. A tip change occurs near the bottom of the image. **(b)** The same image as (a) during ramping of the magnetic field from 2 T to 3 T, taken with a bias of 0.12 V and a set current of 1.5 nA. Note that some drift has occurred. **(c)** The same image as (a) and (b) at 3 T, taken with a bias of 0.12 V and a set current of 1.5 nA.

before quickly transferring to the ARPES/SPM system through air. Here, it is annealed one more time in the ARPES manipulator at ∼200°C for about 30 minutes, then allowed to cool before transferring into the SPM head.

Since the ARPES/SPM system is not equipped with tools for tip treatment, a cut Pt-Ir tip is used for these tests. It is treated on the Au(111) surface by a combination of controlled contact with the sample and pulsing the bias voltage until atomic resolution can be observed. Figure 4.7(a) shows an image of the surface taken in constant-current mode (V_{bias} = 0.28 V, I_{set} = 1 nA).

The STM can also be operated normally at a magnetic field of 3 T (Figure 4.7(b), V_{bias} = 0.12 V, I_{set} = 1.5 nA), or even during ramping (Figure 4.7(c), V_{bias} = 0.12 V, I_{set} = 1.5 nA). Some drift of the tip position can occur during ramping, so the tip height should be set to approximately the centre of its range before ramping in order to avoid crashing or moving out of tunnelling range. At high fields, the magnet also produces a similar effect as the eddy current damping mechanism, and mechanical noise tends to be reduced.

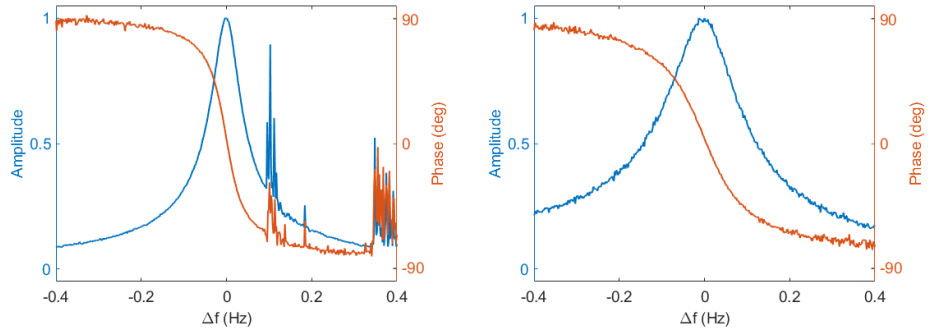

Figure 4.8: Resonance characteristics of a qPlus sensor. (a) Amplitude (blue) and phase (orange) of a qPlus sensor as a function of frequency shift off-resonance, $\Delta f = f - f_0$, at 0 T. Here f_0 is 24.752 kHz, corresponding to a quality factor of $Q = 2.21 \times 10^5$. **(b)** The same frequency dependence as (a) at 3 T. Here f_0 is shifted slightly to 24.772 kHz. The amplitude peak is broadened, corresponding to $Q = 9.36 \times 10^4$. The quality factor is reduced due to damping by the high magnetic field.

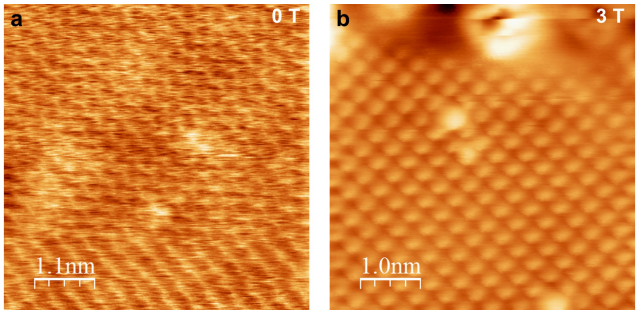

Figure 4.9: AFM operation on NaCl(100). (a) Atomic resolution on NaCl(100) at 0 T, taken in constant Δf mode with a set point of -1 Hz. **(b)** The same image as (a) 3 T, taken at a different location. Note that the additional magnetic field significantly dampens noise in the image.

AFM: atomic resolution on NaCl(100) below 1.2 K, at 0 and 3 T

AFM operation is demonstrated in non-contact mode using a non-conducting NaCl(100) crystal and a qPlus sensor with an etched tungsten tip.

The NaCl crystal is cleaved using a razor blade and clamped to a sample plate immediately before it is introduced to vacuum. It is annealed at ∼250–300°C for about 1 hour, then allowed to cool before transferring into the SPM head.

Before approaching the sample surface, the resonance characteristics of the qPlus sensor must be determined. At 0 T (Figure 4.8(a)), the qPlus sensor used had a resonant frequency of 24.752 kHz. The FWHM of the resonance peak is approximately 0.112 Hz. From this, we obtain a quality factor of $Q = 2.21 \times 10^5$. A high quality factor is important, since it determines the minimum frequency shift that can be detected. At 3 T (Figure 4.8(b)), the resonance frequency shifts slightly to 24.772 kHz, with a broader FWHM of 0.265 Hz due to interaction with the magnetic field. This results in a reduction of the quality factor to $Q = 9.36 \times 10^4$, but atomic-scale imaging can nevertheless be performed.

Images of the NaCl(100) surface are collected at 0 T (Figure 4.9(a)) and 3 T (Figure 4.9(b)). Both are taken in constant Δf mode, with a set point of -1 Hz (a higher shift of the resonant frequency corresponds to a shorter distance to the sample surface). Since qPlus operation relies on the vibration of the tip, it must be scanned very slowly (<1 nm/s) so that any effects of the motion has time to dampen. This also means that qPlus is particularly sensitive to noise in the system, which is more evident at 0 T but is significantly dampened at 3 T due to the presence of the field.

4.2 Additional tests

In addition to the required acceptance criteria, we performed several other tests to characterize the functionality of the system. They are detailed in this section.

4.2.1 UPS: energy resolution

For any spectroscopy technique, one of the most important specifications of the system is energy resolution, which (along with temperature) determines the smallest features that can be observed. For photoemission spectroscopy,

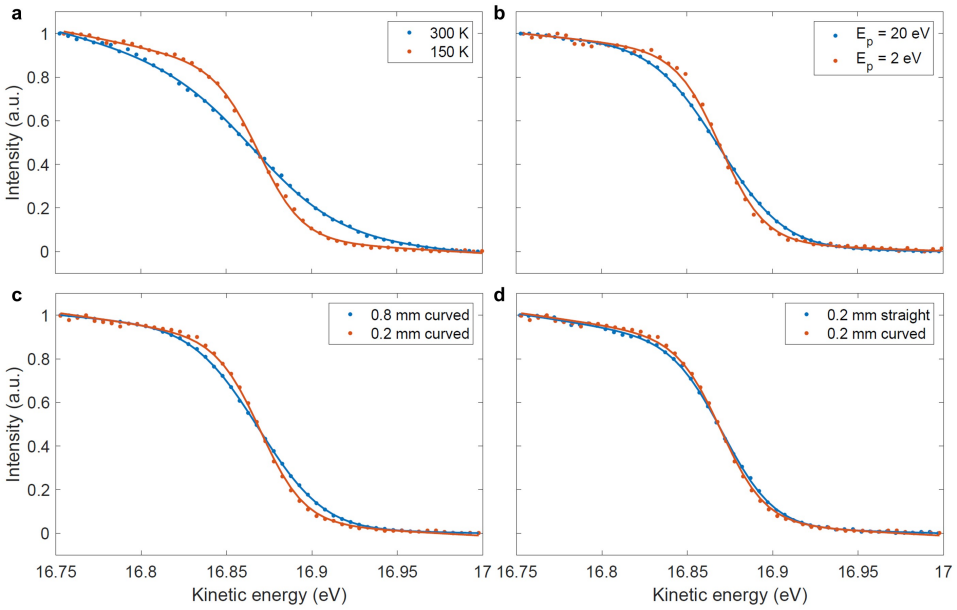

Figure 4.10: Factors affecting energy resolution. **(a)** Fermi edge taken at 300 K (blue) and 150 K (orange), using the 0.2 mm straight slit and $E_p = 20$ eV. The Fermi edge is broadened by k_BT. The intensity is fit to Equation 4.1, without considering resolution effects. **(b)** Fermi edge taken at 150 K using $E_p = 20$ eV (blue) and 2 eV (orange), with the 0.8 mm curved slit. The resolution for 2 eV is negligible compared to temperature effects, while for 20 eV it is approximately 21 meV. **(c)** Fermi edge taken at 150 K using the 0.8 mm (blue) and 0.2 mm (orange) curved slits, with $E_p = 20$ eV. The resolution for the 0.2 mm slit is negligible, while for the 0.8 mm slit it is approximately 21 meV. **(d)** Fermi edge taken at 150 K using the 0.2 mm straight (blue) and curved (orange) slits, with $E_p = 20$ eV. The resolution for the curved slit is negligible, while for the straight slit it is approximately 11 meV.

energy resolution can be estimated by studying the Fermi edge on a normal metal, which is a step function at zero temperature and infinite resolution but broadens with increasing temperature and decreasing resolution. If the temperature is known, then the remaining broadening can be attributed to system resolution.

Since the ARPES manipulator can only be cooled to ∼150 K, temperature is a major contributor to broadening effects in this system. Figure 4.10(a) compares the Fermi edge collected on a polycrystalline gold sample at 300 K (blue) and 150 K (orange), both using the 0.2 mm straight slit and $E_p = 20$ eV. The intensity I is fit to the form

$$I(E_{kin}) = \frac{AE_{kin} + B}{e^{(E_{kin}-E_F)/k_BT} + 1} + CE_{kin} + D, \tag{4.1}$$

where E_{kin} is the electron kinetic energy, E_F is the Fermi energy, and $AE_{kin} + B$ and $CE_{kin} + D$ empirically fit the slopes and intercepts above and below E_F, respectively. Here we have not yet taken into account the effects of system resolution, but the Fermi edge is broadened by $k_BT = 26$ meV at 300 K and 13 meV at 150 K due to temperature only.

To account for resolution effects, we convolve Equation 4.1 with a Gaussian distribution with standard deviation ΔE:

$$I(E_{kin}) = \left[\frac{AE_{kin} + B}{e^{(E_{kin}-E_F)/k_BT} + 1} + CE_{kin} + D\right] * \left[\frac{1}{\Delta E\sqrt{2\pi}}\, e^{-\frac{E_{kin}^2}{2\Delta E^2}}\right]. \tag{4.2}$$

By fixing T and fitting for ΔE, we can estimate the resolution of the system.

The theoretical energy resolution of the analyzer is approximated by

$$\Delta E \propto \frac{sE_p}{r}, \tag{4.3}$$

where s is the width of the entrance slit, E_p is the pass energy (the range of energies allowed to pass through the analyzer) and r is the analyzer mean radius [124]. While the analyzer radius cannot be easily altered, we can observe the effects of E_p and slit width.

Figure 4.10(b) compares the Fermi edge at 150 K using $E_p = 20$ eV (blue) and 2 eV (orange), both using the 0.8 mm curved slit. The fitted ΔE is 21 meV for $E_p = 20$ eV and <1 meV for $E_p = 2$ eV. Note that this does not necessarily mean the resolution is <1 meV, but the resolution effects are negligible in comparison to the 13 meV due to thermal broadening. Meanwhile, Figure 4.10(c) compares the 0.8 mm (blue) and 0.2 mm (orange)

Slit			Pass energy (eV)			
Position	Width (mm)	Shape	2	5	10	20
1	0.2	Straight	1.1	3	6	11
2	0.2	Curved	0.5	1.3	3	5
3	0.4	Curved	1.1	3	5	11
4	0.8	Curved	2	5	11	21
5	1.3	Straight	7	18	36	72
6	3.0	Straight	17	41	83	165

Table 4.1: ARPES energy resolution estimates. The energy resolution of the ARPES system is estimated in meV for each combination of slit and pass energy. Resolution estimates obtained from fitting are shaded in blue; the rest are calculated using Equation 4.3. At 150 K, with a thermal broadening of ∼13 meV, the grey-shaded settings should not be used as they do not provide any meaningful increase in resolution for a cost in intensity.

curved slits, both using $E_p = 20$ eV (the blue data sets in (b) and (c) are identical). The fitted ΔE for the 0.2 mm curved slit is <1 meV.

An additional parameter that affects the resolution is the shape of the entrance slit. Due to the spherical shape of the analyzer, a straight slit is imaged as a curved line on the detector. When the slit is narrow, this can significantly affect the resolution. To eliminate this effect, some of the slits are slightly curved so that they are imaged as a straight line [124]. Figure 4.10(d) compares the 0.2 mm straight (blue) and curved (orange) slits, both using $E_p = 20$ eV (the orange data sets in (c) and (d) are identical). The fitted ΔE is 11 meV for the straight slit and <1 meV for the curved slit.

From these fitted values for ΔE and Equation 4.3, we can estimate the resolution for all combinations of slit and pass energy. These estimates are shown in Table 4.1, with values obtained from fitting shaded in blue. Note that the resolution is likely underestimated for the wider straight slits, since the effect of the straight slit is more pronounced for narrow slit widths. At 150 K, the grey-shaded settings should be avoided, since any increase in resolution they can provide is washed out by thermal broadening. Among the remaining combinations, a higher pass energy should be selected over a wider slit for higher intensity, since intensity scales as s but E_p^2 (Figure 4.11).

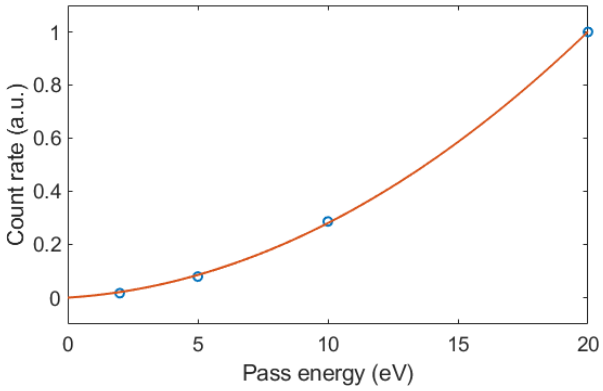

Figure 4.11: Count rate as a function of pass energy. Photoelectron count rate scales linearly with slit width, but quadratically with pass energy. However, resolution scales linearly with both, so given the option, a higher pass energy should be used over a wider slit.

Additionally, the estimated resolution for the 0.2 mm curved slit can be compared to the manufacturer's factory test results: 1.2, 3.4, 7.2, and 14.5 meV for pass energies of 2, 5, 10, and 20 eV, respectively. Since we estimate higher resolutions, other factors (e.g. the acceptance angle of the analyzer, the non-monochromatized UV source) likely contribute to the factory test resolution. However, it is impossible for us to confirm these values without the ability to cool the sample to a significantly lower temperature.

4.2.2 ARPES: Au(111) surface state, ZrSiSe

To test the "angle-resolved" part of the ARPES module, we studied two samples with known bandstructures: the Au(111) surface on Au/mica and ZrSiSe. These samples were selected for simple preparation (annealing or cleaving only) and the presence of bands near Γ (since the ARPES manipulator can only rotate in one direction).

The Au/mica sample was prepared as in Section 4.1.3. The paraboloidal Au(111) surface state is clearly visible in Figure 4.12, in good agreement with the existing literature [127]. Figure 4.12(a) shows a single energy-momentum cut through $k_x = 0$, while Figure 4.12(b) shows half of the circular Fermi

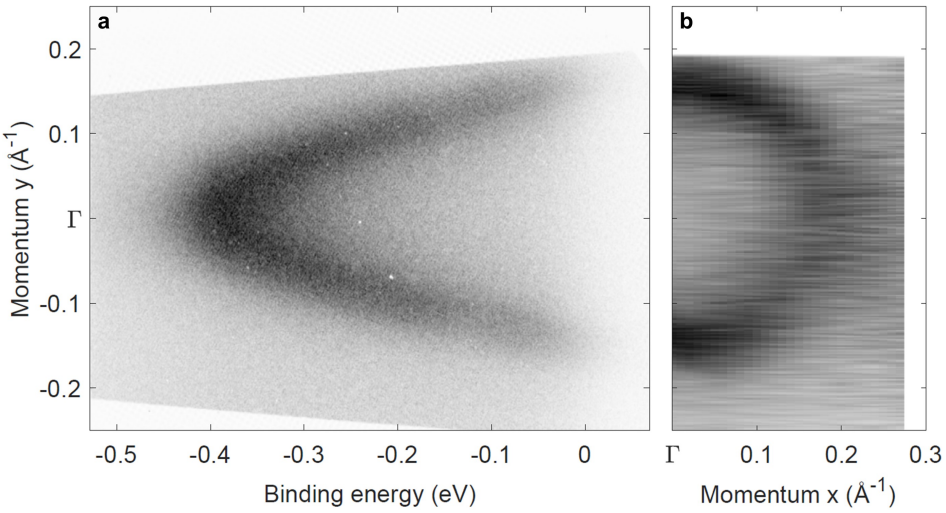

Figure 4.12: Au(111) surface state probed by ARPES. (a) Energy-momentum cut through the paraboloidal Au(111) surface state, taken at $k_x = 0$. **(b)** Fermi surface near Γ showing half of the circular electron pocket.

surface. These spectra were taken at room temperature in A10 angular mode and fixed energy mode, using the 0.8 mm curved slit and $E_p = 5$ eV.

The ZrSiSe crystal was cleaved in vacuum immediately before the ARPES experiment. A single cut through the square Fermi surface pocket near Γ is shown in Figure 4.13(a), with the cut position indicated by the orange dotted line in Figure 4.13(b). A small part of the Fermi surface is also shown in Figure 4.13(b), with its position relative to the pocket (blue dotted lines) indicated by the schematic. These features are also in agreement with the literature [128]. These spectra were taken at room temperature in A20 angular mode and fixed energy mode, using the 0.8 mm curved slit and $E_p = 20$ eV.

4.2.3 STS: Au(111) surface state

We also tested the spectroscopic capabilities of the SPM module by collecting STS curves on the Au(111) surface of the Au/mica sample. Figure 4.14(a) shows the $I(V)$ curve (corresponding to the integrated local DOS) obtained by sweeping the bias between −1 V and 1 V, averaged over 10 iterations. A

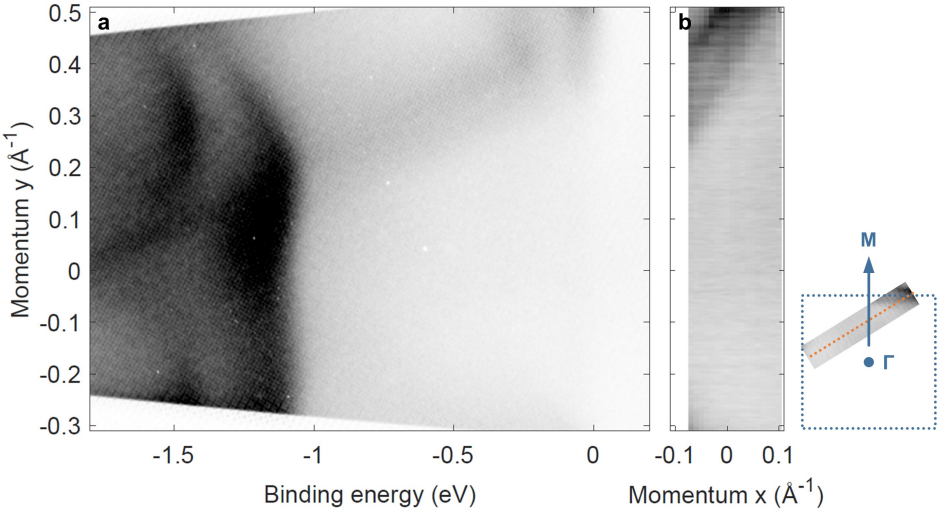

Figure 4.13: ZrSiSe bandstructure probed by ARPES. (a) Energy-momentum cut taken at the orange dotted line in (b). **(b)** Fermi surface showing part of the pocket near Γ. The position of the area shown is indicated by the schematic, with the square pocket near Γ shown by the blue dotted lines.

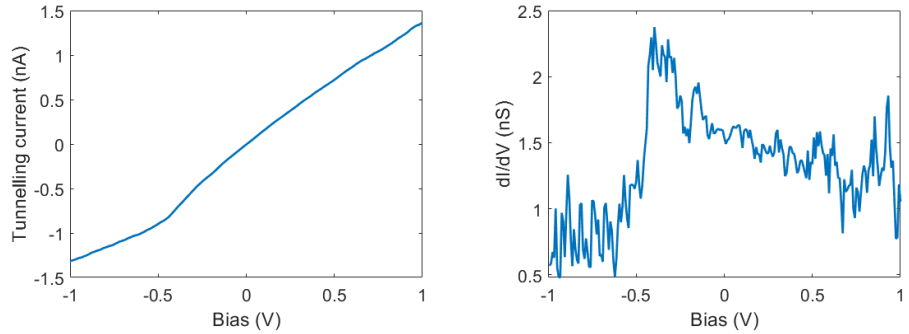

Figure 4.14: STS reference measurement. (a) $I(V)$ curve taken on the Au(111) surface, averaged over 10 iterations. A kink is visible just above -0.5 V. **(b)** dI/dV calculated from (a). The peak just above -0.5 V corresponds to the Au(111) surface state.

change in slope is observed just above −0.5 V, corresponding to the Au(111) surface state. Figure 4.14(b) shows the dI/dV curve (corresponding to the local DOS), calculated from the curve in (a). Here the Au(111) surface state appears as a step just above −0.5 V, matching both the ARPES results in Section 4.2.2 and other STS results in the literature [129].

4.2.4 Lithium evaporation on Au(111)

Alkali and earth alkali metals are often used to donate electrons or otherwise modify a sample. However, it can be difficult and time-consuming to swap the evaporator material in a UHV system. Thus, we built a dual-source evaporator capable of dispensing either lithium or calcium depending on which leads are connected. A 3D model of the design is shown in Figure 4.15. At the end of the evaporator, a Macor blinder separates the two sources (obtained from AlfaVakuo e.U.) to prevent cross-contamination.

The lithium dispenser was tested on Au(111). An STM topograph taken after 3 minutes of lithium evaporation is shown in Figure 4.16(a). We observe that the lithium prefers the "elbows" of the Au(111) herringbone reconstruction and tends to form clusters. The smallest lithium spots are ∼1.3 Å tall, which may correspond to a single lithium atom. A height profile through several of these spots is shown in Figure 4.16(b). The larger spots and clusters can be up to 4–5 Å tall.

4.3 Summary

In this chapter, we demonstrated the functionality of a commercial UHV system, including the ability to perform ARPES, UPS, STM, STS, and AFM experiments, as well as temperature and vacuum requirements.

Several additions can further enhance the performance of this system for condensed matter physics research, primarily more functionality for tip and sample preparation. An e-beam stage can be added to the SPM chamber for tip treatment, and a sputter gun to either the transfer or ARPES chambers for cleaning single-crystal metal samples. A cold cleaving stage, cooled by LN_2 or LHe from outside the chamber, can be added to the SPM chamber

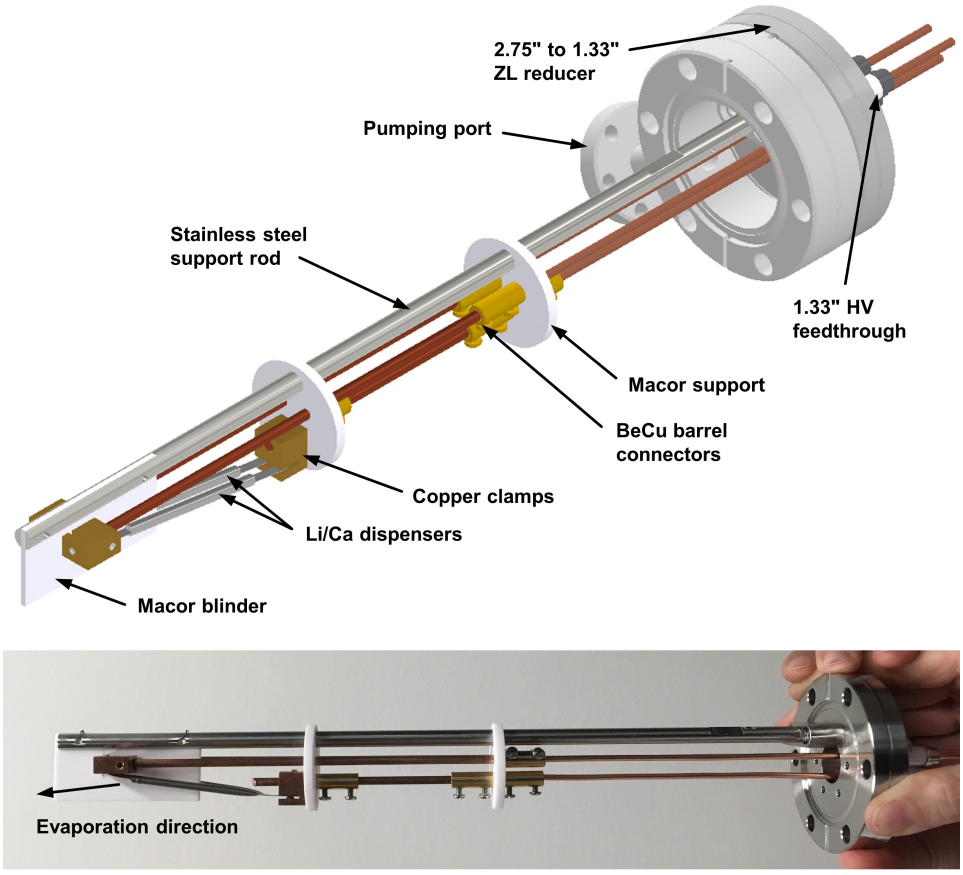

Figure 4.15: Dual source evaporator design. 3D model and photo of the lithium/calcium evaporator. The desired dispenser is selected by connecting to the appropriate pair of leads. A Macor blinder between the ends of the dispensers prevents cross-heating and contamination. The dispensors and leads are supported by a stainless steel road, electrically isolated by Macor plates.

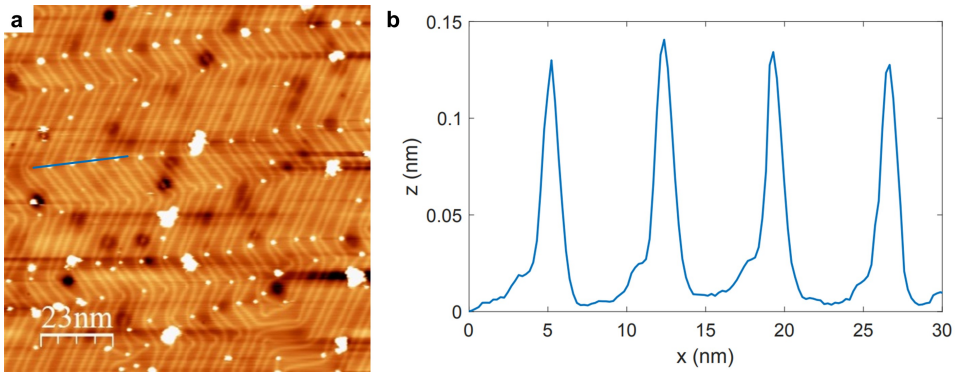

Figure 4.16: Lithium deposition on Au(111). (a) STM topograph (V_{bias} = 1 V, I_t = 20 pA) taken on the Au(111) surface of Au/mica at 1 K after lithium deposition. Lithium preferentially collects at the "elbows" of the Au(111) herringbone reconstruction. **(b)** Height profile taken along the blue line in (a). The smallest bright spots are typically ∼1.3 Å tall; the larger clusters can be up to several angstroms tall.

for materials particularly sensitive to temperature effects.

Chapter 5

Inducing Kekulé bond order in graphene via adatom deposition

5.1 Introduction

A charge density wave (CDW) is a unique quantum phase in which electrons in a low-dimensional system collectively form a standing wave pattern. Such a spatial modulation introduces new periodicities to the host material and can result in bond distortions, folding of the bandstructure, or the opening of a bandgap leading to a metal-to-insulator transition [130, 131, 132]. CDWs have attracted a great deal of interest in the condensed matter community, as they often coexist [133] or compete [134] with other correlated electronic phases such as superconductivity.

The existence of the CDW was first predicted in the 1930s by Peierls, who showed that a 1D metal is unstable at low temperatures and becomes insulating in what is now known as the Peierls transition [131]. The basic 1D chain at high temperature, with unit cell size a and a uniform charge density ρ_e, is shown in Figure 5.1(a). Its bandstructure in the first BZ is shown in Figure 5.1(b). Peierls showed that due to the nesting of the two-point Fermi

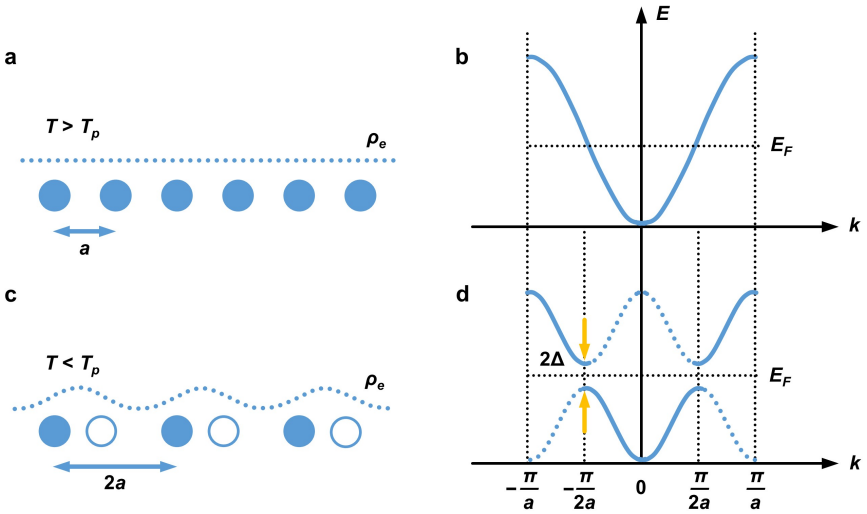

Figure 5.1: The Peierls distortion. **(a)** A 1D chain above the Peierls transition temperature T_p has unit cell size a. The charge density ρ_e is uniform along the chain. **(b)** The bandstructure of the 1D chain in the first BZ. The Fermi level E_F is indicated for half-filling. The Fermi surface is two points connected by a nesting vector of length π/a. **(c)** Below T_p, the chain dimerizes, resulting in a doubling of the unit cell size to $2a$. The charge density becomes modulated in a CDW. **(d)** The BZ is correspondingly halved, and band folding occurs across the new zone boundaries. A gap opening appears at the band crossings, lowering the total electronic energy of the system. Adapted from [132].

surface, such a chain tends to dimerize below some critical temperature T_p, periodically distorting the bonds between atoms and producing two-atom unit cells of size $2a$, resulting in a modulation of the charge density (Figure 5.1(c)). This results in a reduction of the BZ and subsequent band folding across the new zone boundaries, opening up a gap at the band crossings (Figure 5.1(d)).

In graphene, there exists a 2D analog of the Peierls distortion known as the Kekulé distortion. The Kekulé distortion, too, periodically alters the carbon-carbon bonds in graphene [135, 136], resulting in a larger unit cell and band folding. Two examples of Kekulé bond order are shown in Figure 5.2: "Kek-O" in (a) and "Kek-Y" in (b), so named for the shape

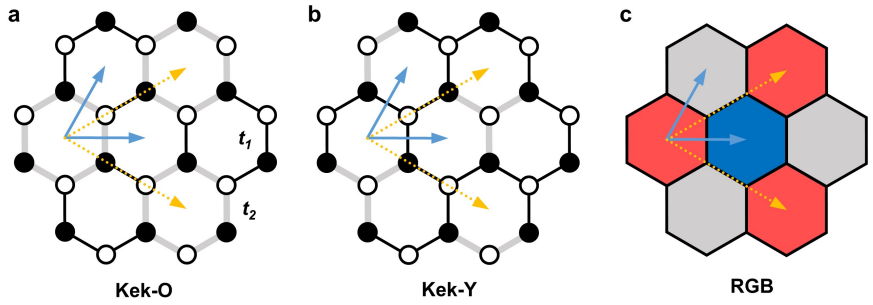

Figure 5.2: Kekulé textures and RGB colour-coding. (a) The "Kek-O texture" of the Kekulé distortion. Thin black lines (hopping t_1) indicate undistorted bonds; thick grey lines (hopping t_2) are distorted. Every third carbon ring is distorted (grey lines), hence its name. The original graphene lattice vectors are shown in blue, and the lattice vectors of the Kekulé superstructure are shown in yellow. **(b)** The "Kek-Y texture" of the Kekulé distortion, named for the Y-shaped pattern of the distorted bonds. While the pattern of bonds is different from Kek-O, the superstructure is the same. **(c)** In both (a) and (b), the graphene flakes can be tiled using three inequivalent hexagons. For simplicity, they can be colour-coded red, grey, and blue (RGB).

of the bonds that are distorted (thick grey lines). The Kek-O texture is particularly interesting as it is predicted to open a band gap at the Dirac point [137], as well as become topologically non-trivial when $t_2 > t_1$ [138]. Meanwhile, the Kek-Y texture preserves the massless character of the Dirac fermions via valley-momentum locking [137].

While the two distortion patterns ("textures") are different, both result in a graphene flake that can be tiled with three different hexagonal plaquettes. A simple way to represent this is to colour-code each hexagon in red, grey, and blue (RGB) as in Figure 5.2(c). The original graphene lattice vectors are shown in blue, while the new, larger $(\sqrt{3} \times \sqrt{3})$ R30° lattice vectors are shown in yellow. This superstructure is particularly key, as the corresponding wavevectors exactly match the nesting wavevectors between the Dirac points at half filling.

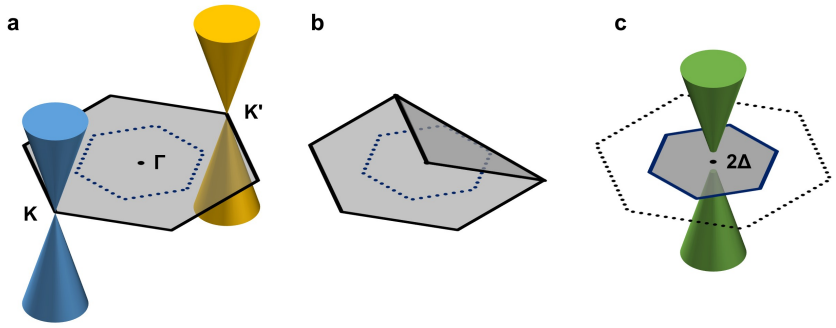

Figure 5.3: Band folding due to the Kekulé distortion. **(a)** Schematic diagram of the graphene bandstructure showing the electronic Dirac cones located at the two different zone corners K and K′ of the graphene BZ (black hexagon). **(b)** The Kekulé superstructure leads to a smaller BZ (blue hexagon) and band folding across the new zone boundaries. **(c)** This produces an additional Dirac cone at Γ, as well as a gap opening at the Dirac point. Adapted from [139].

Just as with the Peierls distortion, this larger unit cell corresponds to a reduced BZ, band folding across the new zone boundaries, and a gap opening at the Dirac point (Figure 5.3). A more theoretical discussion of this bandstructure can be found in Section 2.4.

Unlike the case of the 1D chain, however, the graphene lattice does not spontaneously exhibit the Kekulé distortion due to the rigidity of the lattice [51]. Instead, theorists have suggested that one way to induce the formation of such a phase is through the use of a small number of adatoms [139, 140, 141]. These adatoms act as scattering centres, generating Friedel oscillations with wavelength corresponding to the Fermi wavevector k_F. Due to the unique bandstructure of graphene, this wavelength is commensurate with the $(\sqrt{3} \times \sqrt{3})$ R30° superstructure of the Kekulé distortion. Through these long-ranging oscillations, adatoms can interact with each other across many graphene unit cells, and if they are sufficiently mobile, they can minimize the system energy by choosing sites such that their Friedel oscillations are all in phase. In the RGB scheme, this corresponds to all adatoms sitting on sites of a single colour in what is called hidden Kekulé order (HKO): since

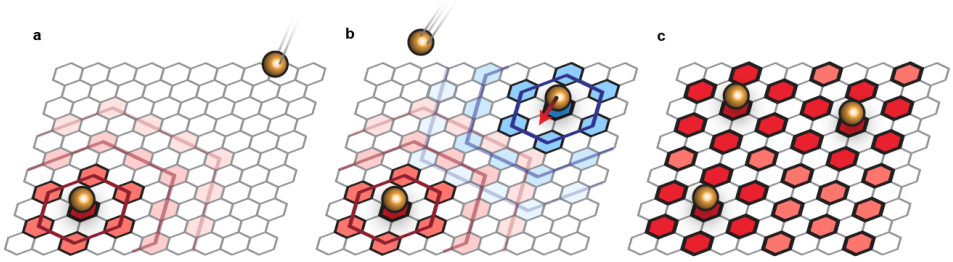

Figure 5.4: Formation of Kekulé ordering during adatom deposition. (a) A single adatom on a graphene flake produces Friedel oscillations with periodicity $a = \sqrt{3}a_0$, resulting in symmetry breaking between three previously equivalent hollow sites (indicated in red). Bond distortions appear near the adatom. **(b)** A second adatom arrives and lands on an out-of-phase site, producing its own preferred sites nearby (indicated in blue). It "feels" the potential from the first adatom and shifts to a "red" site. **(c)** As more adatoms occupy in-phase sites, the entire flake falls into the $(\sqrt{3} \times \sqrt{3})$ R30° Kekulé ordered superstructure, and every third bond is distorted. Adapted from [142].

the adatoms may be far apart from each other, they would appear to sit randomly until the RGB colour-coding is applied and the ordering emerges. In this way, the constructively interfering Friedel oscillations produce a CDW with periodicity corresponding to the $(\sqrt{3} \times \sqrt{3})$ R30° superstructure [51, 139, 140, 141].

Experimentally, one way to realize such an adatom-decorated graphene flake is by slow evaporation onto a graphene sample held at low temperature (5–20 K). The deposition process is shown schematically in Figure 5.4. First, a single adatom on the flake produces Friedel oscillations nearby, resulting in symmetry breaking between the three previously equivalent "colours" (Figure 5.4(a)). Subsequent incoming atoms "feel" these Friedel oscillations and are able to shift to in-phase sites as they thermalize with the graphene flake (Figure 5.4(b)). If the deposition is sufficiently slow, giving present adatoms time to order before new atoms arrive, all adatoms will sit on sites of the same colour, producing the $(\sqrt{3} \times \sqrt{3})$ R30° superstructure everywhere (Figure 5.4(c)). Note that in Figure 5.4, atoms that prefer the graphene

"hollow" sites (in the centre of the hexagons) are shown: this results in the Kek-O texture, but other species of adatoms can be strategically selected to e.g. sit on the graphene "top" sites (directly above a carbon atom) for the Kek-Y texture.

Such a Kekulé phase in graphene has been previously observed with STM, using not adatoms as scatterers but vacancies in the Cu(111) substrate on which the graphene was grown [51]. Such vacancies prefer to sit directly below carbon atoms in the graphene lattice, resulting in the Kek-Y texture. However, the Kek-Y texture is not predicted to open a gap at the Dirac point [137], and without momentum-resolved methods, this study was unable to observe any folding of the bandstructure.

In this chapter, we present a method for inducing the Kekulé distortion in epitaxial graphene films by depositing an extremely dilute concentration of lithium adatoms. Using ARPES, we probe the electronic bandstructure of this Kekulé phase and directly visualize the folded Dirac cone at the BZ center, as well as observe the opening of an energy gap of $2\Delta_{kek} = (126 \pm 5)$ meV at the Dirac point, the two signatures of the Kekulé phase in graphene. The Kekulé superstructure is confirmed using LEED experiments. We observe that this Kekulé phase is reproducible in other graphene systems independent of doping level and shape of the Fermi surface, and finally, we study the deposition process using a Monte Carlo toy model for the real space behaviour of the adatoms.

5.2 Methods

Monolayer graphene samples were grown epitaxially on hydrogen-etched silicon carbide (SiC(0001)) substrates under argon atmosphere [29, 120]. Prior to ARPES measurements, the sample surface was cleaned by annealing at 600°C in UHV for several hours and allowed to cool. Lithium was deposited *in situ* between 5–20 K using a commercial SAES alkali metal source over 3–30 minutes, with a shutter blocking the direct line of sight between the source and the sample.

ARPES and LEED experiments were performed at the University of British Columbia in an ultra-high vacuum chamber equipped with a SPECS Phoibos 150 Hemispherical Analyzer, a SPECS UVS300 Monochromatized Gas Discharge Lamp, and a SPECS ErLEED 1000A. The sample temperature was held between 5 and 30 K for all experiments, and the chamber pressure was better than 10^{-10} torr. For the ARPES experiments, *s*- and *p*- polarized 21.2 eV photons were used, and the energy and momentum resolution were better than 20 meV and 0.01 Å^{-1}, respectively.

For a full description of the samples and system used in this chapter, see Chapter 3.

5.3 Results & Discussion

5.3.1 Superstructure and band folding

On the pristine sample, the Dirac cone at K is clearly visible (Figure 5.5(a)). Due to charge-transfer doping from the substrate, the Dirac point is shifted to ∼450 meV below the Fermi level E_F [41, 120, 143]. The observed intensity asymmetry of the two branches of the Dirac cone is due to ARPES matrix element effects related to the electron momentum, photon energy, and photon polarization (detailed in Section 3.1) [144]. Meanwhile, at Γ (Figure 5.5(d)), no bands are visible, consistent with the bandstructure calculated in Section 2.1.

Figure 5.5(b) and (d) show the same two spectra near K and Γ, respectively, after lithium decoration,. At K, some broadening of the bands occurs due to increased disorder in the system, but no other qualitative changes are observed (we will discuss quantitative changes momentarily).

More striking is the appearance of new electronic energy bands centred at Γ, as can be directly observed in Fermi surface maps (Figure 5.5(c)). These new bands appear as a replica Dirac cone, corresponding the superposition of the folded Dirac cones at K and K′ due to the emergence of a $(\sqrt{3} \times \sqrt{3})$ R30° superstructure. This superstructure may be caused by the additional scattering vectors induced by the lithium-related modulation. Supporting

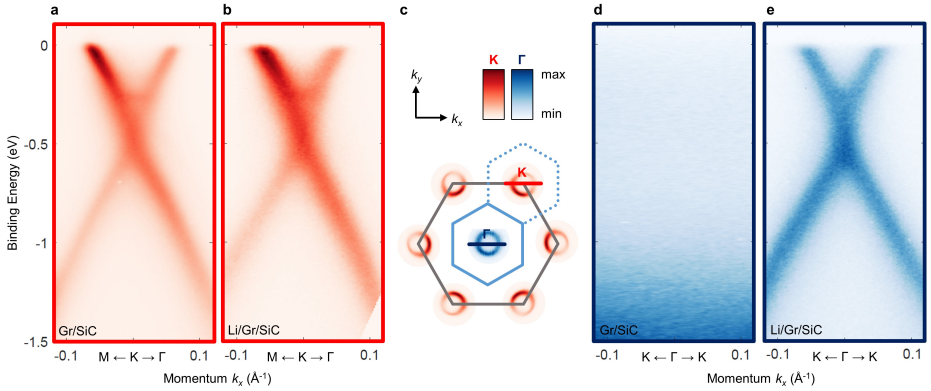

Figure 5.5: Band folding observed by ARPES. (a) ARPES spectra through the Dirac cone at K (cut indicated by red line in (c)) in pristine Gr/SiC. The Dirac cone has some initial doping due to charge transfer from the substrate, and one branch appears brighter due to matrix element effects. **(b)** The same spectra as (a) after dilute lithium deposition. The bands are slightly broader due to increased disorder in the system, but no charge transfer doping from the lithium is detectable. **(c)** Schematic of the BZ of pristine graphene (grey) and the $(\sqrt{3} \times \sqrt{3})$ R30° superstructure (blue) superimposed on the Fermi surfaces after lithium decoration (not to scale; data from one K point is symmetrized for all other K points). Locations of the ARPES cuts in (a), (b), (d), and (e) are indicated by the red and blue lines. **(d)** Spectra at Γ (cut indicated by blue line in (c)) in pristine Gr/SiC. No bands are present. **(e)** The same spectra as (d) after dilute lithium deposition. The folded Dirac cone is clearly resolved, and both branches are equally bright due to mixing of the K and K′ cones. A gap is opened at the Dirac point. Adapted from [142].

this interpretation for the origin of the new feature, the Dirac cone centred at Γ presents a momentum-symmetric intensity reflecting its mixed character due to contributions from Dirac cones at opposite ends of the graphene BZ (Figure 5.5(c), grey hexagon). In addition, these new bands are extremely sharp: the linewidth near the Fermi level is very similar between K and Γ after lithium decoration, and only slightly broader than at K on the pristine sample (Figure 5.6), indicating ordering on the length scale of the ARPES spot size (approximately 1 mm).

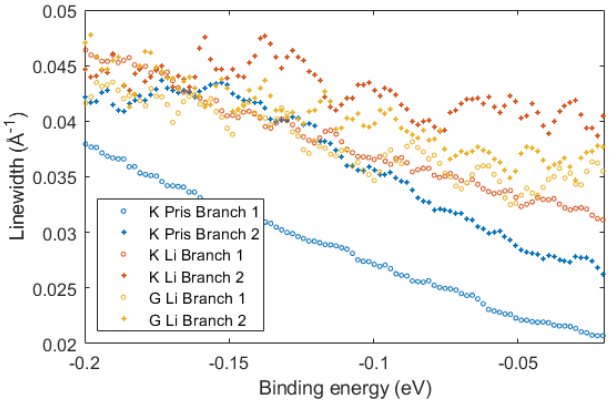

Figure 5.6: ARPES linewidth comparison. The linewidth of both branches of the Dirac cone near the Fermi level is plotted for the cone at K on pristine Gr/SiC (blue), as well as the cones at K (orange) and Γ (yellow) after lithium decoration. After lithium decoration, the linewidths near K and Γ are very similar, and only slightly broader than near K on the pristine sample.

We also eliminate the possibility of a larger superstructure by studying a continuous ARPES cut between Γ and K along $k_y = 0$ (Figure 5.7). Three additional Dirac cones with low intensity are observed here due to Umklapp scattering: SiC 1×1 (blue), 1×1 plus 6×6 (green), and 6×6 (yellow) [145, 146]. Note that in *s*-polarization (shown here), only one branch of each cone is visible due to matrix element effects; the other branch can be observed in *p*-polarization. These cones are already present on the pristine sample, however, and indicate a highly ordered substrate [145]. No new features are observed after the lithium decoration.

The same superstructure is further confirmed by the appearance of new peaks in LEED measurements after lithium decoration (Figure 5.8). Figure 5.8(a) shows the LEED pattern observed on the pristine Gr/SiC, measured using 66 eV electrons. Both the graphene and SiC periodicities are observed, and the calculated peaks are overlaid on the pattern (graphene: red, SiC: green). Weaker "satellite" peaks around each of these peaks (yellow) are also visible, corresponding to the periodicity of the graphene-

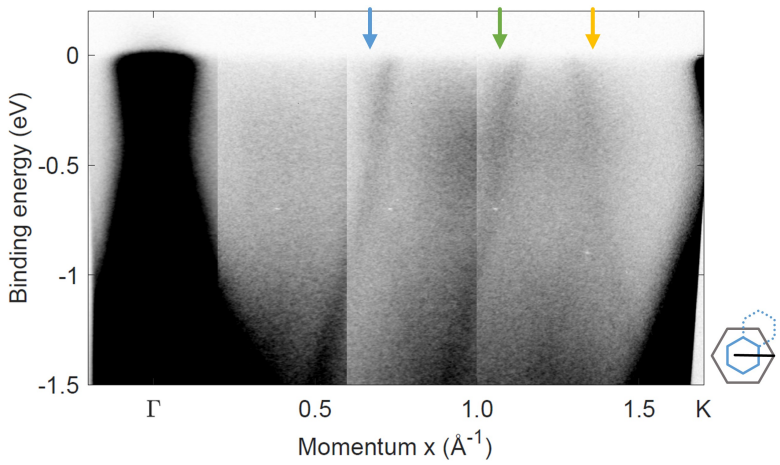

Figure 5.7: Full ΓK cut in ARPES. Multiple spectra are stitched together to cover the full k distance from Γ to K along $k_y = 0$ after lithium decoration, collected using s-polarized light. The cut is indicated by the schematic in the bottom right corner. The colour scale is set to show the Umklapp scattered Dirac cones (saturating the cones at Γ and K): the arrows indicate the SiC 1×1 (blue), 1×1 plus 6×6 (green), and 6×6 (yellow) replicas. These are present before the lithium decoration and indicate excellent substrate quality [145]. Only one branch of each cone is visible due to matrix element effects.

SiC moiré pattern. Figure 5.8(b) shows the LEED pattern observed after lithium decoration, when the reconstructed cone appears at Γ in ARPES measurements. The appearance of additional peaks corresponding to the $(\sqrt{3} \times \sqrt{3})R30°$ superstructure are observed; the calculated peaks for the superstructure are overlaid in blue.

Figure 5.8(c) shows a direct comparison of line cuts taken from (a) (black dotted line) and (b) (red dotted line). The peaks are labelled with arrows using the same colour scheme. There is very little change in the graphene and moiré peaks before and after the lithium decoration; however, the appearance of the new peaks is clear. The line profile after lithium decoration is further analyzed in Figure 5.8(d) by fitting to a sum of seven Lorentzians (two each for the graphene, moiré, and superstructure peaks, and one additional for the background). Four of these fitted Lorentzians are shown individually: red

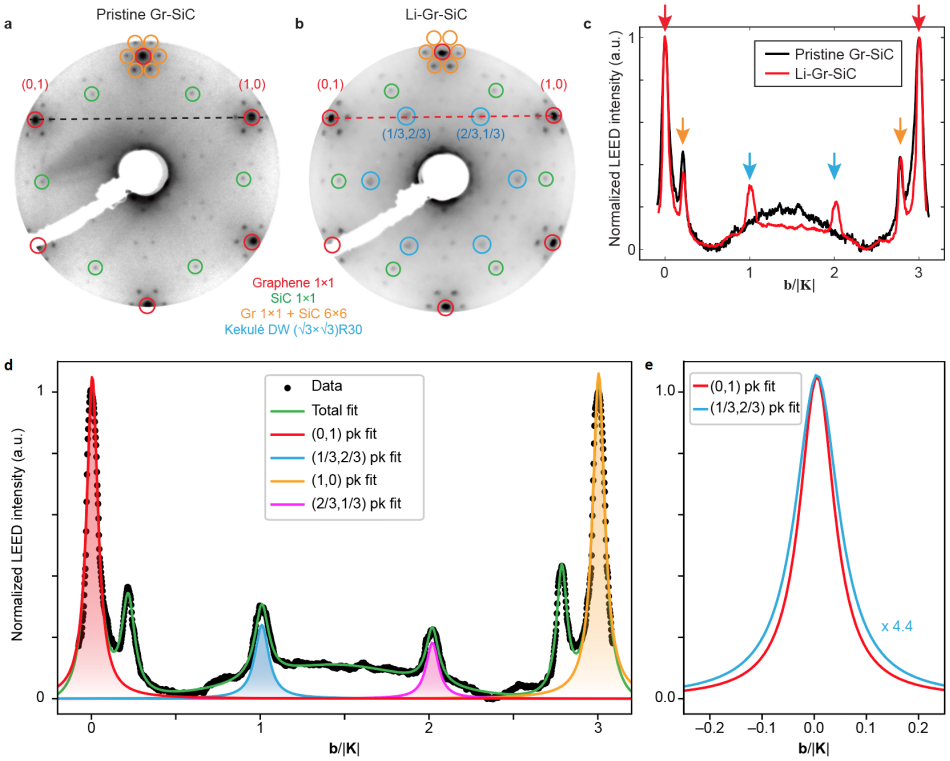

Figure 5.8: Superstructure appearance observed by LEED. (a) LEED pattern measured at 66 eV on the pristine sample. Calculated peaks are overlaid for graphene (red), SiC (green), and the graphene/SiC moiré pattern (yellow). **(b)** The same LEED pattern after lithium deposition. New spots corresponding to the $(\sqrt{3} \times \sqrt{3})$ R30° superstructure (blue) are clearly visible. **(c)** Line profiles taken at the black and red dotted lines in (a) and (b). Peaks are indicated by arrows using the same colour scheme. The width of the graphene and graphene/SiC peaks are comparable before and after lithium decoration. **(d)** Fitting the line profile from (b). The green line is a sum of seven Lorentzians, of which four are individually shown (red, blue, pink, and yellow). **(e)** Direct comparison of the normalized $(0, 1)$ (graphene) and $(1/3, 2/3)$ (superstructure) peaks from (b). The superstructure peak is almost as sharp as the graphene peak, indicating a highly ordered system. Reproduced from [142].

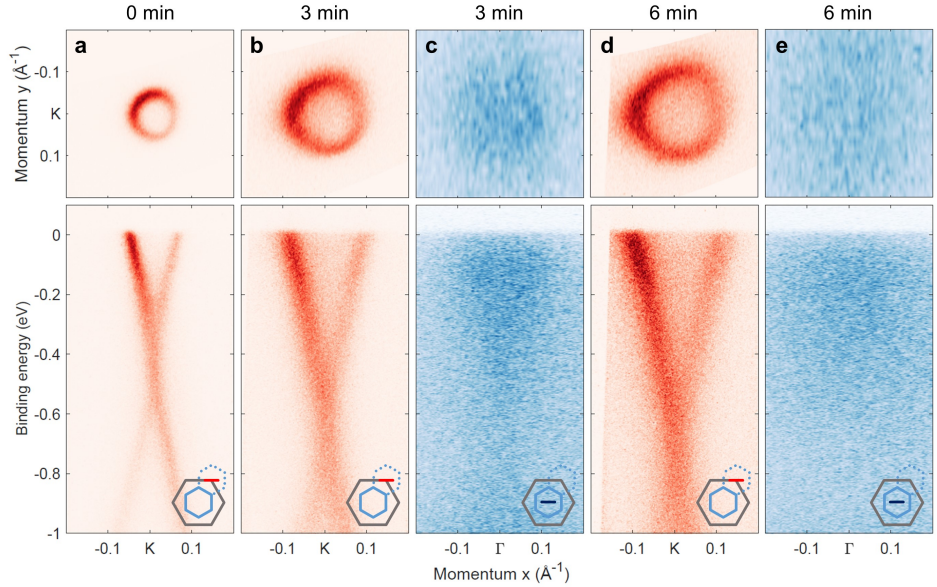

Figure 5.9: Effects of high lithium coverage. **(a)** Fermi surface (top) and cut (bottom) near K on pristine Gr/SiC. The position of the cut with respect to the graphene BZ is shown in the inset. This is the same spectra as Figure 5.5(a), shown here for comparison. **(b)** The same Fermi surface and cut as in (a) after 3 minutes of "normal" lithium deposition, with a direct line of sight from the evaporator to the sample. The Dirac point is shifted away from E_F by ~ 200 meV compared to (a), and the size of the Fermi surface grows correspondingly. **(c)** Fermi surface and cut at Γ after 3 minutes of normal lithium deposition. Some intensity corresponding to a folded Dirac cone appears, but the sharp bands in Figure 5.5(d) are not observed. **(d)** The same Fermi surface and cut as in (a) after 6 minutes of normal lithium deposition. The Dirac point is further shifted by ~ 150 meV compared to (b). **(e)** The same Fermi surface and cut as in (c) after 6 minutes of normal lithium deposition. Some intensity is detected, but no sharp bands are observed. Adapted from [142].

and yellow for the graphene peaks, blue and pink for the superstructure peaks. The red and blue peaks are normalized and compared directly in Figure 5.8(e): the superstructure peak is only slightly broader than the graphene peak (by approximately 25%), indicating coherence in the superstructure on a global scale.

We stress here that these results cannot be explained by the presence of a dense coverage of $(\sqrt{3} \times \sqrt{3})$ R30° ordered adatoms. Firstly, there are no additional electronic bands due to a lithium lattice in our measurements at Γ [147]. Secondly, such a high surface coverage (1/3 monolayer) by alkali atoms would strongly electron-dope our graphene film and thus significantly shift the Dirac point, as has been observed in photoemission experiments on lithium- [53, 148] and calcium-intercalated graphitic systems [149, 150]. The same effect can be observed in our system after depositing lithium with a direct line of sight to the Gr/SiC sample to obtain a higher concentration (Figure 5.9). Here, a clear shift of the Dirac point energy away from E_F is observed after 3 minutes of direct lithium deposition (Figure 5.9(b)), but a sharp reconstruction does not appear at Γ (Figure 5.9(c)). By blocking the direct line of sight between the lithium evaporator and the sample, no detectable shift of the Dirac point occurs even after 30 minutes of deposition, suggesting extremely dilute coverage.

Since we are unable to measure any shifting of the Dirac point after lithium decoration, it is difficult to determine the amount of lithium present. However, we may be able to estimate an upper bound. The resolution of the ARPES system is better than 20 meV; thus, a downward shift of the Dirac point by 20 meV should certainly be detectable. This would correspond to an increase in charge carrier density of approximately 6×10^{11} cm^{-2}. Previous studies of the Li/Gr/SiC system suggest that each lithium adatom donates at least 0.14 electrons to the graphene [53]. Thus, the lithium concentration should be below 4×10^{12} cm^{-2} (about 0.2% of a monolayer, where every graphene hollow cite is occupied). This corresponds to an average distance of ∼5 nm between lithium atoms, comparable to observations in a defect-induced Kekulé distortion [51].

Instead of a dense layer of ordered adatoms, these results are instead well-explained by the onset of a globally phase-coherent Kekulé density wave phase via the HKO mechanism [139]. This global phase-coherence is evidenced by the particular sharpness of the replica Dirac cone at Γ (Figure 5.5(d)) over the long length scale of our ultraviolet light source spot size (∼1 mm). Such long-ranged phase coherence originates from a majority

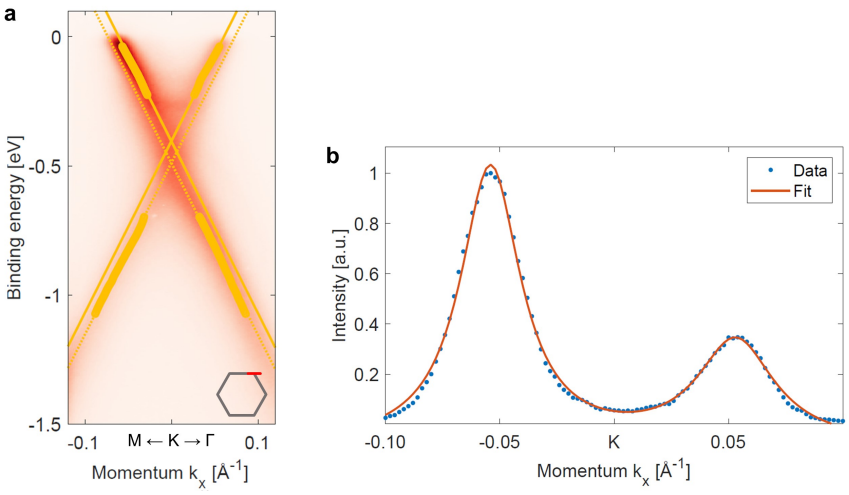

Figure 5.10: Dirac point gap on pristine graphene. (a) The same spectra as Figure 5.5(a) overlaid with the band positions obtained through fitting MDCs (thick yellow lines). Linear dispersions are fitted above (solid yellow lines) and below (dotted yellow lines) the Dirac point. Intersections above and below the Dirac point do not coincide, indicating a gap opening. **(b)** An example of a single MDC from (a), taken just below the Fermi level at $E_B = -40$ meV. It is fitted by two Lorentzians and a constant background. Note that the fitted lineshapes are slightly narrower than the data: this is due to experimental resolution and can be compensated by convolving the fit with a Gaussian, but it does not affect the peak position and is neglected here for computational speed. Adapted from [142].

of Li adatoms occupying a single coloured Kekulé site (Figure 5.4(d)). This is further supported by the appearance of new and sharp diffraction peaks in LEED (Figure 5.8), which point to the electrons forming a well-defined and long-ranged $(\sqrt{3} \times \sqrt{3})$ R30° lattice, suggesting the presence of a structural lattice distortion in graphene.

5.3.2 Gap opening at the Dirac point

To analyze the ARPES data in greater detail, momentum distribution curves (MDCs) at each binding energy are fitted with two Lorentzians plus a constant offset (Figure 5.10(b)). The peak positions of the Lorentzians indicate the

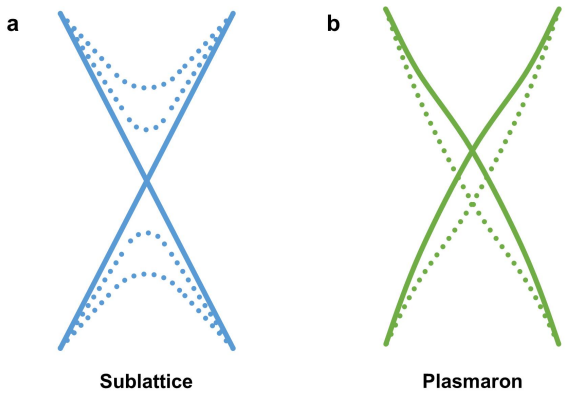

Figure 5.11: Explanations for the "gap" in pristine Gr/SiC. (a) A range of substrate interaction strengths results in varying sublattice gap sizes (dotted lines) across the sample, which are spatially averaged by ARPES experiments. Areas where the gap is small or zero (solid lines) contribute to intensity inside the "gap." **(b)** Coupling between charge carriers and plasmons lead to new "plasmaron" quasiparticles, resulting in a splitting of the pure charge bands (solid lines) and pure plasmaron bands (dotted lines). The Dirac point is resolved into two separate crossings.

electronic dispersion of the bands. Figure 5.10(a) once again shows the spectra near K on the pristine sample (same as Figure 5.5(a)), with the peak positions overlaid (thick yellow lines). The dispersions are well described by linear fits (thin yellow lines) both above (solid lines) and below (dotted lines) the Dirac point. For massless Dirac fermions, the extrapolated fits from the two energy bands should coincide at the Dirac point. However, such a crossing is not observed.

Two explanations for this mismatched crossing in Gr/SiC are commonly presented in the literature. In the first, a gap is opened at the Dirac point by sublattice symmetry breaking (Section 2.3) due to interactions with the underlying SiC substrate. The interaction strength varies across the sample, resulting in a range of gap sizes and contributing to intensity inside the gap (Figure 5.11(a)) [35, 41]. The average size of such a sublattice gap can be

determined by fitting the bands observed in ARPES with a hyperbola.

In the second explanation, charge carriers in the graphene interact with plasmons (density oscillations in the electron gas), leading to the creation of a new "plasmaron" quasiparticle. This results in the separation of the Dirac cone into charge bands (Figure 5.11(b), solid lines) and plasmaron bands (Figure 5.11(b), dotted lines), and the Dirac point splits into two individual crossings [151, 152]. Such a splitting can be determined by fitting the top and bottom halves of the Dirac cone using linear bands as shown in Figure 5.10(a).

Without ruling out either model, here we will primarily use the sublattice model of the "gap" for simplicity. However, we note that the key result—a gap opening at the Dirac point—is reproducible using both the sublattice and plasmaron models.

It is somewhat difficult to extract an accurate estimate for the size of this gap from a single cut in momentum, since the cut must pass through the Dirac point exactly or else the gap will appear artificially larger (Figure 5.12(a) and (c)). To carefully determine a value for this gap, we collect a volume of photoemission data near the Dirac point and take many cuts at different values of k_y. For each cut, the dispersions are extracted in a region near the Dirac point by fitting MDCs as before (Figure 5.12(a–c), thick yellow lines). Then, all four branches are fit to a hyperbola (thin yellow lines). The apparent gap size 2Δ for a particular k_y cut is taken to be the distance between the top and bottom vertices. Finally, the apparent gap size is plotted as a function of k_y and fitted to half a hyperbola (Figure 5.12(d) and (e)), where the minimum is taken to be the actual gap size.

Using this procedure, the pre-existing gap size at K on pristine Gr/SiC is determined to be $2\Delta_{ab} = (292 \pm 4)$ meV (Figure 5.12(d)). This is comparable to the values given in the literature, e.g. ~ 260 meV by Zhou *et al.* [41] and ~ 250 meV by Nigge *et al.* [35] (using the same data set as presented here, with a slightly different fitting procedure).

Similarly, the gap size at K after lithium decoration is observed to increase to $2\Delta_{tot}^{\mathrm{K}} = (354 \pm 2)$ meV (Figure 5.12(d)). The new cone appearing at Γ, by comparison, has a slightly larger gap size of $2\Delta_{tot}^{\Gamma} = (377 \pm 4)$

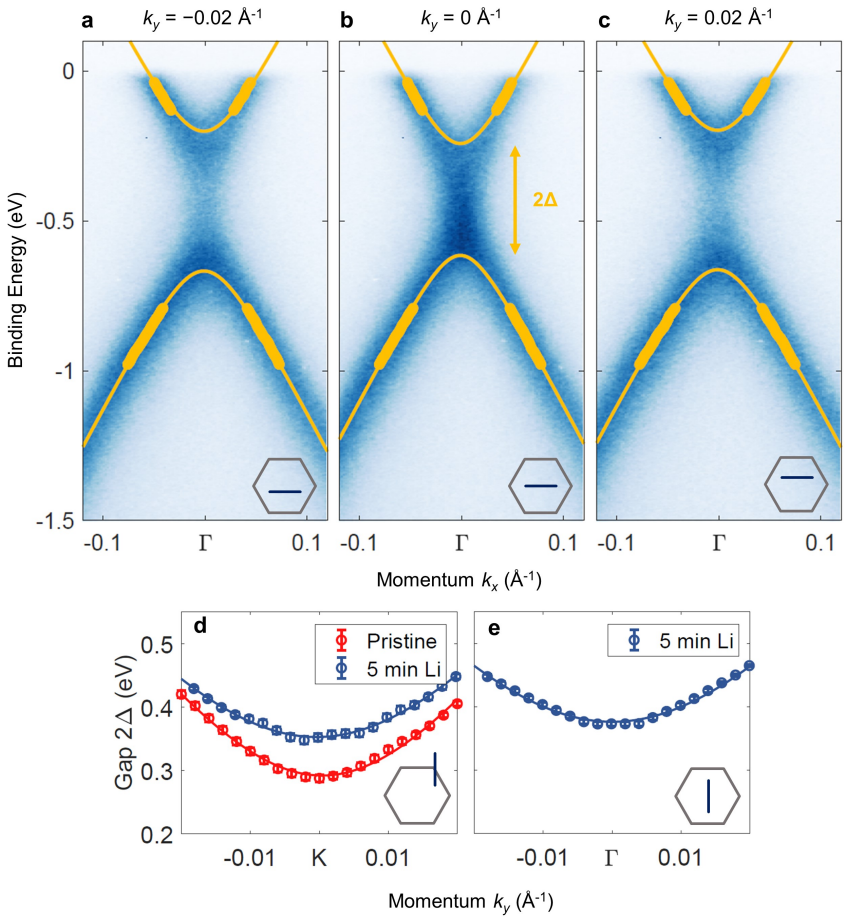

Figure 5.12: Gap-fitting procedure. (a–c) Fitting the Dirac point gap for ARPES cuts taken through the Dirac cone at Γ at different positions in k_y. The inset shows the position of the cut with respect to the graphene BZ (exaggerated for clarity). When the cut does not pass through the Dirac point, the gap appears artificially larger ((a) and (c)). **(d)** Apparent gap size as a function of distance to the Dirac point at K, before (red) and after (blue) lithium decoration. The "true" gap size is indicated by the minimum, when the cut passes directly through the Dirac point. After lithium decoration, a gap opening from $2\Delta = (292 \pm 4)$ meV to $2\Delta = (354 \pm 2)$ meV is observed. **(e)** Apparent gap size as a function of distance to the Dirac point of the new cone at Γ formed after lithium decoration. A gap size of $2\Delta = (377 \pm 2)$ meV is observed. Adapted from [142].

meV (Figure 5.12(e)). A possible explanation for this discrepancy is the contribution from areas of the sample without lithium, which exhibit a smaller gap at K but no intensity at all at Γ.

Here we also note that using the plasmaron model instead of the sublattice model—that is, fitting four linear bands and extracting the energy difference between the top and bottom crossings—a similar gap opening is observed, although the numbers are smaller due to the shape of the fitted function. In this case, we obtain $2\Delta_{ab} = (98 \pm 3)$ meV at K on pristine Gr/SiC, which increases to $2\Delta_{tot}^{\mathrm{K}} = (150 \pm 2)$ meV after lithium decoration. At Γ after lithium decoration, we obtain $2\Delta_{tot}^{\Gamma} = (160 \pm 4)$ meV.

As with the superstructure and band folding described in Section 5.3.1, this gap opening can be explained by the onset of a Kekulé phase, as shown mathematically in Section 2.4. In particular, the gap opening due to the Kekulé phase Δ_{kek} can be distinguished from the gap opening due to sublattice symmetry breaking Δ_{ab} by the appearance of the new Dirac cone at Γ: while Δ_{ab} opens a gap through on-site terms in the Hamiltonian, Δ_{kek} couples the K and K′ valleys, resulting in the band folding and extra cone at Γ. The two terms add in quadrature, $\Delta_{tot}^2 = \Delta_{ab}^2 + \Delta_{kek}^2$ (Section 2.4). Thus, using $2\Delta_{tot} = (377 \pm 4)$ meV, we can estimate the gap opening due to the Kekulé phase, $2\Delta_{kek} = (238 \pm 3)$ meV.

Finally, using these values for Δ_{ab} and Δ_{kek}, we can directly compare the bandstructure observed in ARPES with the tight-binding models from Chapter 2. The tight-binding calculations in Figure 5.13 (black lines) use hopping parameters $t = t_1 = 3$ eV and $t_2 = t_1 + \Delta_{kek}$, and from the fits, $2\Delta_{ab} = 292$ meV, $2\Delta_{kek} = 200$ meV at K and 238 meV at Γ. Both the Fermi surfaces (top row) and momentum cuts (bottom row) show good agreement with the spectra.

5.3.3 Transition temperature of the Kekulé phase

The size of the gap Δ_{kek} is related to the adatom density ρ and the transition temperature of the Kekulé phase T_{kek} via

$$k_B T_{kek} \approx 4\lambda^2 \rho^{3/2} h v_F a^2 \tag{5.1}$$

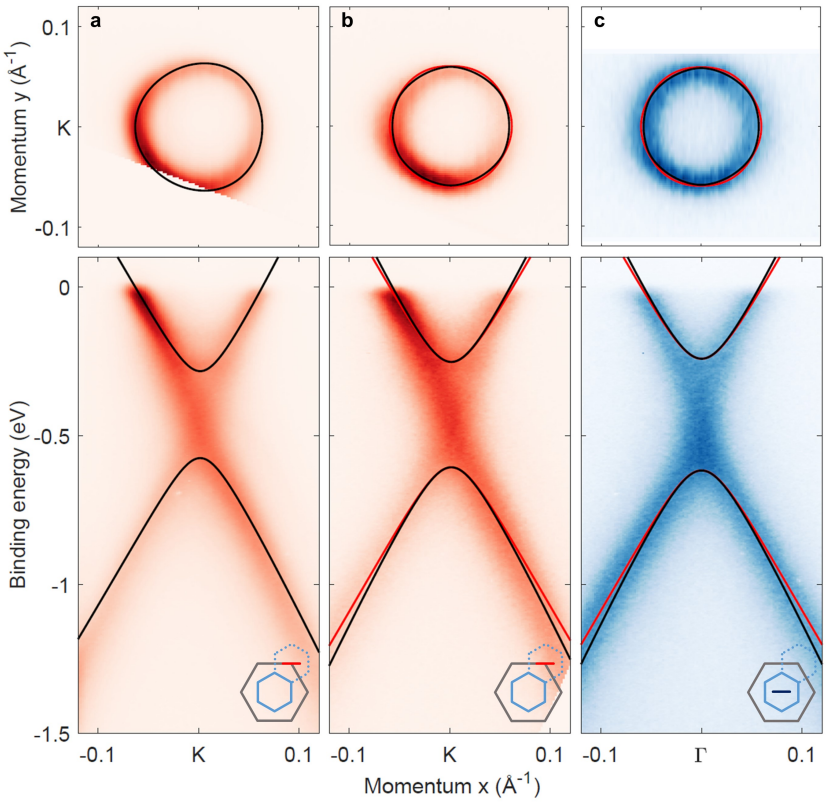

Figure 5.13: Tight binding comparison. (a) Fermi surface (top) and a momentum cut (bottom) near K on the pristine Gr/SiC (same spectra as Figure 5.5(a)). The tight-binding model from Section 2.3, using $t = 3$ eV and $2\Delta_{ab} = 292$ meV, is overlaid in black lines. **(b)** Spectra near K on Gr/SiC after lithium decoration (same spectra as Figure 5.5(b)). This tight-binding model is from Section 2.4, with $2\Delta_{kek} = 200$ meV. Two bands are present due to folding: they are overlaid in black and red lines. **(c)** Spectra near Γ after lithium decoration (same spectra as Figure 5.5(e)). This tight-binding model is from Section 2.4, with $2\Delta_{kek} = 238$ meV.

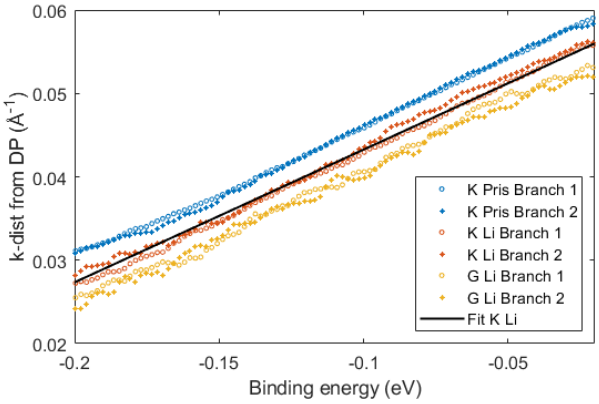

Figure 5.14: Fermi velocity fit. To obtain v_F, the position of both branches of the Dirac cone are fitted between 20 to 200 meV below E_F, then offset by the Dirac point position in k_x. The two branches are overlaid by inverting the sign of one branch. This is shown for the cone at K before (blue) and after (orange) lithium decoration, as well as for the cone at Γ (yellow) after lithium decoration. While the slope of the linear dispersions (v_F) are in close agreement between the cones, the offset is in agreement with the gap opening we observed in Figure 5.12. An example linear fit to one branch is shown (black). By fitting the slope of all six branches, we obtain $v_F = (9.6 \pm 0.2) \times 10^5$ m/s.

and

$$\Delta_{kek} = \lambda \rho h v_F a. \tag{5.2}$$

Here v_F is the Fermi velocity, $a = 2.46$ Å is the graphene lattice constant, and $\lambda \lesssim 1$ is a dimensionless coupling constant [139].

We can estimate v_F by fitting the band dispersion near E_F. In Figure 5.14, we show the positions of both branches of the Dirac cone at K on pristine Gr/SiC (blue symbols) between 20 and 200 meV below E_F, which are then offset by the position of the Dirac point (estimated using the intersection of the two branches). The slope of the two branches are in good agreement, and using these dispersions, we can estimate v_F to be approximately 9.6×10^5 m/s. We can repeat this process for the cones at K and Γ after lithium decoration (Figure 5.14, orange and yellow symbols), and while there is a small overall offset due to the gap opening, the slopes are in good agreement.

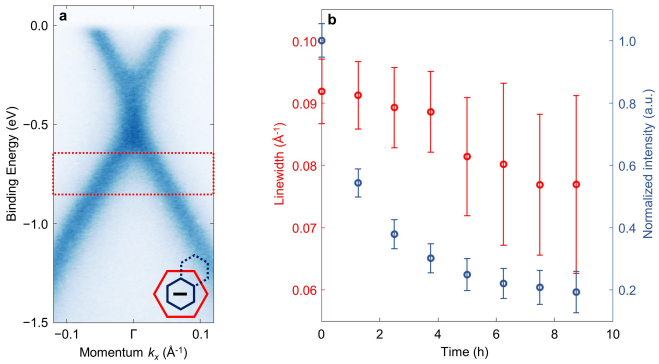

Figure 5.15: Destroying the Kekulé ordering. (a) A sample ARPES cut through the folded cone at Γ. The intensity of the band is an indication for the fraction of the sample in the Kekulé phase; the linewidth is an indication for the coherence across these areas. The region indicated by the red box is fitted to produce the data in (b). **(b)** Linewidth and amplitude of the bands at Γ while the sample is held near the transition temperature. Both decrease as a function of time, suggesting that the lithium is less stable in areas with less order. Adapted from [142].

From all six branches, we estimate $v_F = (9.6 \pm 0.2) \times 10^5$ m/s.

Using this value for v_F and Equation 5.1, we can obtain a lower bound for the adatom density $\rho \gtrsim 1 \times 10^{13}$ cm^{-2}. This is comparable to the upper bound we obtained in Section 5.3.1, $\rho \lesssim 4 \times 10^{12}$ cm^{-2}. This suggests that the true adatom density may be in this regime. Using $\rho \gtrsim 1 \times 10^{13}$ cm^{-2} and Equation 5.1, we can estimate the transition temperature T_{kek} to be above 360 K. STM experiments on a similar system with a different Kekulé "texture" also suggests a high transition temperature of well above 300 K [51].

However, in both ARPES and LEED, we observe that all signatures of the superstructure are only stable up to ∼30 K, at which point they vanish and do not recover upon subsequent cooling. This suggests that this temperature is limited by lithium stability rather than the Kekulé phase. We can study this transition by continuously observing the sample while it is held near this temperature. At 30 K, it takes several hours for the folded Dirac cone at Γ to vanish completely. During this time, we continuously collect ARPES data

near Γ (Figure 5.15) and monitor the amplitude and linewidth of the bands (Figure 5.15, region indicated in red). Remarkably, as the ARPES intensity decays at Γ, the linewidth of the bands also decreases, indicating increased order in the system. This suggests that the less ordered areas are less stable, consistent with the theory of in-phase density waves adding constructively to create deeper potentials at the in-phase sites.

5.3.4 Reproducibility in other graphene systems

A second method to disrupt the Kekulé order as suggested by theory is to alter the charge carrier density of the system [139]. A finite carrier density ρ_e produces an additional modulation of the Friedel oscillations with periodicity on the order of $\rho_e^{-1/2}$ [153]. For large $\rho_e \gtrsim \rho$, then, this modulation effectively scrambles the sign of the adatom interaction, and ordering would no longer occur [139].

To elucidate the effect of different doping levels (and thus also the shape of the graphene Fermi surface) on this lithium-induced order, we further study two additional epitaxial monolayer graphene samples. Instead of the carbon buffer layer, hydrogen (H) and gadolinium (Gd) atoms are intercalated below the graphene to decouple it from the substrate (for details, see Section 3.5). The hydrogen-intercalated sample (Gr/H/SiC) is slightly p-doped, with the Dirac point shifted to ∼100 meV above E_F [52], while the Gd-intercalated sample (Gr/Gd/SiC) is n-doped, with the Dirac point shifted to ∼1.6 eV below E_F [60].

ARPES cuts taken through the Dirac cone on these two samples are shown in Figure 5.16(a) (Gr/H/SiC) and (c) (Gr/Gd/SiC). As before, the location of the cut with respect to the graphene BZ (grey) is indicated by the inset. The Gr/H/SiC spectra (Figure 5.16(a)) is very similar to the Gr/SiC with a shift of the Dirac point. The Gr/Gd/SiC spectra (Figure 5.16(c)), however, has some notable features. In particular, with the Dirac point shifted to −1.6 eV, the asymmetry between the dispersions in the KM (towards the left) and KΓ (towards the right) directions become significant. A comparison of the Fermi surfaces taken on the Gr/SiC and Gr/Gd/SiC

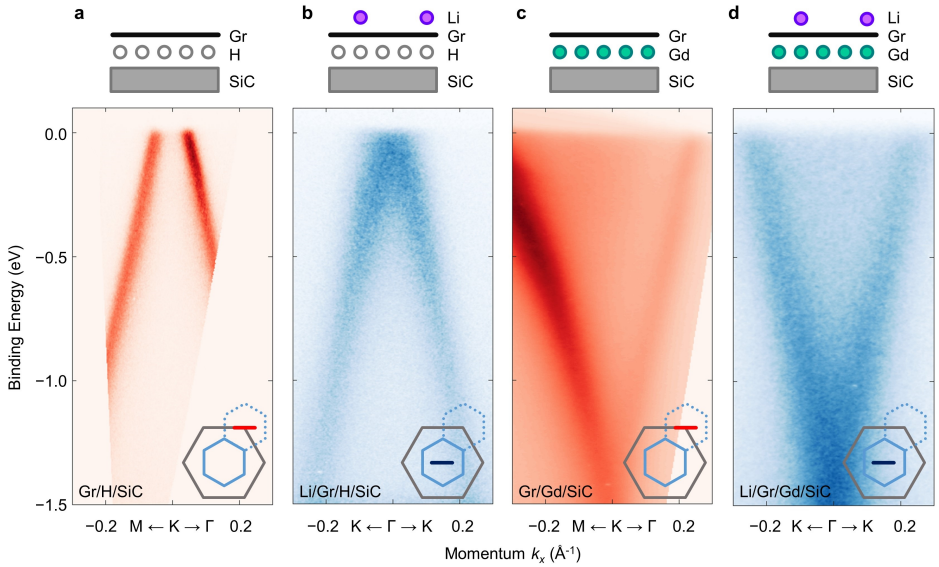

Figure 5.16: Kekulé phase in other graphene systems. (a) ARPES data taken at the K point (cut indicated by inset) on hydrogen-intercalated monolayer graphene (sample schematic is shown above the spectra). The Dirac point is located ∼100 meV above E_F. **(b)** Spectra at Γ on hydrogen-intercalated graphene after lithium deposition showing the folded Dirac cone. **(c)** Spectra at K on gadolinium-intercalated monolayer graphene (sample schematic is shown above the spectra). The Dirac point is located ∼1.6 eV below E_F. **(d)** Spectra at Γ on gadolinium-intercalated graphene after lithium deposition showing the folded Dirac cone. Adapted from [142].

samples is shown in Figure 5.17: on the Gr/Gd/SiC sample, the electron pockets are much larger, and strong triangular warping of the Dirac cone is evident. As with the Gr/SiC samples, no spectral weight is present at Γ on the pristine Gr/H/SiC and Gr/Gd/SiC, but a folded cone appears after lithium decoration (Figure 5.16(b) and (d)).

We can estimate the charge carrier density in each of the graphene systems using the area of the Fermi surface via $n_e = 2A_{FS}/A_{BZ}$, where n_e is the number of electrons per unit cell, A_{FS} is the area of the Fermi surface, A_{BZ} is the area of the BZ, and the factor of 2 accounts for spin degeneracy. This corresponds to $\rho_e \approx 1 \times 10^{13}$ cm^{-2} for the Gr/SiC sample,

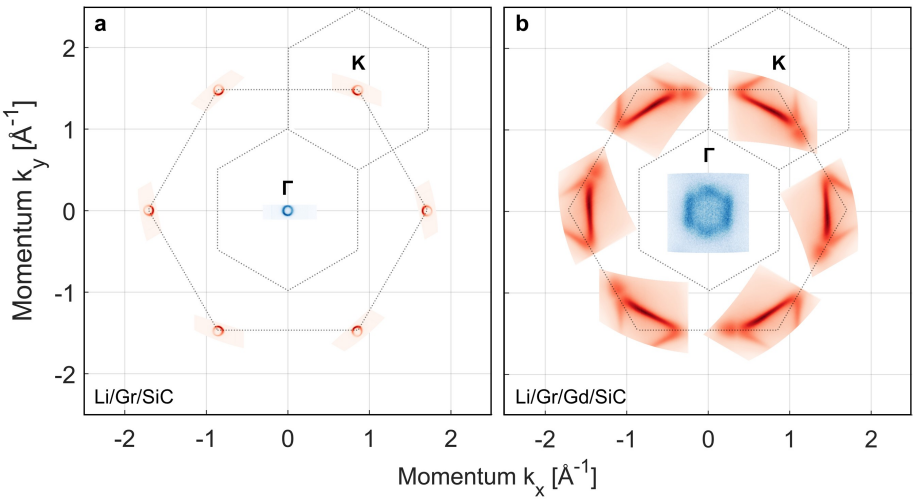

Figure 5.17: Full Fermi surfaces on different graphene systems. (a) Fermi surfaces near Γ (blue) and K (red) taken on Gr/SiC using *s*-polarized light are shown to scale (BZ boundaries indicated by dotted grey lines). The spectra near the top left K point is rotated to produce the remaining K spectra. The electron pockets are small compared to the total area of the BZ. **(b)** The same Fermi surfaces are shown for Gr/Gd/SiC. The electron pockets clearly grow in size, and strong triangular warping of the Dirac cone is observed due to the high electronic doping. The folded cone at Γ appears distinctly hexagonal due to the triangular electron pockets and matrix element effects.

$\rho_h \approx 4 \times 10^{12}$ cm^{-2} for the Gr/H/SiC sample, and $\rho_e \approx 5 \times 10^{14}$ cm^{-2} for the Gr/Gd/SiC sample. In the case of the Gr/Gd/SiC, this carrier density far exceeds even our upper limit for the lithium adatom density, $\rho \approx 10^{14}$ cm^{-2}, and thus the formation of Kekulé ordering should be disrupted [153]. However, a folded Dirac cone indeed appears at Γ following lithium decoration for all three samples. These results are particularly interesting as they show that the Kekulé phase continues to manifest despite the lack of a nesting condition at E_F corresponding to the $(\sqrt{3} \times \sqrt{3})R30°$ superstructure (as can be clearly seen in maps of the full Gr/Gd/SiC Fermi surface in Figure 5.17(b)), in contrast to the case of the 1D Peierls distortion [131].

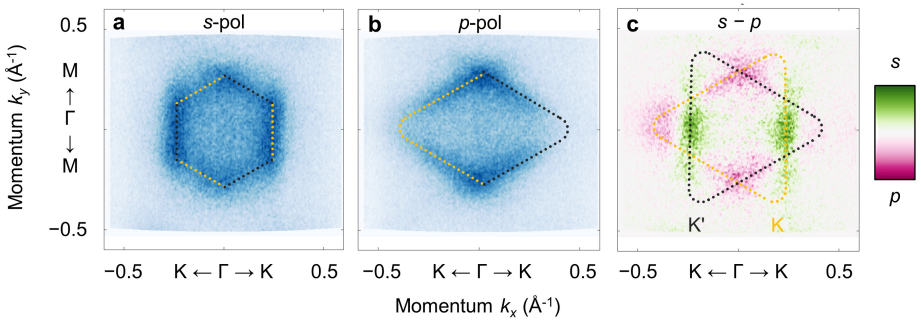

Figure 5.18: Folded Fermi surface on Gr/Gd/SiC. (a) Fermi surface near Γ on gadolinium-intercalated graphene after Lithium deposition using *s*-polarized light. A schematic of the bands expected to be visible in this configuration is overlaid in yellow and grey dotted lines. **(b)** The same Fermi surface as in (a) using *p*-polarized light. **(c)** Difference map between (a) and (b). A schematic of the triangular Fermi surfaces folded from K and K′ is overlaid in yellow (K) and grey (K′) dotted lines. Note that the top and bottom corners of the hexagram pattern are absent; circularly-polarized or unpolarized light is needed to visualize these areas. Adapted from [142].

The folded bands of the Gr/Gd/SiC sample are particularly striking: due to the triangular warping, the Dirac cones fold into a hexagram-like Fermi surface at Γ. Due to matrix element effects in ARPES, only parts of it can be observed using polarized light [144]. Figure 5.18(a) and (b) show the same Fermi surface at Γ from the Gr/Gd/SiC sample, observed using *s*- and *p*-polarized light, respectively. Figure 5.18(c) shows the difference between the two polarizations, overlaid with a schematic of the folded bands from K and K′; the top and bottom corners of the hexagram are absent in both polarizations, but may be observable using circularly-polarized light [154].

Despite significant differences in the size and carrier type of the Fermi surfaces, we observe signatures of Kekulé order across all three graphene systems. The origin of this robustness of Kekulé ordering to electron density is currently unclear. The insensitivity to Fermi surface size rules out Fermi surface nesting for the observed lattice instability, as in the traditional one-dimensional Peierls distortion [131, 155]. In fact, the Fermi surfaces of many typical CDW systems such as $NbSe_2$ deviate from perfect nesting conditions

[155].

One possibility is that the Kekulé phase we observe is driven by the electron-phonon interaction, which is particularly strong in graphene [156]. Specifically, the A_{1g} "breathing mode" phonon of graphene, in which the carbon rings vibrate radially, distorts the same bonds as the Kek-O texture, and ARPES experiments have shown that electrons in graphene couple particularly strongly to the A_{1g} phonon [157].

Indeed, theorists have found that it is so far not possible to model a stable CDW without allowing the atomic positions in the lattice to move, and in real systems, electronic and lattice distortions always occur simultaneously [155]. Combined with the lack of perfect nesting conditions in many CDW systems, this suggests that the CDW is a result of the lattice distortion, rather than vice versa [155].

5.3.5 A Monte Carlo toy model for deposition

In order to reliably induce the Kekulé phase in graphene via the HKO mechanism, we employ two key experimental conditions: (i) lithium is deposited *in situ* with graphene held at low temperature (< 10 K) and (ii) a shutter preventing a direct line of sight to the sample is used to drastically reduce the lithium deposition rate. To better understand how these deposition conditions affect hidden Kekulé ordering, we use a simple hopping model that incorporates the graphene-mediated long-range interaction between adatoms on graphene [139].

In this model, a graphene flake is represented by a lattice of hollow sites, each of which can be occupied by an adatom (Figure 5.19). Each site is assigned a "colour index" m that takes values -1, 0, or $+1$ (red, grey, or blue) corresponding to the three inequivalent unit cells of the $(\sqrt{3}\times\sqrt{3})R30^\circ$ superstructure. In Figure 5.19, these sites are represented by coloured dots: small if the site is empty, and large if the site is occupied by an adatom. Two adatoms i and j on the flake are allowed to interact via

$$V_{ij} = -J\frac{\vec{u}_i \cdot \vec{u}_j}{|\vec{r}_i - \vec{r}_j|^3 \rho^{3/2}}, \tag{5.3}$$

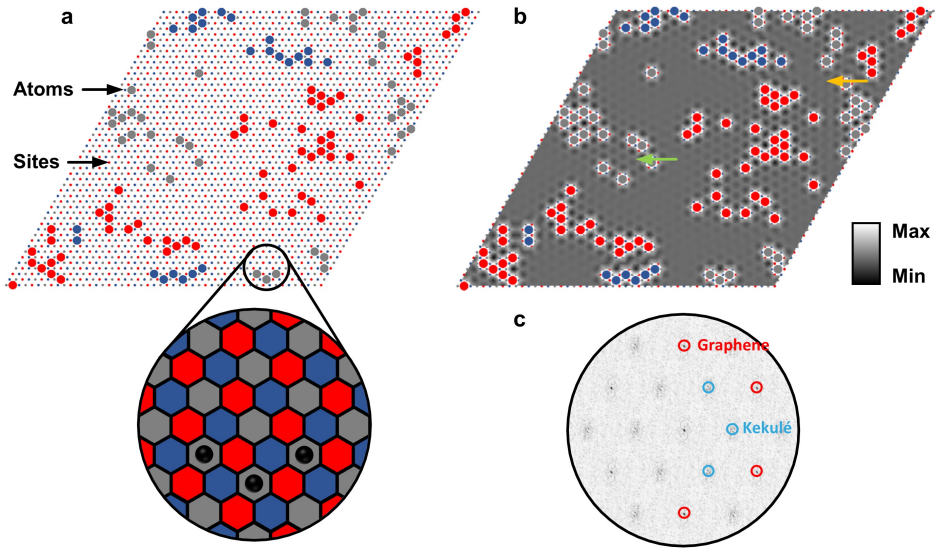

Figure 5.19: A toy model for adatoms on a graphene flake. (a) A red-grey-blue coded graphene flake (magnifier view, bottom) is represented as a lattice of hollow sites (coloured dots). Each site can be occupied by an adatom (large dots) or empty (small dots). **(b)** Simulated potential (Equation 5.3) of empty sites as seen by an incoming atom (occupied sites have infinite potential to prevent double occupancy). In areas where adatoms all occupy sites of the same colour, empty sites of the same colour are preferred (green arrow). In areas between different colours, interference occurs and neither colour is as strongly preferred (yellow arrow). **(c)** Analytical Fourier transform of the occupied sites in (a). Each occupied site is treated as a delta function. The peaks corresponding to the graphene (red) and Kekulé density wave (blue) are circled. Sharper peaks indicate more order in the system.

where the interaction energy J is defined as

$$J = \frac{\lambda^2}{2}(a^2\rho)^{3/2}\frac{h\nu}{a} \tag{5.4}$$

and

$$\vec{u}_i \cdot \vec{u}_j = \cos\frac{2\pi(m_i - m_j)}{3}. \tag{5.5}$$

is $+1$ for i and j occupying sites with the same colour, and $-1/2$ for different colours, analogous to a "ferromagnetic" interaction with three spins [139]. Note that Equation 5.3 is only valid for large interatomic distances $|\vec{r}_i - \vec{r}_j| \gg a$, and thus this model does not accurately represent high adatom coverages where other interactions such as Coulomb repulsion may dominate. Additionally, this model neglects any modulations of the Friedel oscillations due to the finite charge carrier density [139].

An example of a potential landscape seen by an incoming adatom is shown in Figure 5.19(b): red, grey, and blue sites are available, and when no adatoms are present, the three colours are equivalent. However, when an adatom is added to e.g. a red site, symmetry breaking occurs and selectively decreases the potential energy of nearby red sites while also increasing that of blue and grey sites. Thus, a new adatom will prefer to occupy a red site rather than a blue or grey one, and the effect is compounded as more red sites are filled. However, if a nearby adatom occupies a blue site instead, interference occurs between the red and blue adatoms, thus destroying the preference for red or blue sites. If the filling is sufficiently random, then no phase coherence can occur and no single colour is preferred.

An indication of the amount of Kekulé order present in the system is given by the Fourier transform of the flake, calculated analytically by treating each occupied site as a δ function, summing, and normalizing by the total number of adatoms (Figure 5.19(c)). The intensity of the peaks corresponding to the $(\sqrt{3} \times \sqrt{3})$ R30° superstructure (blue circles) is then compared to that of the graphene peaks (red circles). When all adatoms occupy sites of the same colour, the two are equal; when adatoms are randomly arranged, their ratio is typically around 0.2 for $\sim$5% of sites occupied, and drops to 0 when every site is occupied.

Next, we allow adatoms to hop to the nth unoccupied nearest-neighbour site (or remain on the original site) with probability

$$P_n = \frac{e^{-E_n/k_BT}}{\sum_n e^{-E_n/k_BT}} \tag{5.6}$$

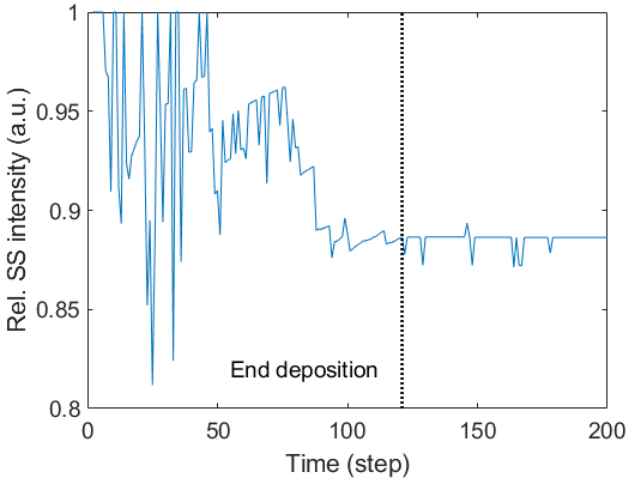

Figure 5.20: Ordering in the system during deposition. Intensity of the $(\sqrt{3} \times \sqrt{3})$ R30° superstructure peak relative to the graphene peak in the Fourier transform is shown as a function of time during and after an example deposition process. Here, $J/k_BT = 1$ and 120 atoms are deposited one at a time. After the deposition, the system is allowed an additional 80 time steps to settle.

where E_n is the sum of potentials contributed to site n by all other adatoms. This provides us with a simple model for the thermal evolution of adatoms on graphene.

To demonstrate the effect of various deposition rates, a total of 120 atoms are added randomly to a 50×50 graphene flake, several at a time, and the present adatoms are allowed to evolve thermally via Equation 5.6 after each addition. After the simulated deposition, the system is allowed to evolve further to come to equilibrium. An example of such a deposition is shown in Figure 5.20, with $J/k_BT = 1$ and 120 atoms deposited one at a time, followed by 80 time steps to equilibriate the system.

Typical end results for 1 and 120 atoms/step are shown in Figure 5.21(a) and (b), respectively, for $J/k_BT = 1$. The slower deposition (Figure 5.21(a)) produces large areas where all adatoms occupy sites of the same colour, resulting in coherent order across the entire 50×50 flake and sharp peaks in

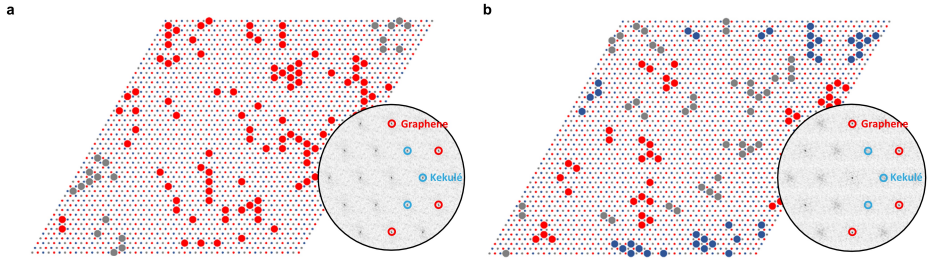

Figure 5.21: Typical results of adatom deposition. (a) 120 adatoms (large dots) are added randomly to hollow sites on a 50×50 graphene flake (small dots) one at a time. The $(\sqrt{3} \times \sqrt{3})$ R30° periodicity is indicated by the red-grey-blue colour scheme. The system is allowed to evolve thermally according to Equation 5.3 ($J/k_BT = 1$) after each addition. The final state of the flake is shown alongside its Fourier transform, overlaid with the theoretical peak positions of the graphene lattice (red circles) and the $(\sqrt{3} \times \sqrt{3})$ R30° superstructure (blue circles). The formation of a large single-colour crystal is observed, as well as sharp peaks in the Fourier transform corresponding to the superstructure. **(b)** 120 adatoms are added to the same flake in a single step and allowed to evolve thermally. Single-colour patches are much smaller than those formed during a slow deposition, and the superstructure peaks in the Fourier transform are broad.

the Fourier transform (inset), while the faster deposition (Figure 5.21(b)) only permits order on the scale of a few sites, and the intensity of the superstructure peaks in the Fourier transform (inset) is weak.

Figure 5.22 shows the ratio between the superstructure and graphene peaks after a deposition, as a function of deposition rate (number of atoms deposited at a time), for three different temperatures. Each data point represents the mean and standard deviation of 100 iterations of the simulation. For the lowest temperature shown ($J/k_BT = 1.0$, blue dots), slower depositions clearly produces more prominent ordering than faster depositions, supporting our experimental results. As the temperature increases, more thermal energy is available to disrupt the Kekulé superstructure, and the effect of the deposition rate is less apparent. For the highest temperature shown ($J/k_BT = 0.1$, yellow dots), the deposition rate makes very little difference to the ordering. A crossover occurs around 30 atoms/step: above

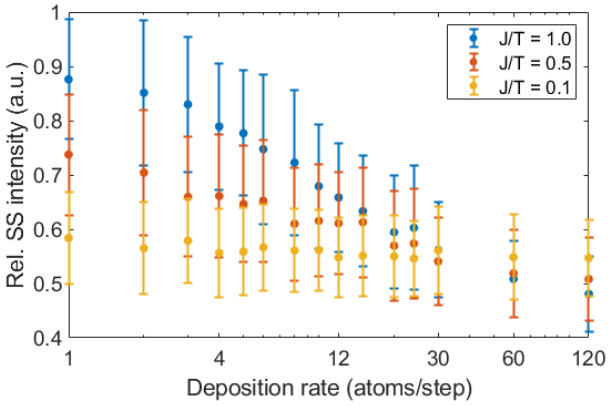

Figure 5.22: Effect of deposition rate and temperature. Intensity of the $(\sqrt{3} \times \sqrt{3})$ R30° superstructure peak relative to the graphene peak in the Fourier transform is shown as a function of the number steps taken to deposit 120 adatoms, for different values of J/k_BT. A slow deposition at low temperature produces the most Kekulé order; at high temperatures, it is difficult to obtain Kekulé order at any deposition rate. A crossover occurs at approximately 30 atoms/step: beyond this rate, lower temperatures are no longer beneficial to the formation of Kekulé order since atoms no longer have sufficient time to order.

this deposition rate, colder depositions result in *less* ordering. A possible explanation is at lower temperatures, the system is less able to move multiple atoms to pass through unfavourable states to get to more favourable ones, and it becomes "stuck" in states with less ordering.

The results from this model are consistent with the observations from Section 5.3.3: isolated adatoms on a different colour lattice from their neighbours sit in a shallower potential and are thus more likely to move as the temperature increases, destroying the Kekulé phase starting from areas with the least order.

5.4 Summary

In this chapter, we demonstrated a method of reliably inducing Kekulé bond order in epitaxial graphene through dilute lithium adatom decoration. Using

ARPES, we were able to directly visualize an extremely sharp folding of the graphene bands due to the superstructure associated with Kekulé order, which was also confirmed using LEED. By careful analysis of the ARPES spectra, we observed a band gap $2\Delta_{ab} = (292 \pm 4)$ meV at the Dirac point on pristine Gr/SiC due to sublattice symmetry breaking by the substrate. This gap further opens to (377 ± 2) meV after lithium decoration, corresponding to $2\Delta_{kek} = (238 \pm 3)$ meV. Although the lithium adatoms are only stable up to approximately 30 K, the size of the gap opening suggests that with different species of adatoms, this phase may be stable up to over 600 K.

Additionally, we were able to show that this instability appears to be generic to multiple graphene systems, even at extremely high charge carrier densities when the Fermi surface nesting does not at all correspond to the Kekulé periodicity. While the mechanism behind this instability is currently unknown, one possibility is that it may be driven by electron-phonon interactions. These results demonstrate that superlattices of dilute adsorbed atoms offer an attractive alternative route towards tailoring the properties of graphene and possibly other two-dimensional materials.

Chapter 6

Accessible Cu intercalation in epitaxial graphene

6.1 Introduction

In Section 3.5.1, we briefly discussed the epitaxial growth of graphene on a SiC substrate [29, 119, 120]. This method shows great promise for producing graphene on a wafer scale for applications in electronics. We previously noted that due to dangling bonds from the SiC, the first carbon layer to grow ("zeroth layer" or "buffer layer") resembles graphene atomically, but does not exhibit the characteristic electronic properties of graphene. One method of decoupling this layer from the substrate is to grow a second carbon layer: the bottom layer saturates the SiC bonds, while the top layer behaves as quasi-free-standing graphene [29, 119].

A different method for decoupling the buffer layer from the substrate is through intercalation, where atoms are added between the buffer layer and substrate. These atoms bond to the substrate, thus freeing the buffer layer to become monolayer graphene [52, 120]. These intercalated atoms can produce additional effects in the graphene layer: in Chapter 5, for example, we studied a H-intercalated graphene/SiC sample in which charge carriers were holes instead of electrons [52], as well as a Gd-intercalated sample where the graphene was doped to the VHS at the M point, resulting in significant

changes of the Fermi surface [60]. Au-intercalated graphene/SiC can be either hole-doped or strongly electron-doped depending on the gold coverage [158], while Bi-intercalated graphene on Ir(111) induces a gap opening at the graphene Dirac point [159]. In bilayer graphene, Ca intercalation results in superconductivity below ∼4 K [65, 66]. Even C_{60} molecules can be intercalated below a graphene sheet, resulting in local strain and deformation [160].

The intercalation process itself, however, can often be challenging. Typically, this involves evaporating the intercalant material onto the graphene sample and providing it with enough thermal energy to migrant below the graphene. In the case of the two samples studied in Chapter 5, the hydrogen is intercalated by heating the graphene sample in hydrogen gas at atmospheric pressure between 600°C and 1000°C [52]. The gadolinium is first deposited via *e*-beam evaporation, then intercalated by annealing at 1200°C [60]. In addition, the gadolinium-intercalated graphene is sensitive to oxidation and cannot be stored in atmosphere.

In this chapter, we present a simple method of intercalating Cu between graphene and the SiC substrate without the need for evaporation, resulting in a material which is stable for long periods of time even in ambient conditions. We confirm the growth of high-quality Cu-intercalated bilayer graphene using STM, ARPES, and LEED.

6.2 Methods

Monolayer graphene samples were grown epitaxially on hydrogen-etched silicon carbide (SiC(0001)) substrates under argon atmosphere [29, 120]. The sample was mounted to molybdenum sample holders using Cu paste for electrical and thermal contact. The Cu paste was first cured at 200°C in air, then annealed at 600°C in UHV overnight. The sample was annealed again at 600°C before each experiment.

STM experiments were performed at the University of British Columbia in two commercial Scienta Omicron systems, an LT-STM and a Tesla JT SPM. Experiments in the LT-STM were performed at 4 K, while experiments

in the Tesla JT SPM were performed at 1 K. The chamber pressure was better than 5×10^{-10} mbar during all STM experiments.

ARPES experiments were performed in the same UHV system as the Tesla JT SPM, in a chamber equipped with a Scienta Omicron R3000 Hemispherical Analyzer and a FOCUS VUV Source HIS 13 helium discharge lamp producing 21.2 eV photons. The sample was at room temperature, and the chamber pressure was better than 5×10^{-9} mbar during the experiment. The energy resolution was approximately 20 meV for the settings used. LEED experiments were performed in a commercial Scienta Omicron MBE system with the sample at room temperature.

X-ray photoelectron spectroscopy (XPS) experiments were performed at the REIXS Surface Science Facility at the Canadian Light Source using 1486.6 eV photons (Al K_α line).

For a full description of the samples and systems used in this chapter, see Chapter 3 and Chapter 4.

6.3 Results

6.3.1 Appearance of patterned islands

Typical topography observed by STM on pristine areas of the graphene/SiC samples (V_{bias} = 30 mV, I_{set} = 30 pA) is shown in Figure 6.1(a). Two honeycomb patterns are observed: the smaller, with a roughness of ∼0.2 Å, has a periodicity of ∼2.4 Å, in good agreement with the graphene lattice with lattice constant 2.46 Å. The larger, with a roughness of ∼0.5 Å, has a periodicity of ∼1.8 nm, corresponding to a (6×6) reconstruction of the underlying SiC substrate with lattice constant 3.08 Å. These observations are consistent with other STM studies of graphene/SiC [29, 52, 161, 162, 163, 164, 165].

The ∼1.8 nm structure can be attributed to the lattice mismatch between the SiC and the carbon-rich buffer layer under the graphene layer, which resembles graphene atomically but not electrically (for details, see Section 3.5.1). Figure 6.1(b) shows an overlay of the graphene (blue) and

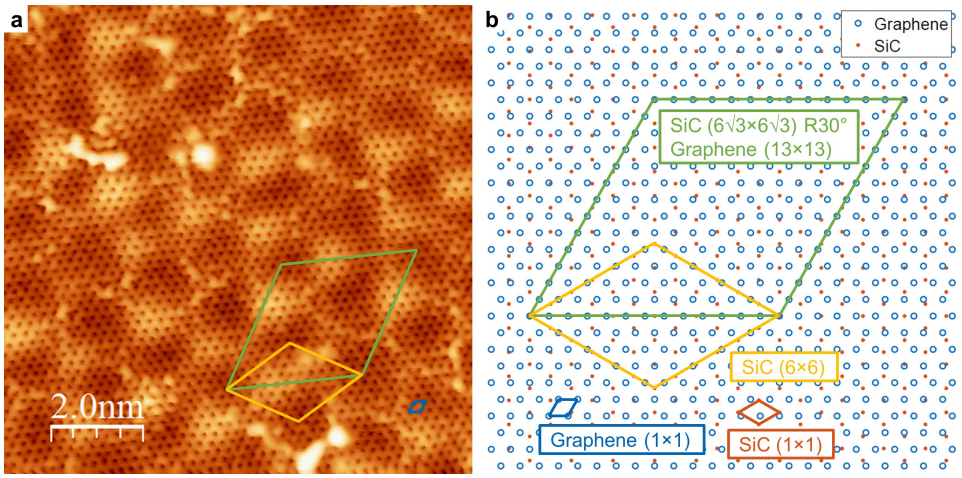

Figure 6.1: Pristine graphene/SiC structure. **(a)** STM topograph on pristine areas of the graphene/SiC ($V_{bias} = 30$ mV, $I_{set} = 30$ pA). The smaller corrugation, with a roughness of ∼0.2 Å, has periodicity ∼2.4 Å and corresponds to the graphene lattice. The larger corrugation, with a roughness of ∼0.5 Å, has periodicity ∼1.8 nm and corresponds to the SiC (6×6) quasi-cell. The graphene (1×1) (blue), SiC (6×6) (yellow), and SiC $(6\sqrt{3} \times 6\sqrt{3})$ R30° (green) cells are indicated. **(b)** Schematic showing the graphene lattice (blue circles, $a = 2.46$ Å) superimposed on the SiC lattice (orange dots, $a = 3.08$ Å). The graphene and SiC unit cells are indicated in blue and orange, respectively. The SiC (6×6) cell is indicated in yellow, but it is incommensurate with the graphene lattice. The SiC $(6\sqrt{3} \times 6\sqrt{3})$ R30° cell, matching the graphene (13×13) cell to $< 1\%$, is indicated in green.

SiC (orange) lattices, with the unit cells shown in the corresponding colours. The SiC (6×6) cell is shown in yellow; however, it is incommensurate with the graphene lattice, and thus is sometimes referred to as a quasi-cell [162]. The actual superstructure is the SiC $(6\sqrt{3} \times 6\sqrt{3})$ R30° cell (green), which matches the graphene (13×13) cell.

After repeated annealing, we observe that an increasing proportion of the sample surface becomes covered by raised islands. An example of such an island is shown in Figure 6.2(a) ($V_{bias} = 100$ mV, $I_{set} = 10$ pA). They are ∼2.2 Å taller than the pristine surface, as shown by the height profiles in Figure 6.2(b) and (c) (taken at the blue and green dotted lines in Figure 6.2(a)

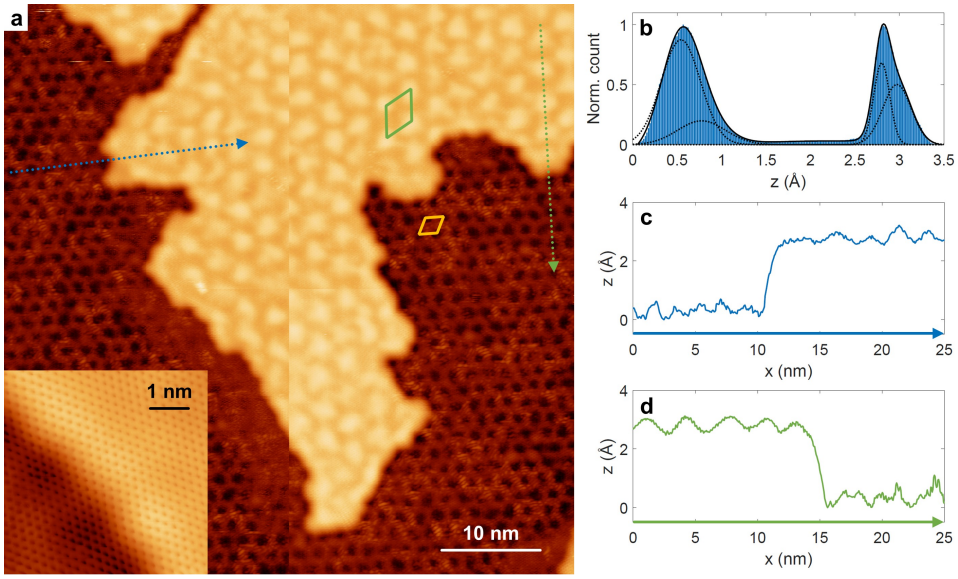

Figure 6.2: Cu-intercalated islands on graphene/SiC. (a) STM topograph on graphene/SiC after repeated annealing at 600°C ($V_{bias} = 100$ mV, $I_{set} = 10$ pA). The SiC (6×6) quasi-cell is indicated in yellow. Islands of height ∼2.2 Å are observed, also with a roughness of ∼0.5 Å but a periodicity of ∼3.2 nm, corresponding to the SiC ($6\sqrt{3} \times 6\sqrt{3}$) R30° cell (indicated in green). The edges of the islands follow the SiC (6×6) structure. The graphene lattice continues smoothly over these edges (inset, $V_{bias} = 100$ mV, $I_{set} = 2$ pA). **(b)** Height distribution of the topograph in (a) showing the ∼2.2 Å height difference on and off the island. Due to the corrugation on and off the island, each peak is fit to two Gaussian distributions. The ∼2.2 Å distance is calculated by the difference between the average centres of each pair of Gaussians. **(c)** Height profile taken along the blue dotted line in (a), showing the ∼2.2 Å height of the island. **(d)** Height profile taken along the green dotted line in (a), showing the same ∼2.2 Å height of the island.

respectively). More strikingly, they exhibit a change in periodicity compared to the pristine surface: specifically, the SiC (6×6) quasi-cell (Figure 6.2(a), yellow rhombus) is replaced by the SiC $(6\sqrt{3} \times 6\sqrt{3})$ R30° superstructure (Figure 6.2(a), green rhombus). The contrast is also inverted: while the "hollow" parts of the SiC (6×6) honeycomb were lower than the rest, they are higher on the SiC $(6\sqrt{3} \times 6\sqrt{3})$ R30° pattern. The edge of the these islands follow the SiC (6×6) pattern. The graphene lattice is continuous over the step (Figure 6.2(a), inset, $V_{bias} = 100$ mV, $I_{set} = 2$ pA), suggesting that the island is formed underneath the graphene.

Another piece of evidence pointing towards intercalation is the appearance of the SiC $(6\sqrt{3} \times 6\sqrt{3})$ R30° periodicity. As the SiC (6×6) quasi-cell is not the "true" superstructure of the graphene/SiC interface, there are three inequivalent "versions" of this cell. Figure 6.3(b) shows the superimposed graphene (blue circles) and SiC (orange dots) lattices once again: the first SiC lattice point of each (6×6) quasi-cell is highlighted in red, grey, or blue, corresponding to the $(6\sqrt{3} \times 6\sqrt{3})$ R30° periodicity. While the red-highlighted SiC lattice points are directly below a graphene lattice point, the grey- and blue-highlighted SiC lattice points sit equidistant from three graphene lattice points. It is likely, then, that the emergence of the $(6\sqrt{3} \times 6\sqrt{3})$ R30° superstructure is related to the interaction between the intercalant and this structure, breaking the apparent symmetry of the three (6×6) quasi-cells.

Figure 6.3(a) shows part of the STM image from Figure 6.1(a), overlaid by a lattice with periodicity corresponding to the SiC (6×6) quasi-cell and lattice points aligned with the "hollow" areas of the (6×6) pattern. (Note that the dotted lines are not part of the Bravais lattice, but intended as guides to the eye.) The "hollow" areas of the SiC $(6\sqrt{3} \times 6\sqrt{3})$ R30° pattern (periodicity shown by the red-highlighted triangles) are observed to align with the Y-shaped "top" areas (between the "hollow" areas) of the (6×6) pattern. From this, a proposed correspondence between the graphene/SiC interface and the STM image on the pristine surface is shown in Figure 6.3(b), with the "hollow" areas of the (6×6) pattern indicated by the large grey shaded circles. The red-highlighted "top" areas in Figure 6.3(b) correspond to the red-highlighted triangles in Figure 6.3(a).

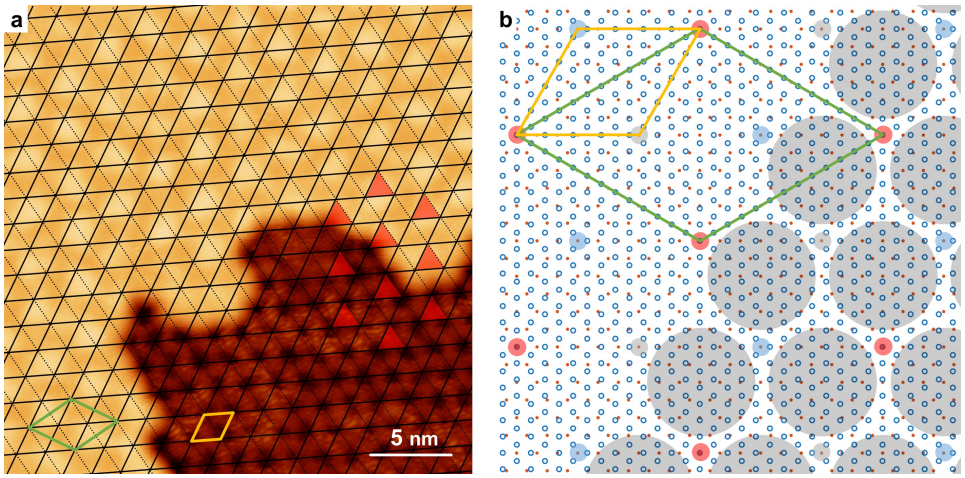

Figure 6.3: Matching the STM image and atomic structure. (a) A lattice with periodicity corresponding to the SiC (6×6) quasi-cell is overlaid on part of the STM image from Figure 6.1(a). The taller areas of the SiC $(6\sqrt{3} \times 6\sqrt{3})$ R30° pattern correspond to the Y-shaped areas between the lower areas of the (6×6) (red triangles). As usual, the SiC (6×6) quasi-cell is indicated in yellow, while the SiC $(6\sqrt{3} \times 6\sqrt{3})$ R30° cell is indicated in green. **(b)** Since the "true" superstructure of the graphene/SiC interface is the SiC $(6\sqrt{3} \times 6\sqrt{3})$ R30° periodicity, the SiC (6×6) lattice can be tiled with three slightly different versions of the quasi-cell. Here the first SiC lattice point (orange dots) of the three versions are colour-coded red, grey, and blue as in Chapter 5. The red-highlighted SiC lattice points sit directly below a graphene lattice point (blue circles); the blue- and grey-highlighted SiC lattice points sit between three graphene lattice points. The areas between these points (large grey circles) are identical up to a rotation. Since the red SiC lattice points differ from the other two, they are a good candidate for the Y-shaped areas in (a) indicated by the red triangles.

Detailed STM images taken on and off the island ($V_{bias} = 100$ mV, $I_{set} =$ 10 pA) are shown in Figure 6.4(a) and (b), respectively. In Figure 6.4(a), the SiC $(6\sqrt{3} \times 6\sqrt{3})$ R30° cell is indicated in green, while in Figure 6.4(b), the SiC (6×6) cell is indicated in yellow. The Fourier transform of these images is shown in Figure 6.4(c) and Figure 6.4(d). The graphene (1×1) spots, indicated in blue, are consistent across both images. The SiC (6×6) and $(6\sqrt{3} \times 6\sqrt{3})$ R30° spots are too close to the origin to be seen, but they

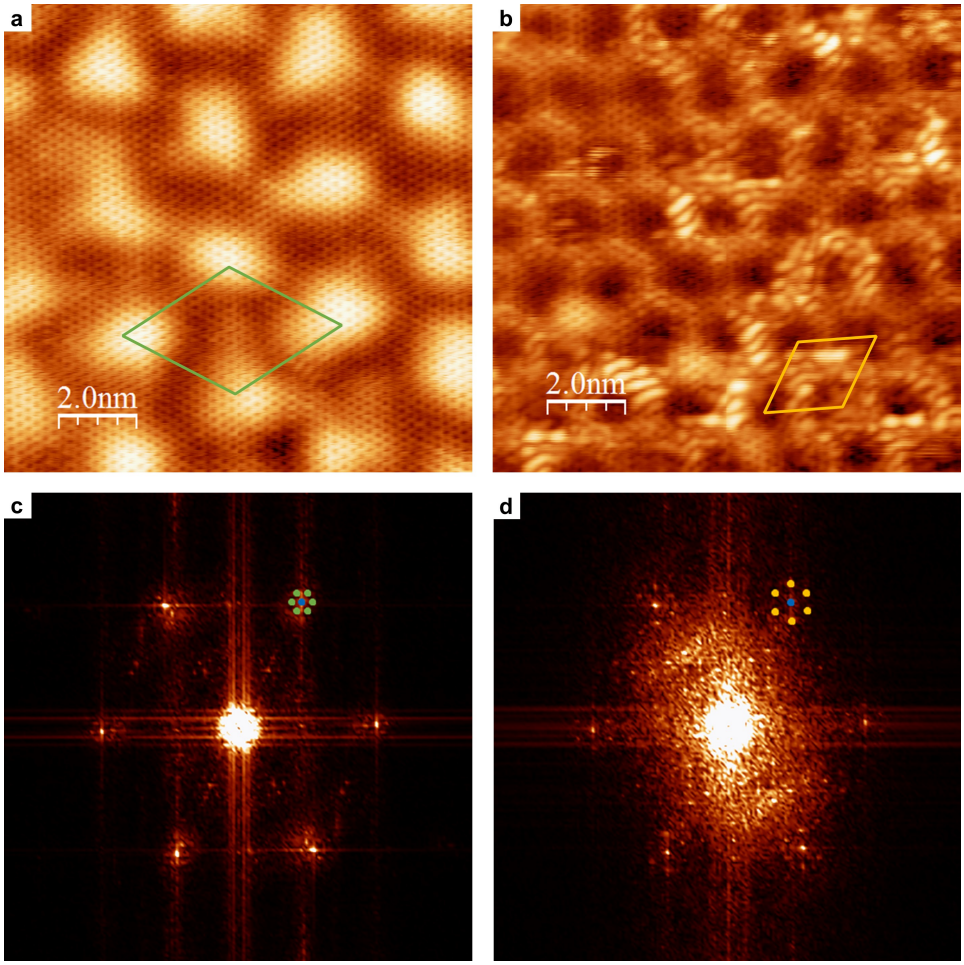

Figure 6.4: Comparing intercalated and bare areas. (a) STM topograph taken on top of a ∼2.2 Å step ($V_{bias} = 100$ mV, $I_{set} = 10$ pA). The SiC $(6\sqrt{3} \times 6\sqrt{3})$ R30° cell is indicated in green. **(b)** STM topograph taken below the ∼2.2 Å step ($V_{bias} = 100$ mV, $I_{set} = 10$ pA). The SiC (6×6) cell is indicated in yellow. **(c)** Fourier transform of the image in (a). Graphene (1×1) spots are indicated in blue; graphene (1×1) plus SiC $(6\sqrt{3} \times 6\sqrt{3})$ R30° are indicated in green. **(d)** Fourier transform of the image in (b). Graphene (1×1) spots are indicated in blue; graphene (1×1) plus SiC (6×6) are indicated in yellow.

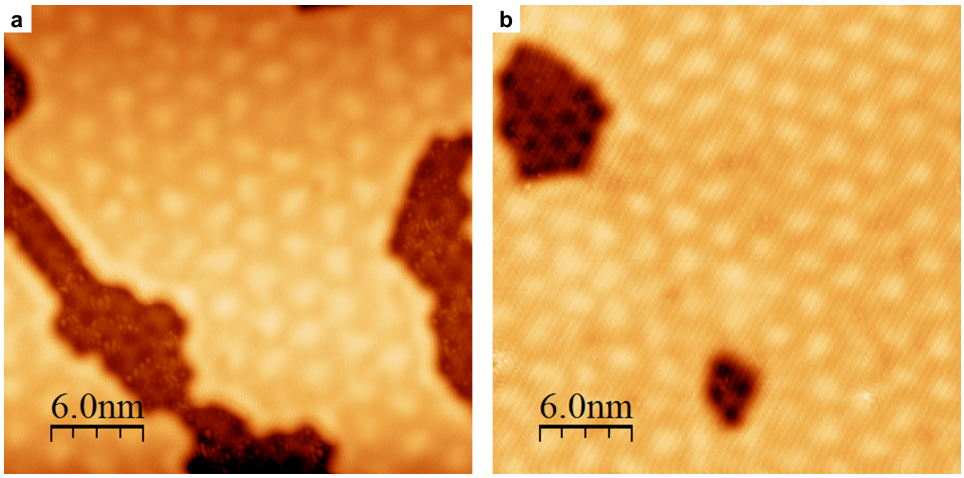

Figure 6.5: High intercalant coverage. **(a)** Example STM topograph taken on a sample almost entirely covered by the ∼2.2 Å islands ($V_{bias} = 200$ mV, $I_{set} = 10$ pA). **(b)** A second example topograph taken on the same sample as (a) ($V_{bias} = 100$ mV, $I_{set} = 10$ pA).

can be observed as satellites of the graphene (1×1) spots. In Figure 6.4(c), the graphene (1×1) plus SiC $(6\sqrt{3} \times 6\sqrt{3})$ R30° spots are indicated in green, while in Figure 6.4(b), the graphene (1×1) plus SiC (6×6) spots are indicated in yellow. The SiC (6×6) spots are not observed in Figure 6.4(c), and vice versa.

On one of the two samples studied, we observe a high coverage of the taller areas, possibly due to the smaller size of the sample. Figure 6.5(a) ($V_{bias} = 200$ mV, $I_{set} = 10$ pA) and (b) ($V_{bias} = 100$ mV, $I_{set} = 10$ pA) show examples of typical topography on this sample.

The coverage is so high, in fact, that we were able to observe the appearance of spots corresponding to the SiC $(6\sqrt{3} \times 6\sqrt{3})$ R30° superstructure in LEED. Figure 6.6(a) shows the LEED pattern taken on a pristine graphene/SiC sample. The graphene (1×1) (blue arrow) and SiC (1×1) (orange arrow) spots are clearly observed; the SiC (6×6) spots (yellow arrow) are partially hidden behind the electron gun, but can be observed as satellites around the graphene (1×1) and SiC (1×1) spots. Figure 6.6(b), meanwhile, shows the LEED pattern taken on the high-coverage sample. Here, the

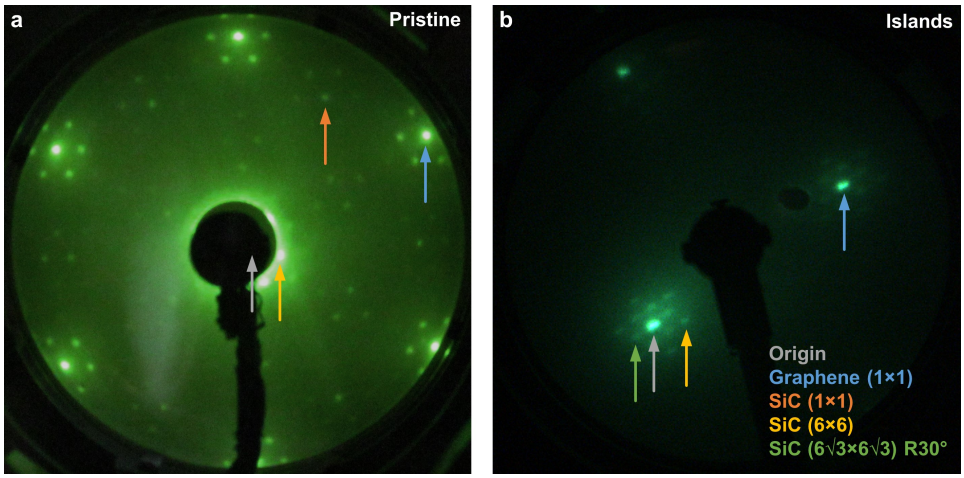

Figure 6.6: Periodicities observed in LEED. (a) LEED pattern taken on a pristine graphene/SiC sample at 66 V. Normal incidence (grey arrow) is hidden behind the electron gun. Graphene (1×1) and SiC (1×1) spots are indicated by the blue and orange arrows, respectively. The SiC (6×6) spots are indicated by the yellow arrow, but are difficult to see behind the electron gun; however, graphene (1×1) plus SiC (6×6) spots are visible around the graphene spots. **(b)** LEED pattern taken on a sample with high intercalant coverage (same sample as shown in Figure 6.5), also at 66 V. The sample is tilted such that normal incidence (grey arrow) is offset from the electron gun. Graphene (1×1) and SiC (6×6) spots are indicated by the blue and yellow arrows as in (a), and the new SiC $(6\sqrt{3} \times 6\sqrt{3})$ R30° spots are indicated by the green arrow. As in (a), graphene (1×1) plus SiC (6×6) spots are visible, with the addition of graphene (1×1) plus SiC $(6\sqrt{3} \times 6\sqrt{3})$ R30° spots, matching the Fourier transforms of the STM topography in Figure 6.4.

sample is tilted such that spots near normal incidence (grey arrow) can be observed. Besides the SiC (6×6) spots (yellow arrow), the SiC $(6\sqrt{3} \times 6\sqrt{3})$ R30° spots (green arrow) are now also visible. Both sets of spots can also be observed as satellites around the graphene spots (blue arrow). These results correspond well to the Fourier transforms of the STM topography shown in Figure 6.4: since LEED averages over a large area, both the SiC (6×6) and $(6\sqrt{3} \times 6\sqrt{3})$ R30° spots are observed. (The SiC (1×1) spots are too weak to be visible in Figure 6.6(b); however, they are observed in the expected location at other electron energies.)

These island features correspond well to previous STM studies of Cu-intercalated graphene [166, 167]. In particular, Yagyu *et al.* intercalated Cu under the carbon buffer layer on SiC to produce quasi-free-standing monolayer graphene, and they observe the same SiC $(6\sqrt{3} \times 6\sqrt{3})$ R30° pattern after intercalation in both STM and LEED [166]. Sicot *et al.*, studying Cu-intercalated graphene on Ir(111), do not observe a change in periodicity, but do observe the formation of ∼2.2 Å tall islands [167]. However, both studies achieved the intercalation of Cu via evaporation prior to annealing at 600–800°C [166, 167], while no Cu was evaporated on our samples.

Since both graphene samples studied have had lithium intentionally deposited on them, an alternative explanation for the formation of these islands could be the intercalation of lithium atoms after deposition and heating. Indeed, studies of lithium-intercalated graphene on SiC also observe the formation of similar islands growing along the SiC (6×6) pattern [163, 168]. However, the SiC $(6\sqrt{3} \times 6\sqrt{3})$ R30° periodicity is not observed on the intercalated areas. More importantly, any intercalated lithium should have desorbed completely by annealing the graphene/SiC at ~ 600°C [163, 168], while we continue to observe a high coverage of these islands even after multiple anneals for several hours (Figure 6.5, Figure 6.6).

To confirm the absence of lithium, we further studied the chemical composition of these samples using XPS. An overview spectrum is shown in Figure 6.7(a). C 1s and Si 2s/2p peaks from the graphene and SiC substrate are clearly observed, as well as the Cu 2p peaks (however, due to the spot size of the x-ray source, it is difficult to distinguish the Cu paste from intercalated Cu). A small Na 1s signal is also observed, possibly due to impurities in the Li source. The Li 1s peak, however, is not observed at -55 eV [169] in the overview spectrum. In a high-resolution scan of this energy range (Figure 6.7(b)), only a very small peak is observed. Although Na contamination in the Li source is <0.2% [170], the Li 1s peak is significantly weaker than the Na 1s, suggesting that most of the Li was indeed removed by the annealing process.

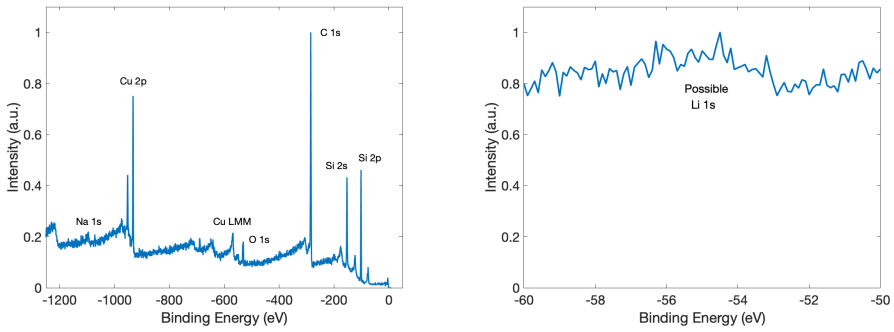

(a) **(b)**

Figure 6.7: XPS on intercalated graphene. **(a)** Overview spectra taken on the intercalated samples. The expected C, Si, and Cu peaks are observed. In addition, O is observed due to oxidation, as well as a small amount of Na, possibly due to contamination of the Li source. No Li peaks are observed near -55 eV binding energy. **(b)** High-resolution scan near the Li 1s binding energy (-55 eV). Only a very weak peak is observed.

6.3.2 Appearance of a doped Dirac cone in ARPES

To confirm the intercalation of Cu in our graphene/SiC samples, we also use ARPES to study its bandstructure (Figure 6.8). The Fermi surface near K as probed by ARPES is shown in Figure 6.8(a), while an energy-momentum cut through K is shown in Figure 6.8(b). The usual Dirac cone is observed (for ARPES measurements on pristine graphene/SiC, see Chapter 5). In addition, a second, fainter Dirac cone is also observed with its Dirac point shifted further away from E_F. Figure 6.8(c) and (d) show the second derivatives of the same two cuts as in (a) and (b), where the new bands are more easily visible.

Figure 6.8(e) shows fits to the spectra: as in Chapter 5, the band positions (thick yellow lines) are obtained by fitting MDCs. A hyperbolic fit through the "normal" Dirac cone (thin solid yellow lines) positions the Dirac point at $\sim$440 meV, comparable to the $\sim$450 meV observed on the pristine samples. However, the substrate-induced gap opening at the Dirac point is reduced to $2\Delta \approx 200$ meV from (292 ± 4) meV (see Section 5.3.2), suggesting a

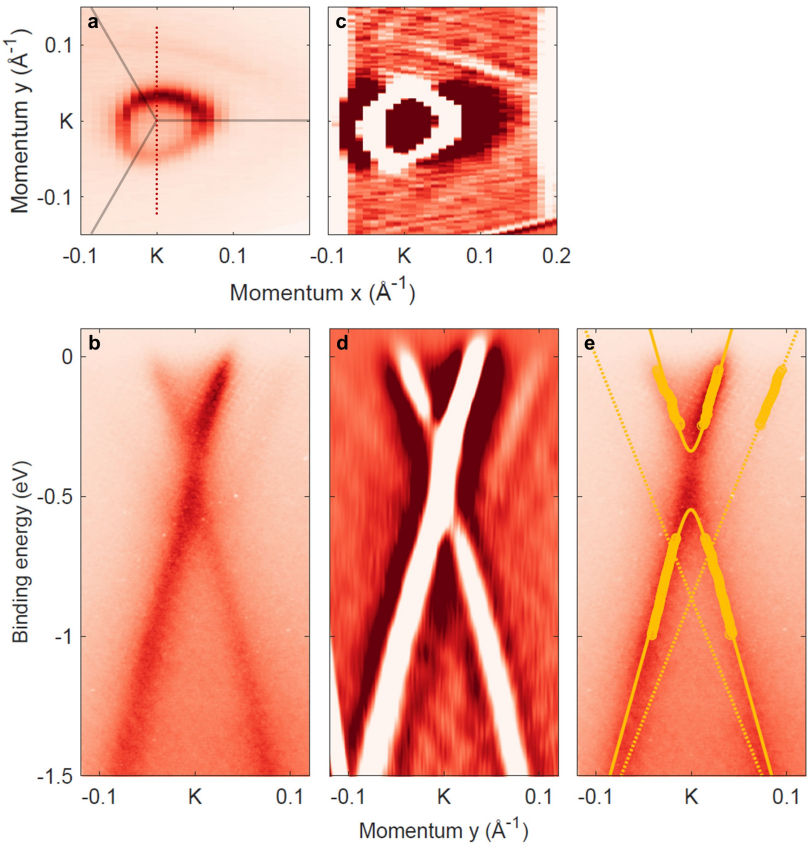

Figure 6.8: Bandstructure of intercalated graphene probed by ARPES. (a) Fermi surface map near K taken on the sample showing high intercalant coverage. The BZ boundaries are indicated by the grey lines. In addition to the expected Dirac cone pocket, a second, larger pocket is faintly visible. **(b)** A single energy-momentum cut through the Dirac cone at K, at the location indicated by the red dotted line in (a). As in (a), the expected Dirac cone is observed, and a second cone, shifted away from the Fermi level, is faintly visible. **(c)** Second derivative map (in k_y) of the image in (a) after Gaussian filtering for easier visualization of the additional bands. **(d)** Second derivative map (in k_x) of the image in (b). **(e)** The position of the bands in (a) (thick yellow lines) are obtained by fitting MDCs. Since the intensity of the doped Dirac cone is very low, only one branch can be fitted above the Dirac point.

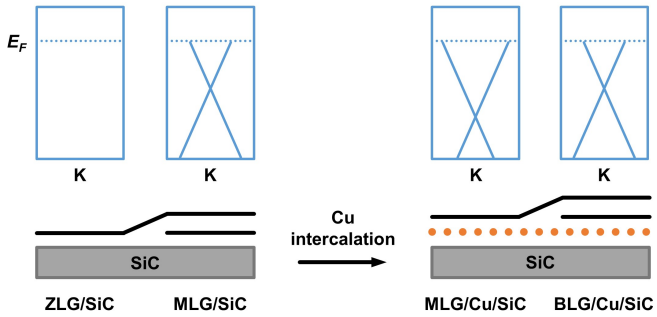

Figure 6.9: Schematic of Cu intercalation and ARPES spectra. Prior to Cu intercalation (left), ZLG (buffer layer only) areas of the SiC does not exhibit the Dirac cone dispersion, while MLG areas produce a "normal" cone in ARPES. After Cu intercalation (right), the ZLG areas become MLG/Cu/SiC, producing a Dirac cone shifted lower in binding energy, while the MLG areas become BLG/Cu/SiC, producing a "normal" cone. When averaged over the ARPES spot size, both the shifted cone and the "normal" cone are observed.

decoupling of the graphene from the substrate.

As for the second, fainter Dirac cone, only one branch of the cone can be determined by fitting MDCs (Figure 6.8(e)). A linear fit to the band position is shown, both through the band and symmetrized across the K point (thin dotted yellow lines). These lines intersect at -0.86 eV, in good agreement with the -0.9 eV observed by Yagyu *et al.* [166] and -0.85 eV observed by Forti *et al.* [171]. This double cone feature is also consistent with observations on other graphene systems intercalated with metals such as Al [172] and Yb [173].

Here we note that both Yagyu *et al.* and Forti *et al.* observe a much stronger intensity for the shifted Dirac cone compared to the "normal" one. This can be attributed to both studies intercalating Cu under the buffer layer to produce quasi-free-standing monolayer graphene, while we intercalate Cu under both the buffer layer and graphene monolayer to produce quasi-free-standing bilayer graphene. To investigate the difference between the two cases, Daukiya *et al.* intercalated Tb atoms in graphene/SiC samples

with varying ratios of buffer and monolayer coverage. They observed that the "normal" cone resulted from intercalation under the monolayer, while the shifted cone resulted from intercalation under the buffer layer [174]. A schematic is shown in Figure 6.9. On our samples, the shifted cone has about 9% of the intensity of the "normal" cone, indicating that the sample was almost completely covered by monolayer graphene prior to intercalation.

6.3.3 Local features of the intercalated areas

Besides the typical ∼2.2 Å islands, we also observe other variations of this structure (Figure 6.10). A second step is sometimes found on top of the ∼2.2 Å islands (Figure 6.10(a), $V_{bias} = 100$ mV, $I_{set} = 20$ pA), measuring ∼1.6 Å tall and possibly corresponding to the intercalation of two Cu layers below the graphene. A profile across such a two-step island is shown in Figure 6.10(b).

We also observe what appears to be areas in the process of intercalation (Figure 6.10(c), $V_{bias} = 100$ mV, $I_{set} = 10$ pA). The SiC (6×6) periodicity is still visible, but the "hollow" areas start to become filled in. A profile taken across the "hollow" areas is shown in Figure 6.10(d): the "bridge" areas do not change significantly in height, but the "hollow" areas are clearly taller than in the pristine areas.

A more careful study of the areas on these ∼2.2 Å islands reveals an assortment of interesting periodic behaviours. Figure 6.11 shows two such areas at different biases. Figure 6.11(a) and (b) are taken on the same area at biases of 100 mV and 300 mV, respectively; stripes with periodicity double that of the graphene lattice are clearly visible. Meanwhile, Figure 6.11(c) and (d) are taken on a different area, also at biases of 100 mV and 300 mV, respectively. Here the periodicity that emerges is a graphene (2×2) superstructure. These features are also consistent with previous STM studies of Cu-intercalated graphene on SiC [166].

The graphene lattice on these islands also appears to be particularly susceptible to lattice distortions. The graphene $(\sqrt{3} \times \sqrt{3})$ R30° superstructure is particularly common (Figure 6.12(a–c)), but a (2×2) superstructure is

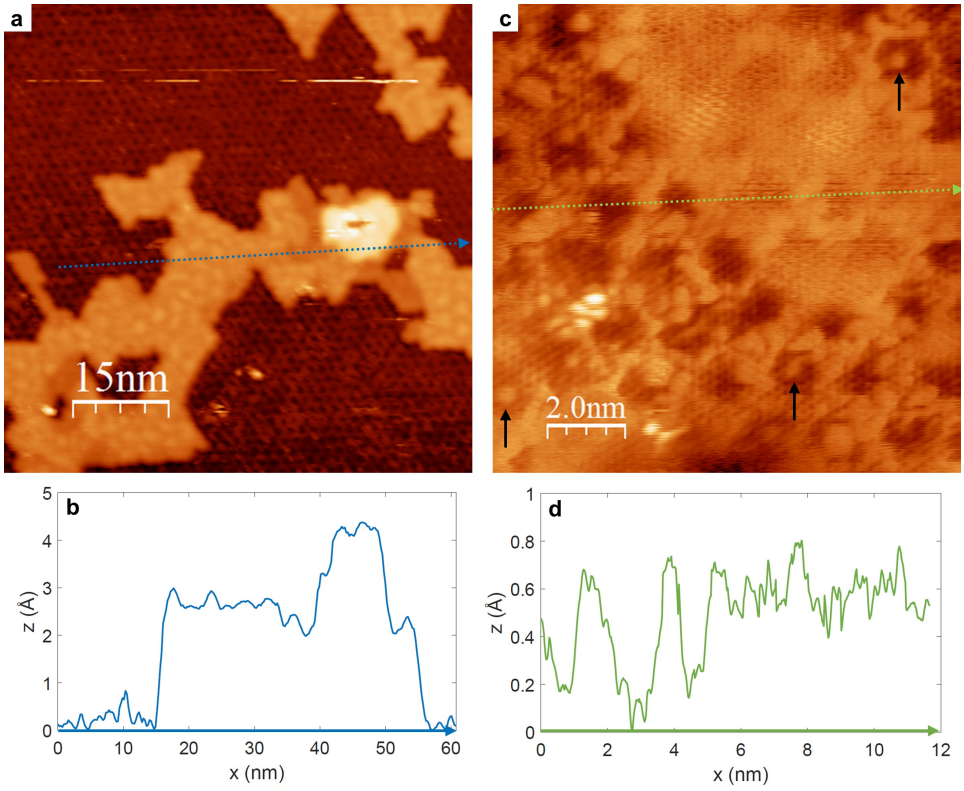

Figure 6.10: Double steps and partial intercalation. (a) STM topograph ($V_{bias} = 100$ mV, $I_{set} = 20$ pA) showing a ∼2.2 Å island. Parts of the island exhibit a second, ∼1.6 Å taller step on top. **(b)** Height profile taken along the blue dotted line in (a), showing the double step. **(c)** STM topograph ($V_{bias} = 100$ mV, $I_{set} = 10$ pA) showing a partially intercalated area. The "hollow" areas of the SiC (6×6) quasi-cell appear to fill in first, with partially-filled quasi-cells indicated by the black arrows. **(d)** Height profile taken along the green dotted line in (c). While the taller parts of the SiC (6×6) quasi-cell show little change on the partially intercalated area, the lower parts are filled in.

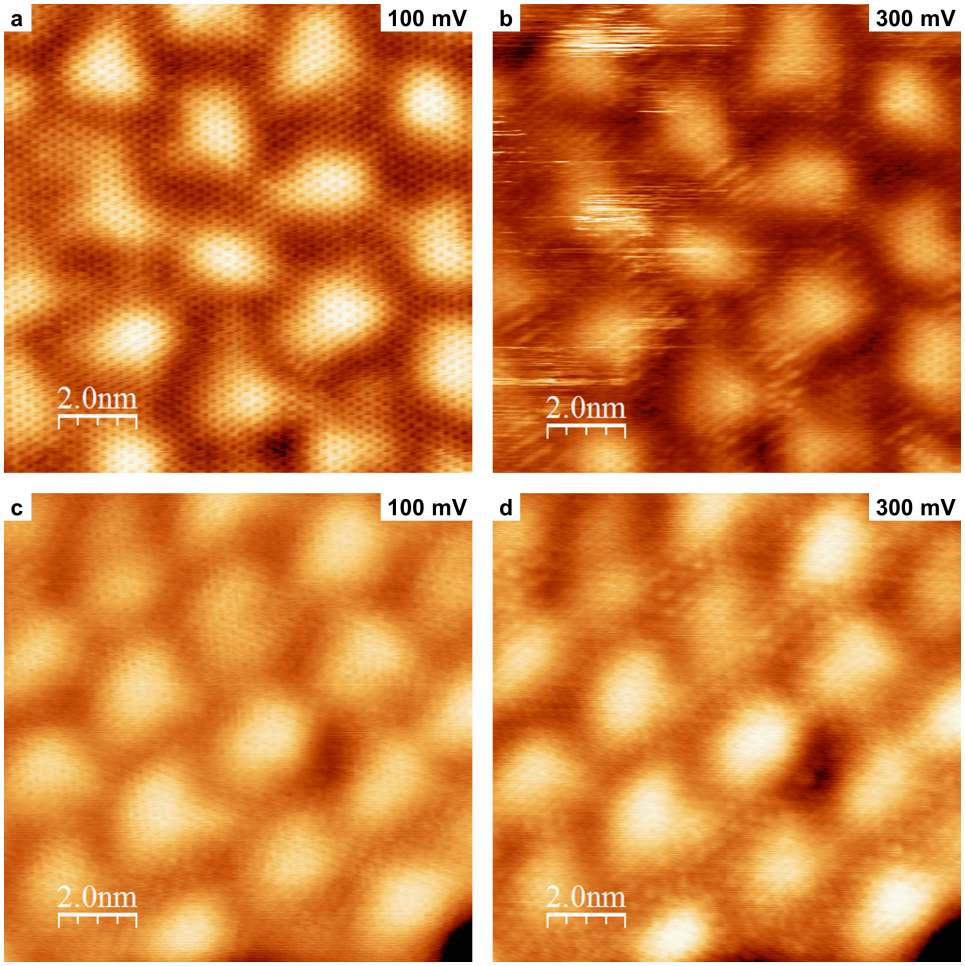

Figure 6.11: Bias dependence of the intercalated areas. **(a)** STM topograph taken on top of a ∼2.2 Å step at $V_{bias} = 100$ mV and $I_{set} = 10$ pA. **(b)** The same topograph as in (a), but taken at $V_{bias} = 300$ mV. We observe stripes with a spacing of double the graphene lattice. **(c)** STM topograph taken on top of a different ∼2.2 Å step at $V_{bias} = 100$ mV and $I_{set} = 50$ pA. **(d)** The same topograph as in (c), but taken at $V_{bias} = 300$ mV. In this case, we observe a graphene (2×2) reconstruction instead.

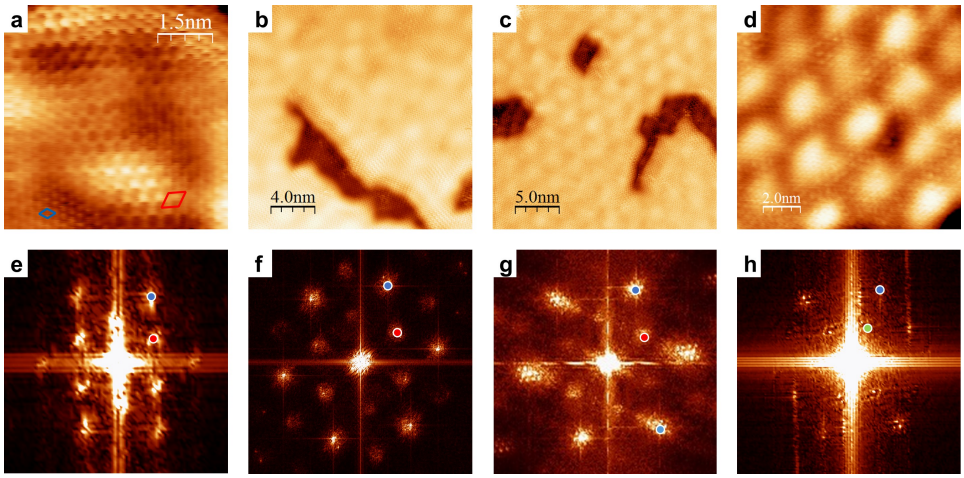

Figure 6.12: Lattice distortion on the intercalated areas. (a) STM topograph taken on top of a ∼2.2 Å step (V_{bias} = 100 mV, I_{set} = 20 pA), showing significant lattice distortions. The graphene lattice is observed in the bottom left corner (unit cell indicated in blue). In the bottom right corner, only the graphene ($\sqrt{3} \times \sqrt{3}$) R30° reconstruction is observed (unit cell indicated in red). **(b–c)** STM topograph taken mostly on a ∼2.2 Å step (V_{bias} = 30 mV for (b), V_{bias} = 100 mV for (c), I_{set} = 2 pA for both), also exhibiting lattice distortions. **(d)** STM topograph taken on top of a ∼2.2 Å step (V_{bias} = 300 mV, I_{set} = 50 pA, same as Figure 6.11(d)). Here the graphene (2 × 2) reconstruction is observed instead. **(e–h)** Fourier transforms of the topography shown in (a–d). All images are cropped to show the same area in frequency space. Graphene (1 × 1) spots are indicated in blue; in (e–g), graphene ($\sqrt{3} \times \sqrt{3}$) R30° spots are indicated in red, while in (h), graphene (2 × 2) spots are indicated in green.

sometimes observed as well (Figure 6.12(d)). These periodicities are particularly clear in the Fourier transforms of the STM images (Figure 6.12(e–d)), where the graphene (1 × 1) spots are indicated in blue, ($\sqrt{3} \times \sqrt{3}$) R30° spots are indicated in red, and (2 × 2) spots are indicated in green. Here we note that the ($\sqrt{3} \times \sqrt{3}$) R30° lattice distortions are distinct from those observed in Chapter 5, which are coherent over the much greater distances required for ARPES and LEED, and also vanish above ∼30 K and do not recover upon subsequent cooling.

6.4 Summary

In this chapter, we observe the formation of islands ∼2.2 Å in height on graphene/SiC samples after mounting the samples using Cu paste and repeated annealing at 600°C due to the appearance of an intercalated layer below the graphene. We observe a change in the graphene/SiC reconstruction periodicity from SiC (6×6) to $(6\sqrt{3} \times 6\sqrt{3})$ R30° on these islands, which we attribute to interactions with the interface and its three inequivalent SiC (6×6) quasi-cells. Such islands are coherent across large portions of the sample surface, such that the $(6\sqrt{3} \times 6\sqrt{3})$ R30° periodicity is clearly observed in LEED. ARPES data indicates a decoupling of the graphene from the substrate, as well as a high coverage of monolayer graphene prior to intercalation.

Through comparison with previous experiments in the literature [166, 167, 171], we attribute these islands to the intercalation of Cu between the graphene and SiC. This intercalation appears to be extremely stable, remaining well-ordered even after years of storage in ambient conditions. These results indicate that Cu can be intercalated in graphene/SiC without the need for evaporation, and the same process may be possible with other metals, thus providing a simple method to produce wafer-scale quasi-free-standing graphene on SiC.

Chapter 7

Conclusions and outlook

In this thesis, we presented a variety of surface characterization tools and techniques, then used them to study graphene on silicon carbide modified via the adsorption and intercalation of foreign atoms. These studies help us to better understand the properties of graphene, and will contribute to its eventual use for electronic applications.

In Chapter 4, we described the testing and characterization of an UHV system capable of offering a number of surface science techniques for parallel characterization of a single sample. Most importantly, we demonstrated the system's ability to perform STM/STS and AFM experiments below 1.2 K in a 3 T magnetic field, as well as ARPES/UPS experiments below 160 K with resolution limited by temperature only.

In Chapter 5, we studied the formation of a CDW phase in graphene due to a very dilute amount of adsorbed lithium. Interactions between the adatoms were mediated by the graphene, resulting in the onset of globally coherent Kekulé bond order and a subsequent $(\sqrt{3}\times\sqrt{3})$ R30° reconstruction. We observed this superstructure using ARPES, through a folding of the Dirac cones from K to Γ, and confirmed it using LEED, through the appearance of new bright spots corresponding to the $(\sqrt{3}\times\sqrt{3})$ R30° periodicity.

By careful analysis of the ARPES data, we also observed a gap opening $2\Delta_{kek} = (238 \pm 3)$ meV at the Dirac point, adding in quadrature with the existing gap due to sublattice symmetry breaking via the SiC substrate. We

observed that the lithium-induced Kekulé phase vanished above ∼30 K, but concluded that this is likely a limit of the lithium stability and not the Kekulé phase itself, since no signatures of the ordering are recovered on subsequent cooling. Additionally, we used a Monte Carlo toy model to demonstrate the importance of deposition conditions in the formation of the Kekulé phase.

Finally, we were able to reproduce the band folding on two other graphene systems, one hole-doped and the other electron-doped up to the VHS, suggesting that this phase is independent of charge carrier type and robust to the absence of nesting conditions.

In Chapter 6, we studied the intercalation of Cu atoms between the graphene and SiC substrate by mounting the sample with Cu paste and subsequent annealing. We observed the appearance of large islands ∼2.2 Å taller than the pristine surface, exhibiting the SiC $(6\sqrt{3} \times 6\sqrt{3})$ R30° reconstruction instead of pristine (6×6). The same periodicity was confirmed using LEED. Using ARPES, we observed a slight closing of the Dirac point gap due to a decoupling of the graphene from the substrate. Additionally, we observed the appearance of an additional Dirac cone whose Dirac point is shifted to −0.86 eV below the Fermi level, which we attributed to the areas of the sample which were covered by the buffer layer prior to intercalation. This provides a simple, accessible method of intercalating metallic atoms under graphene, but care should also be taken to avoid undesired intercalation.

Moving forward, there is a great deal more to be explored in these graphene systems. A major open question is the mechanism behind the Kekulé distortion that allows it to form despite the lack of nesting conditions at E_F. In Chapter 5, we hypothesized that it may be related to electron-phonon coupling. However, a more detailed study of the graphene phonon modes—possibly via high-resolution and/or time-resolved ARPES experiments—is needed to shed further light in this direction.

Another possible extension of the Kekulé graphene work is probing its dynamics using time-resolved ARPES experiments. In particular, a transient "melting" of the CDW phase can be driven and studied via pump-probe spectroscopy [175, 176].

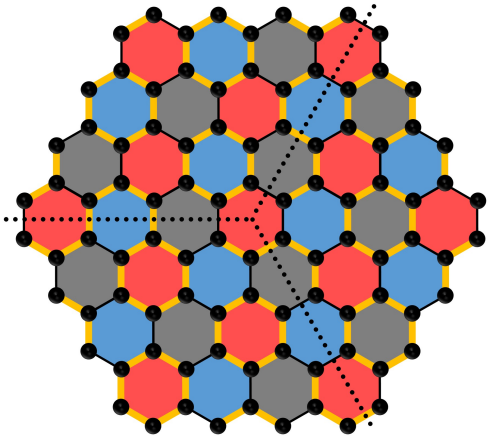

Figure 7.1: A junction between three Kekulé "colours." A graphene flake is RGB colour-coded as in Chapter 5. In each third of the flake, the distorted bonds (thick yellow lines) reside on a different colour lattice. Such a junction can be built using atom manipulation techniques, and is believed to host a vortex state [177]. Adapted from [177].

Aside from the temporal domain, the local characteristics of such a Kekulé phase can be probed using SPM techniques. In particular, the effects associated with a single adatom can be studied via atom manipulation. Specific local structures of the Kekulé distortion can also be constructed and studied: the junction between the three different "colours" of the Kekulé pattern (Figure 7.1) is particularly interesting, as it has been theorized to host a vortex state [177]. Such SPM experiments, however, have proven to be challenging due to the weak bond between the lithium and the graphene surface, which is easily disrupted by interactions with the tip. Using a different adsorbate which bonds more strongly to the graphene may produce better results.

Despite graphene's multitude of remarkable properties, its use is not yet widespread. Some of the reasons for this—such as the lack of wafer-sized samples—have been addressed since graphene was first realized in 2004. Others, such as the lack of a band gap in pristine graphene for use in semiconducting devices, are still being investigated by physicists and

engineers. In this thesis, we studied two methods of modifying graphene on large length scales: one using just a small number of adsorbed atoms interacting over large distances, and the other stable for years in ambient conditions. Such simple, robust new phases in graphene grown on a wafer-sized, insulating substrate offer great promise for graphene to one day become commonplace in our electronic devices.

Bibliography

[1] K. S. Novoselov, A. K. Geim, S. V. Morozov, D. Jiang, Y. Zhang, S. V. Dubonos, I. V. Grigorieva, and A. A. Firsov. Electric Field Effect in Atomically Thin Carbon Films. *Science*, 306(5696):666–669, Oct. 2004. ISSN 0036-8075, 1095-9203. doi:10.1126/science.1102896. → pages 1, 4

[2] P. R. Wallace. The Band Theory of Graphite. *Physical Review*, 71(9): 622–634, May 1947. doi:10.1103/PhysRev.71.622. → pages 1, 3

[3] J. W. McClure. Diamagnetism of Graphite. *Physical Review*, 104(3): 666–671, Nov. 1956. doi:10.1103/PhysRev.104.666. → page 1

[4] J. C. Slonczewski and P. R. Weiss. Band Structure of Graphite. *Physical Review*, 109(2):272–279, Jan. 1958. doi:10.1103/PhysRev.109.272. → page 1

[5] G. W. Semenoff. Condensed-Matter Simulation of a Three-Dimensional Anomaly. *Physical Review Letters*, 53(26): 2449–2452, Dec. 1984. doi:10.1103/PhysRevLett.53.2449. → pages 1, 3

[6] F. D. M. Haldane. Model for a Quantum Hall Effect without Landau Levels: Condensed-Matter Realization of the "Parity Anomaly". *Physical Review Letters*, 61(18):2015–2018, Oct. 1988. doi:10.1103/PhysRevLett.61.2015. → page 1

[7] R. E. Peierls. Quelques propriétés typiques des corps solides. *Ann. I. H. Poincare*, 5:177–222, 1935. → page 1

[8] L. D. Landau. Zur Theorie der phasenumwandlungen II. *Phys. Z. Sowjetunion*, 11:26–35, 1937. → page 1

[9] L. D. Landau and E. M. Lifshitz. *Statistical Physics, Part I.* Pergamon, Oxford, 1980. → page 1

[10] N. D. Mermin. Crystalline order in two dimensions. *Physical Review*, 176:250–254, 1968. → page 1

[11] H. P. Boehm, A. Clauss, G. O. Fischer, and U. Hofmann. Das Adsorptionsverhalten sehr dünner Kohlenstoff-Folien. *Zeitschrift für anorganische und allgemeine Chemie*, 316(3-4):119–127, 1962. ISSN 1521-3749. doi:10.1002/zaac.19623160303. → page 1

[12] H. Shioyama. Cleavage of graphite to graphene. *Journal of Materials Science Letters*, 20(6):499–500, Mar. 2001. ISSN 1573-4811. doi:10.1023/A:1010907928709. → page 1

[13] L. M. Viculis, J. J. Mack, and R. B. Kaner. A Chemical Route to Carbon Nanoscrolls. *Science*, 299(5611):1361–1361, Feb. 2003. ISSN 0036-8075, 1095-9203. doi:10.1126/science.1078842. → page 1

[14] S. Horiuchi, T. Gotou, M. Fujiwara, T. Asaka, T. Yokosawa, and Y. Matsui. Single graphene sheet detected in a carbon nanofilm. *Applied Physics Letters*, 84(13):2403–2405, Mar. 2004. ISSN 0003-6951. doi:10.1063/1.1689746. → page 1

[15] A. K. Geim and K. S. Novoselov. The rise of graphene. *Nature Materials*, 6(3):183–191, Mar. 2007. ISSN 1476-4660. doi:10.1038/nmat1849. → page 1

[16] A. K. Geim. Graphene: Status and Prospects. *Science*, 324(5934): 1530–1534, June 2009. ISSN 0036-8075, 1095-9203. doi:10.1126/science.1158877. → page 1

[17] A. K. Geim. Graphene prehistory. *Physica Scripta*, T146:014003, Jan. 2012. ISSN 1402-4896. doi:10.1088/0031-8949/2012/T146/014003. → page 1

[18] A. H. Castro Neto, F. Guinea, N. M. R. Peres, K. S. Novoselov, and A. K. Geim. The electronic properties of graphene. *Reviews of Modern Physics*, 81(1):109–162, Jan. 2009. doi:10.1103/RevModPhys.81.109. → pages 1, 3, 11, 15

[19] M. J. Allen, V. C. Tung, and R. B. Kaner. Honeycomb Carbon: A Review of Graphene. *Chemical Reviews*, 110(1):132–145, Jan. 2010. ISSN 0009-2665. doi:10.1021/cr900070d. → page 1

[20] Y. Zhang, Y.-W. Tan, H. L. Stormer, and P. Kim. Experimental observation of the quantum Hall effect and Berry's phase in graphene. *Nature*, 438(7065):201–204, Nov. 2005. ISSN 1476-4687. doi:10.1038/nature04235. → pages 3, 4

[21] K. S. Novoselov, A. K. Geim, S. V. Morozov, D. Jiang, M. I. Katsnelson, I. V. Grigorieva, S. V. Dubonos, and A. A. Firsov. Two-dimensional gas of massless Dirac fermions in graphene. *Nature*, 438(7065):197–200, Nov. 2005. ISSN 1476-4687. doi:10.1038/nature04233. → pages 3, 4

[22] K. von Klitzing, G. Dorda, and M. Pepper. New Method for High-Accuracy Determination of the Fine-Structure Constant Based on Quantized Hall Resistance. *Physical Review Letters*, 45(6):494–497, Aug. 1980. doi:10.1103/PhysRevLett.45.494. → page 3

[23] C. Lee, X. Wei, J. W. Kysar, and J. Hone. Measurement of the Elastic Properties and Intrinsic Strength of Monolayer Graphene. *Science*, 321(5887):385–388, July 2008. ISSN 0036-8075, 1095-9203. doi:10.1126/science.1157996. → page 4

[24] V. M. Pereira, A. H. Castro Neto, and N. M. R. Peres. Tight-binding approach to uniaxial strain in graphene. *Physical Review B*, 80(4): 045401, July 2009. doi:10.1103/PhysRevB.80.045401. → page 4

[25] A. A. Balandin, S. Ghosh, W. Bao, I. Calizo, D. Teweldebrhan, F. Miao, and C. N. Lau. Superior Thermal Conductivity of Single-Layer Graphene. *Nano Letters*, 8(3):902–907, Mar. 2008. ISSN 1530-6984, 1530-6992. doi:10.1021/nl0731872. → page 4

[26] A. J. Van Bommel, J. E. Crombeen, and A. Van Tooren. LEED and Auger electron observations of the SiC(0001) surface. *Surface Science*, 48(2):463–472, Mar. 1975. ISSN 0039-6028. doi:10.1016/0039-6028(75)90419-7. → page 4

[27] C. Berger, Z. Song, T. Li, X. Li, A. Y. Ogbazghi, R. Feng, Z. Dai, A. N. Marchenkov, E. H. Conrad, P. N. First, and W. A. de Heer. Ultrathin Epitaxial Graphite: 2D Electron Gas Properties and a Route toward Graphene-based Nanoelectronics. *The Journal of Physical Chemistry B*, 108(52):19912–19916, Dec. 2004. ISSN 1520-6106. doi:10.1021/jp040650f. → page 4

[28] C. Berger, Z. Song, X. Li, X. Wu, N. Brown, C. Naud, D. Mayou, T. Li, J. Hass, A. N. Marchenkov, E. H. Conrad, P. N. First, and W. A. de Heer. Electronic Confinement and Coherence in Patterned Epitaxial Graphene. *Science*, 312(5777):1191–1196, May 2006. ISSN 0036-8075, 1095-9203. doi:10.1126/science.1125925. → page 4

[29] C. Riedl, U. Starke, J. Bernhardt, M. Franke, and K. Heinz. Structural properties of the graphene-SiC(0001) interface as a key for the preparation of homogeneous large-terrace graphene surfaces. *Physical Review B*, 76(24):245406, Dec. 2007. doi:10.1103/PhysRevB.76.245406. → pages 4, 82, 109, 110, 111

[30] F. Guinea, M. I. Katsnelson, and A. K. Geim. Energy gaps and a zero-field quantum Hall effect in graphene by strain engineering. *Nature Physics*, 6(1):30–33, Jan. 2010. ISSN 1745-2481. doi:10.1038/nphys1420. → pages 5, 6

[31] Y. Cao, V. Fatemi, A. Demir, S. Fang, S. L. Tomarken, J. Y. Luo, J. D. Sanchez-Yamagishi, K. Watanabe, T. Taniguchi, E. Kaxiras, R. C. Ashoori, and P. Jarillo-Herrero. Correlated insulator behaviour at half-filling in magic-angle graphene superlattices. *Nature*, 556 (7699):80–84, Apr. 2018. ISSN 1476-4687. doi:10.1038/nature26154. URL https://www.nature.com/articles/nature26154. → page 6

[32] H. Chen, X.-L. Zhang, Y.-Y. Zhang, D. Wang, D.-L. Bao, Y. Que, W. Xiao, S. Du, M. Ouyang, S. T. Pantelides, and H.-J. Gao. Atomically precise, custom-design origami graphene nanostructures. *Science*, 365(6457):1036–1040, Sept. 2019. ISSN 0036-8075, 1095-9203. doi:10.1126/science.aax7864. → page 6

[33] C. L. Kane and E. J. Mele. Size, Shape, and Low Energy Electronic Structure of Carbon Nanotubes. *Physical Review Letters*, 78(10): 1932–1935, Mar. 1997. doi:10.1103/PhysRevLett.78.1932. → page 6

[34] N. Levy, S. A. Burke, K. L. Meaker, M. Panlasigui, A. Zettl, F. Guinea, A. H. C. Neto, and M. F. Crommie. Strain-Induced Pseudo–Magnetic Fields Greater Than 300 Tesla in Graphene Nanobubbles. *Science*, 329(5991):544–547, July 2010. ISSN 0036-8075, 1095-9203. doi:10.1126/science.1191700. → page 6

[35] P. Nigge, A. C. Qu, É. Lantagne-Hurtubise, E. Mårsell, S. Link, G. Tom, M. Zonno, M. Michiardi, M. Schneider, S. Zhdanovich,

G. Levy, U. Starke, C. Gutiérrez, D. Bonn, S. A. Burke, M. Franz, and A. Damascelli. Room temperature strain-induced Landau levels in graphene on a wafer-scale platform. *Science Advances*, 5(11): eaaw5593, Nov. 2019. ISSN 2375-2548. doi:10.1126/sciadv.aaw5593. → pages 6, 91, 92

[36] K. K. Gomes, W. Mar, W. Ko, F. Guinea, and H. C. Manoharan. Designer Dirac fermions and topological phases in molecular graphene. *Nature*, 483(7389):306–310, Mar. 2012. ISSN 1476-4687. doi:10.1038/nature10941. → page 6

[37] M. C. Rechtsman, J. M. Zeuner, A. Tünnermann, S. Nolte, M. Segev, and A. Szameit. Strain-induced pseudomagnetic field and photonic Landau levels in dielectric structures. *Nature Photonics*, 7(2):153–158, Feb. 2013. ISSN 1749-4893. doi:10.1038/nphoton.2012.302. → page 6

[38] A. Ramasubramaniam, D. Naveh, and E. Towe. Tunable Band Gaps in Bilayer Graphene-BN Heterostructures. *Nano Letters*, 11(3): 1070–1075, Mar. 2011. ISSN 1530-6984. doi:10.1021/nl1039499. → pages 6, 17

[39] J. Jung, A. M. DaSilva, A. H. MacDonald, and S. Adam. Origin of band gaps in graphene on hexagonal boron nitride. *Nature Communications*, 6(1):6308, Feb. 2015. ISSN 2041-1723. doi:10.1038/ncomms7308. → pages 6, 17

[40] S. Kim, J. Ihm, H. J. Choi, and Y.-W. Son. Origin of Anomalous Electronic Structures of Epitaxial Graphene on Silicon Carbide. *Physical Review Letters*, 100(17):176802, Apr. 2008. doi:10.1103/PhysRevLett.100.176802. → page 6

[41] S. Y. Zhou, G.-H. Gweon, A. V. Fedorov, P. N. First, W. A. de Heer, D.-H. Lee, F. Guinea, A. H. Castro Neto, and A. Lanzara. Substrate-induced bandgap opening in epitaxial graphene. *Nature Materials*, 6(10):770–775, Oct. 2007. ISSN 1476-4660. doi:10.1038/nmat2003. → pages 6, 17, 83, 91, 92

[42] M. Weinberg, C. Staarmann, C. Ölschläger, J. Simonet, and K. Sengstock. Breaking inversion symmetry in a state-dependent honeycomb lattice: Artificial graphene with tunable band gap. *2D Materials*, 3(2):024005, Apr. 2016. ISSN 2053-1583. doi:10.1088/2053-1583/3/2/024005. → pages 6, 17

[43] Y. Yao, F. Ye, X.-L. Qi, S.-C. Zhang, and Z. Fang. Spin-orbit gap of graphene: First-principles calculations. *Physical Review B*, 75(4): 041401, Jan. 2007. doi:10.1103/PhysRevB.75.041401. → page 7

[44] A. Avsar, J. Y. Tan, T. Taychatanapat, J. Balakrishnan, G. K. W. Koon, Y. Yeo, J. Lahiri, A. Carvalho, A. S. Rodin, E. C. T. O'Farrell, G. Eda, A. H. Castro Neto, and B. Özyilmaz. Spin–orbit proximity effect in graphene. *Nature Communications*, 5(1):4875, Sept. 2014. ISSN 2041-1723. doi:10.1038/ncomms5875. → page 7

[45] H. X. Yang, A. Hallal, D. Terrade, X. Waintal, S. Roche, and M. Chshiev. Proximity Effects Induced in Graphene by Magnetic Insulators: First-Principles Calculations on Spin Filtering and Exchange-Splitting Gaps. *Physical Review Letters*, 110(4):046603, Jan. 2013. doi:10.1103/PhysRevLett.110.046603. → page 7

[46] M. V. Feigel'man, M. A. Skvortsov, and K. S. Tikhonov. Proximity-induced superconductivity in graphene. *JETP Letters*, 88 (11):747–751, Feb. 2008. ISSN 0021-3640, 1090-6487. doi:10.1134/S0021364008230100. → page 7

[47] H. B. Heersche, P. Jarillo-Herrero, J. B. Oostinga, L. M. K. Vandersypen, and A. F. Morpurgo. Induced superconductivity in graphene. *Solid State Communications*, 143(1):72–76, July 2007. ISSN 0038-1098. doi:10.1016/j.ssc.2007.02.044. → page 7

[48] M. Ben Shalom, M. J. Zhu, V. I. Fal'ko, A. Mishchenko, A. V. Kretinin, K. S. Novoselov, C. R. Woods, K. Watanabe, T. Taniguchi, A. K. Geim, and J. R. Prance. Quantum oscillations of the critical current and high-field superconducting proximity in ballistic graphene. *Nature Physics*, 12(4):318–322, Apr. 2016. ISSN 1745-2481. doi:10.1038/nphys3592. → page 7

[49] C. Ojeda-Aristizabal, M. Ferrier, S. Guéron, and H. Bouchiat. Tuning the proximity effect in a superconductor-graphene-superconductor junction. *Physical Review B*, 79(16):165436, Apr. 2009. doi:10.1103/PhysRevB.79.165436. → page 7

[50] A. Shailos, W. Nativel, A. Kasumov, C. Collet, M. Ferrier, S. Guéron, R. Deblock, and H. Bouchiat. Proximity effect and multiple Andreev reflections in few-layer graphene. *Europhysics Letters (EPL)*, 79(5): 57008, Aug. 2007. ISSN 0295-5075. doi:10.1209/0295-5075/79/57008. → page 7

[51] C. Gutiérrez, C.-J. Kim, L. Brown, T. Schiros, D. Nordlund, E. B. Lochocki, K. M. Shen, J. Park, and A. N. Pasupathy. Imaging chiral symmetry breaking from Kekulé bond order in graphene. *Nature Physics*, 12(10):950–958, Oct. 2016. ISSN 1745-2481. doi:10.1038/nphys3776. → pages 7, 80, 81, 82, 89, 97

[52] C. Riedl, C. Coletti, T. Iwasaki, A. A. Zakharov, and U. Starke. Quasi-Free-Standing Epitaxial Graphene on SiC Obtained by Hydrogen Intercalation. *Physical Review Letters*, 103(24):246804, Dec. 2009. doi:10.1103/PhysRevLett.103.246804. → pages 7, 51, 98, 109, 110, 111

[53] B. M. Ludbrook, G. Levy, P. Nigge, M. Zonno, M. Schneider, D. J. Dvorak, C. N. Veenstra, S. Zhdanovich, D. Wong, P. Dosanjh, C. Straßer, A. Stöhr, S. Forti, C. R. Ast, U. Starke, and A. Damascelli. Evidence for superconductivity in Li-decorated monolayer graphene. *Proceedings of the National Academy of Sciences*, 112(38): 11795–11799, Sept. 2015. ISSN 0027-8424, 1091-6490. doi:10.1073/pnas.1510435112. → pages 7, 8, 89

[54] C. Virojanadara, A. A. Zakharov, S. Watcharinyanon, R. Yakimova, and L. I. Johansson. A low-energy electron microscopy and x-ray photo-emission electron microscopy study of Li intercalated into graphene on SiC(0001). *New Journal of Physics*, 12(12):125015, Dec. 2010. ISSN 1367-2630. doi:10.1088/1367-2630/12/12/125015. → page 7

[55] F. Bisti, G. Profeta, H. Vita, M. Donarelli, F. Perrozzi, P. M. Sheverdyaeva, P. Moras, K. Horn, and L. Ottaviano. Electronic and geometric structure of graphene/SiC(0001) decoupled by lithium intercalation. *Physical Review B*, 91(24):245411, June 2015. doi:10.1103/PhysRevB.91.245411. → page 7

[56] R. Nandkishore, L. S. Levitov, and A. V. Chubukov. Chiral superconductivity from repulsive interactions in doped graphene. *Nature Physics*, 8(2):158–163, Feb. 2012. ISSN 1745-2473, 1745-2481. doi:10.1038/nphys2208. → page 7

[57] M. L. Kiesel, C. Platt, W. Hanke, D. A. Abanin, and R. Thomale. Competing many-body instabilities and unconventional superconductivity in graphene. *Physical Review B*, 86(2):020507, July 2012. doi:10.1103/PhysRevB.86.020507. → page 7

[58] A. M. Black-Schaffer and C. Honerkamp. Chiral d-wave superconductivity in doped graphene. *Journal of Physics: Condensed Matter*, 26(42):423201, Sept. 2014. ISSN 0953-8984. doi:10.1088/0953-8984/26/42/423201. → page 7

[59] D. Makogon, R. van Gelderen, R. Roldán, and C. M. Smith. Spin-density-wave instability in graphene doped near the van Hove singularity. *Physical Review B*, 84(12):125404, Sept. 2011. doi:10.1103/PhysRevB.84.125404. → page 7

[60] S. Link, S. Forti, A. Stöhr, K. Küster, M. Rösner, D. Hirschmeier, C. Chen, J. Avila, M. C. Asensio, A. A. Zakharov, T. O. Wehling, A. I. Lichtenstein, M. I. Katsnelson, and U. Starke. Introducing strong correlation effects into graphene by gadolinium intercalation. *Physical Review B*, 100(12):121407, Sept. 2019. doi:10.1103/PhysRevB.100.121407. → pages 7, 51, 98, 110

[61] P. Rosenzweig, H. Karakachian, S. Link, K. Küster, and U. Starke. Tuning the doping level of graphene in the vicinity of the Van Hove singularity via ytterbium intercalation. *Physical Review B*, 100(3): 035445, July 2019. ISSN 2469-9950, 2469-9969. doi:10.1103/PhysRevB.100.035445. → page 7

[62] P. Rosenzweig, H. Karakachian, D. Marchenko, K. Küster, and U. Starke. Overdoping Graphene Beyond the van Hove Singularity. *Physical Review Letters*, 125(17):176403, Oct. 2020. ISSN 0031-9007, 1079-7114. doi:10.1103/PhysRevLett.125.176403. → page 7

[63] J. L. McChesney, A. Bostwick, T. Ohta, T. Seyller, K. Horn, J. González, and E. Rotenberg. Extended van Hove Singularity and Superconducting Instability in Doped Graphene. *Physical Review Letters*, 104(13):136803, Apr. 2010. ISSN 0031-9007, 1079-7114. doi:10.1103/PhysRevLett.104.136803. → page 7

[64] G. Profeta, M. Calandra, and F. Mauri. Phonon-mediated superconductivity in graphene by lithium deposition. *Nature Physics*, 8(2):131–134, jan 2012. doi:10.1038/nphys2181. → page 8

[65] S. Ichinokura, K. Sugawara, A. Takayama, T. Takahashi, and S. Hasegawa. Superconducting Calcium-Intercalated Bilayer Graphene. *ACS Nano*, 10(2):2761–2765, Feb. 2016. ISSN 1936-0851. doi:10.1021/acsnano.5b07848. → pages 8, 110

[66] K. Kanetani, K. Sugawara, T. Sato, R. Shimizu, K. Iwaya, T. Hitosugi, and T. Takahashi. Ca intercalated bilayer graphene as a thinnest limit of superconducting C6Ca. *Proceedings of the National Academy of Sciences*, 109(48):19610–19613, Nov. 2012. ISSN 0027-8424, 1091-6490. doi:10.1073/pnas.1208889109. → pages 8, 110

[67] R. Balog, B. Jørgensen, L. Nilsson, M. Andersen, E. Rienks, M. Bianchi, M. Fanetti, E. Lægsgaard, A. Baraldi, S. Lizzit, Z. Sljivancanin, F. Besenbacher, B. Hammer, T. G. Pedersen, P. Hofmann, and L. Hornekær. Bandgap opening in graphene induced by patterned hydrogen adsorption. *Nature Materials*, 9(4):315–319, Apr. 2010. ISSN 1476-4660. doi:10.1038/nmat2710. → page 8

[68] J. H. Jørgensen, A. G. Čabo, R. Balog, L. Kyhl, M. N. Groves, A. M. Cassidy, A. Bruix, M. Bianchi, M. Dendzik, M. A. Arman, L. Lammich, J. I. Pascual, J. Knudsen, B. Hammer, P. Hofmann, and L. Hornekaer. Symmetry-Driven Band Gap Engineering in Hydrogen Functionalized Graphene. *ACS Nano*, 10(12):10798–10807, Dec. 2016. ISSN 1936-0851, 1936-086X. doi:10.1021/acsnano.6b04671. → page 8

[69] C. Weeks, J. Hu, J. Alicea, M. Franz, and R. Wu. Engineering a Robust Quantum Spin Hall State in Graphene via Adatom Deposition. *Physical Review X*, 1(2):021001, Oct. 2011. doi:10.1103/PhysRevX.1.021001. → page 8

[70] C. Straßer, B. M. Ludbrook, G. Levy, A. J. Macdonald, S. A. Burke, T. O. Wehling, K. Kern, A. Damascelli, and C. R. Ast. Long- versus Short-Range Scattering in Doped Epitaxial Graphene. *Nano Letters*, 15(5):2825–2829, May 2015. ISSN 1530-6984, 1530-6992. doi:10.1021/nl504155f. → page 8

[71] Z. Jia, B. Yan, J. Niu, Q. Han, R. Zhu, D. Yu, and X. Wu. Transport study of graphene adsorbed with indium adatoms. *Physical Review B*, 91(8):085411, Feb. 2015. doi:10.1103/PhysRevB.91.085411. → page 8

[72] F. Utermohlen. Tight-Binding Model for Graphene, 2018. → page 9

[73] M. Franz. PHYS 502: Condensed Matter Physics I, 2015. → page 9

[74] M. Franz. PHYS 525B: Advanced Condensed Matter Physics, 2017. → page 9

[75] L.-H. Wu and X. Hu. Topological Properties of Electrons in Honeycomb Lattice with Detuned Hopping Energy. *Scientific Reports*, 6(1):24347, Apr. 2016. ISSN 2045-2322. doi:10.1038/srep24347. → page 21

[76] A. J. Heeger, S. Kivelson, J. R. Schrieffer, and W. P. Su. Solitons in conducting polymers. *Reviews of Modern Physics*, 60(3):781–850, July 1988. ISSN 0034-6861. doi:10.1103/RevModPhys.60.781. → page 21

[77] H. Hertz. Ueber einen Einfluss des ultravioletten Lichtes auf die electrische Entladung. *Annalen der Physik*, 267(8):983–1000, 1887. ISSN 1521-3889. doi:10.1002/andp.18872670827. → page 23

[78] A. Einstein. Ueber einen die Erzeugung und Verwandlung des Lichtes betreffenden heuristischen Gesichtspunkt. *Annalen der Physik*, 322(6): 132–148, 1905. ISSN 1521-3889. doi:10.1002/andp.19053220607. → page 23

[79] S. Hüfner. *Photoelectron Spectroscopy*. Springer-Verlag Berlin Heidelberg, 2003. → pages 23, 24, 26, 28, 30, 41

[80] S. Hüfner. *Very High Resolution Photoelectron Spectroscopy*. Springer-Verlag Berlin Heidelberg, 2007. → page 23

[81] A. Damascelli, Z. Hussain, and Z.-X. Shen. Angle-resolved photoemission studies of the cuprate superconductors. *Reviews of Modern Physics*, 75(2):473–541, Apr. 2003. doi:10.1103/RevModPhys.75.473. → page 23

[82] A. Damascelli. Probing the Electronic Structure of Complex Systems by ARPES. *Physica Scripta*, 2004(T109):61, Jan. 2004. ISSN 1402-4896. doi:10.1238/Physica.Topical.109a00061. → pages 23, 24, 25, 26, 28

[83] M. Cardona and L. Ley. *Photoemission in Solids I: General Principles*. Springer-Verlag Berlin Heidelberg, 1978. → page 23

[84] M. Cardona and L. Ley. *Photoemission in Solids II: Case Studies*. Springer-Verlag Berlin Heidelberg, 1979. → page 23

[85] B. Feuerbacher, B. Fitton, and R. F. Willis. *Photoemission and the Electronic Properties of Surfaces*. John Wiley & Sons, 1978. → page 23

[86] S. D. Kevan. *Angle-Resolved Photoemission: Theory and Current Applications*. Elsevier Science, 1992. → page 23

[87] G. D. Mahan. Theory of Photoemission. In *Electron and Ion Spectroscopy of Solids*. Springer-Verlag, 1978. → page 23

[88] C. N. Berglund and W. E. Spicer. Photoemission Studies of Copper and Silver: Theory. *Physical Review*, 136(4A):A1030–A1044, Nov. 1964. doi:10.1103/PhysRev.136.A1030. → page 26

[89] A. A. Abrikosov, L. P. Gorkov, and I. E. Dzyaloshinski. *Methods of Quantum Field Theory in Statistical Physics*. Dover, 1975. → page 28

[90] A. Fetter and J. D. Walecka. *Quantum Theory of Many-Particle Systems*. Dover, 2003. → page 28

[91] G. D. Mahan. *Many-Particle Physics*. Springer US, 2000. → page 28

[92] E. N. Economou. *Green's Functions in Quantum Physics*. Springer, 2006. → page 28

[93] G. Rickayzen. *Green's Functions and Condensed Matter*. Dover, 2013. → page 28

[94] I. Vishik. Angle-resolved photoemission spectroscopy (ARPES) overview, 2018. → page 28

[95] B. Wannberg. Electron optics development for photo-electron spectrometers. *Nuclear Instruments and Methods in Physics Research Section A: Accelerators, Spectrometers, Detectors and Associated Equipment*, 601(1):182–194, Mar. 2009. ISSN 0168-9002. doi:10.1016/j.nima.2008.12.156. → page 29

[96] G. Binnig, H. Rohrer, C. Gerber, and E. Weibel. Surface Studies by Scanning Tunneling Microscopy. *Physical Review Letters*, 49(1):57–61, July 1982. doi:10.1103/PhysRevLett.49.57. → page 32

[97] G. Binnig and H. Rohrer. Scanning tunneling microscopy. *Surface Science*, 126(1):236–244, Mar. 1983. ISSN 0039-6028. doi:10.1016/0039-6028(83)90716-1. → page 32

[98] G. Binnig, C. F. Quate, and C. Gerber. Atomic Force Microscope. *Physical Review Letters*, 56(9):930–933, Mar. 1986. doi:10.1103/PhysRevLett.56.930. → pages 32, 38

[99] J. E. Hoffman. Spectroscopic scanning tunneling microscopy insights into Fe-based superconductors. *Reports on Progress in Physics*, 74(12): 124513, Nov. 2011. ISSN 0034-4885. doi:10.1088/0034-4885/74/12/124513. → page 32

[100] S. Lounis. Theory of Scanning Tunneling Microscopy. *arXiv:1404.0961 [cond-mat]*, Apr. 2014. → page 33

[101] J. Bardeen. Tunnelling from a Many-Particle Point of View. *Physical Review Letters*, 6(2):57–59, Jan. 1961. doi:10.1103/PhysRevLett.6.57. → pages 33, 35

[102] J. Tersoff and D. R. Hamann. Theory and Application for the Scanning Tunneling Microscope. *Physical Review Letters*, 50(25): 1998–2001, June 1983. doi:10.1103/PhysRevLett.50.1998. → page 33

[103] J. Tersoff and D. R. Hamann. Theory of the scanning tunneling microscope. *Physical Review B*, 31(2):805–813, Jan. 1985. doi:10.1103/PhysRevB.31.805. → page 33

[104] C. J. Chen. Tunneling matrix elements in three-dimensional space: The derivative rule and the sum rule. *Physical Review B*, 42(14): 8841–8857, Nov. 1990. doi:10.1103/PhysRevB.42.8841. → page 33

[105] C. J. Chen. Origin of atomic resolution on metal surfaces in scanning tunneling microscopy. *Physical Review Letters*, 65(4):448–451, July 1990. doi:10.1103/PhysRevLett.65.448. → page 33

[106] C. J. Chen. *Introduction to Scanning Tunneling Microscopy*. Oxford University Press, 1993. → page 33

[107] Y. Zhang, V. W. Brar, F. Wang, C. Girit, Y. Yayon, M. Panlasigui, A. Zettl, and M. F. Crommie. Giant phonon-induced conductance in scanning tunnelling spectroscopy of gate-tunable graphene. *Nature Physics*, 4(8):627–630, Aug. 2008. ISSN 1745-2481. doi:10.1038/nphys1022. → page 38

[108] T. O. Wehling, I. Grigorenko, A. I. Lichtenstein, and A. V. Balatsky. Phonon mediated tunneling into graphene. *Physical Review Letters*, 101(21):216803, Nov. 2008. ISSN 0031-9007, 1079-7114. doi:10.1103/PhysRevLett.101.216803. → page 38

[109] Y. Zhang, V. W. Brar, C. Girit, A. Zettl, and M. F. Crommie. Origin of spatial charge inhomogeneity in graphene. *Nature Physics*, 5(10): 722–726, Oct. 2009. ISSN 1745-2481. doi:10.1038/nphys1365. → page 38

[110] M. F. Crommie, C. P. Lutz, and D. M. Eigler. Imaging standing waves in a two-dimensional electron gas. *Nature*, 363(6429):524–527, June 1993. ISSN 1476-4687. doi:10.1038/363524a0. → page 38

[111] Y. Hasegawa and P. Avouris. Direct observation of standing wave formation at surface steps using scanning tunneling spectroscopy. *Physical Review Letters*, 71(7):1071–1074, Aug. 1993. doi:10.1103/PhysRevLett.71.1071. → page 38

[112] S. Morita, R. Wiesendanger, and E. Meyer. *Noncontact Atomic Force Microscopy*. Springer-Verlag Berlin Heidelberg, 2002. → page 39

[113] U. Dürig, H. R. Steinauer, and N. Blanc. Dynamic force microscopy by means of the phase-controlled oscillator method. *Journal of Applied Physics*, 82(8):3641–3651, Oct. 1997. ISSN 0021-8979. doi:10.1063/1.365726. → page 39

[114] K. Oura, V. G. Lifshits, A. A. Saranin, A. V. Zotov, and M. Katayama. *Surface Science*. Springer-Verlag Berlin Heidelberg, 2003. → page 40

[115] M. A. Van Hove, W. H. Weinberg, and C. M. Chan. *Low-Energy Electron Diffraction*. Springer-Verlag, 1986. → page 40

[116] N. W. Ashcroft and N. D. Mermin. *Solid State Physics*. Harcourt College Publishers, 1976. → pages 40, 41

[117] Ponor. File:Low-energy electron diffraction (LEED) instrument - schematic diagram.svg. *Wikipedia*, 2020. → page 41

[118] D. V. Schroeder. *An Introduction to Thermal Physics*. Addison Wesley Longman, 2000. → pages 46, 62

[119] S. Forti, K. V. Emtsev, C. Coletti, A. A. Zakharov, C. Riedl, and U. Starke. Large-area homogeneous quasifree standing epitaxial graphene on SiC(0001): Electronic and structural characterization. *Physical Review B*, 84(12):125449, Sept. 2011. doi:10.1103/PhysRevB.84.125449. → pages 49, 109

[120] S. Forti and U. Starke. Epitaxial graphene on SiC: From carrier density engineering to quasi-free standing graphene by atomic intercalation. *Journal of Physics D: Applied Physics*, 47(9):094013, Feb. 2014. ISSN 0022-3727. doi:10.1088/0022-3727/47/9/094013. → pages 49, 82, 83, 109, 110

[121] M. Kara, H. Sasabe, and W. Knoll. Ordered nucleation of a self-assembled monolayer on Au(111) studied by scanning tunneling microscopy. *Thin Solid Films*, 273(1):66–69, Feb. 1996. ISSN 0040-6090. doi:10.1016/0040-6090(95)06995-X. → page 51

[122] H. Pan, B. Tong, J. Yu, J. Wang, D. Fu, S. Zhang, B. Wu, X. Wan, C. Zhang, X. Wang, and F. Song. Three-Dimensional Anisotropic Magnetoresistance in the Dirac Node-Line Material ZrSiSe. *Scientific Reports*, 8(1):9340, June 2018. ISSN 2045-2322. doi:10.1038/s41598-018-27148-z. → page 53

[123] Focus GmbH. VUV Source HIS 13 / HIS 14 HD and HIS Mono Instruction Manual, 2018. → pages 59, 62

[124] Scienta Omicron AB. Scienta Omicron R3000 Instrument Manual, 2018. → pages 59, 69, 70

[125] G. Panaccione, G. Cautero, M. Cautero, A. Fondacaro, M. Grioni, P. Lacovig, G. Monaco, F. Offi, G. Paolicelli, M. Sacchi, N. Stojić, G. Stefani, R. Tommasini, and P. Torelli. High-energy photoemission in silver: Resolving d and sp contributions in valence band spectra. *Journal of Physics: Condensed Matter*, 17(17):2671–2679, Apr. 2005. ISSN 0953-8984. doi:10.1088/0953-8984/17/17/015. → page 59

[126] D. Wang, X. Cui, Q. Xiao, Y. Hu, Z. Wang, Y. M. Yiu, and T. K. Sham. Electronic behaviour of Au-Pt alloys and the 4f binding energy shift anomaly in Au bimetallics- X-ray spectroscopy studies. *AIP Advances*, 8(6):065210, June 2018. doi:10.1063/1.5027251. → page 62

[127] S. D. Kevan and R. H. Gaylord. High-resolution photoemission study of the electronic structure of the noble-metal (111) surfaces. *Physical Review B*, 36(11):5809–5818, Oct. 1987. doi:10.1103/PhysRevB.36.5809. → page 71

[128] M. M. Hosen, K. Dimitri, I. Belopolski, P. Maldonado, R. Sankar, N. Dhakal, G. Dhakal, T. Cole, P. M. Oppeneer, D. Kaczorowski, F. Chou, M. Z. Hasan, T. Durakiewicz, and M. Neupane. Tunability

of the topological nodal-line semimetal phase in ZrSiX-type materials (X=S, Se, Te). *Physical Review B*, 95(16):161101, Apr. 2017. doi:10.1103/PhysRevB.95.161101. → page 72

[129] M. P. Everson, L. C. Davis, R. C. Jaklevic, and W. Shen. Effects of surface features upon the Au(111) surface state local density of states studied with scanning tunneling spectroscopy. *Journal of Vacuum Science & Technology B: Microelectronics and Nanometer Structures Processing, Measurement, and Phenomena*, 9(2):891–896, Mar. 1991. ISSN 1071-1023. doi:10.1116/1.585490. → page 74

[130] G. Grüner. *Density waves in solids*. CRC Press, 2018. ISBN 0-429-96956-2. → page 77

[131] R. E. Peierls. *Quantum theory of solids*. Clarendon Press, 1956. → pages 77, 100, 101

[132] J. Kröger. Electron–phonon coupling at metal surfaces. *Reports on Progress in Physics*, 69(4):899–969, Mar. 2006. ISSN 0034-4885. doi:10.1088/0034-4885/69/4/R02. → pages 77, 78

[133] D. E. Moncton, J. D. Axe, and F. J. DiSalvo. Neutron scattering study of the charge-density wave transitions in $2h - \mathrm{Tase}_2$ and $2h - \mathrm{Nbse}_2$. *Phys. Rev. B*, 16:801–819, Jul 1977. doi:10.1103/PhysRevB.16.801. URL https://link.aps.org/doi/10.1103/PhysRevB.16.801. → page 77

[134] J. Tranquada, B. Sternlieb, J. Axe, Y. Nakamura, and S. Uchida. Evidence for stripe correlations of spins and holes in copper oxide superconductors. *nature*, 375(6532):561–563, 1995. → page 77

[135] C. Chamon. Solitons in carbon nanotubes. *Physical Review B*, 62(4): 2806–2812, July 2000. doi:10.1103/PhysRevB.62.2806. URL https://link.aps.org/doi/10.1103/PhysRevB.62.2806. Publisher: American Physical Society. → page 78

[136] C.-Y. Hou, C. Chamon, and C. Mudry. Electron Fractionalization in Two-Dimensional Graphenelike Structures. *Physical Review Letters*, 98(18):186809, May 2007. doi:10.1103/PhysRevLett.98.186809. URL https://link.aps.org/doi/10.1103/PhysRevLett.98.186809. Publisher: American Physical Society. → page 78

[137] O. V. Gamayun, V. P. Ostroukh, N. V. Gnezdilov, I. Adagideli, and C. W. J. Beenakker. Valley-momentum locking in a graphene

superlattice with Y-shaped Kekulé bond texture. *New Journal of Physics*, 20(2):023016, 2018. ISSN 1367-2630. doi:10.1088/1367-2630/aaa7e5. URL http://stacks.iop.org/1367-2630/20/i=2/a=023016. → pages 79, 82

[138] L.-H. Wu and X. Hu. Topological properties of electrons in honeycomb lattice with detuned hopping energy. *Scientific reports*, 6: 24347; doi: 10.1038/srep24347, 2016. → page 79

[139] V. V. Cheianov, V. I. Fal'ko, O. Syljuåsen, and B. L. Altshuler. Hidden Kekulé ordering of adatoms on graphene. *Solid State Communications*, 149(37):1499–1501, Oct. 2009. ISSN 0038-1098. doi:10.1016/j.ssc.2009.07.008. → pages 80, 81, 89, 96, 98, 102, 104

[140] V. V. Cheianov, O. Syljuåsen, B. L. Altshuler, and V. Fal'ko. Ordered states of adatoms on graphene. *Physical Review B*, 80(23):233409, Dec. 2009. doi:10.1103/PhysRevB.80.233409. → pages 80, 81

[141] S. Kopylov, V. Cheianov, B. L. Altshuler, and V. I. Fal'ko. Transport anomaly at the ordering transition for adatoms on graphene. *Physical Review B*, 83(20), may 2011. doi:10.1103/physrevb.83.201401. → pages 80, 81

[142] A. C. Qu, P. Nigge, S. Link, G. Levy, T. Matthé, M. Michiardi, M. Schneider, S. Zhdanovich, U. Starke, C. Gutiérrez, and A. Damascelli. Surface engineering Kekulé density wave formation in monolayer graphene. *In preparation*, 2021. → pages 81, 84, 87, 88, 90, 93, 97, 99, 101

[143] A. Bostwick, T. Ohta, T. Seyller, K. Horn, and E. Rotenberg. Quasiparticle dynamics in graphene. *Nature Physics*, 3(1):36–40, Jan 2007. ISSN 1745-2481. doi:10.1038/nphys477. URL https://doi.org/10.1038/nphys477. → page 83

[144] I. Gierz, J. Henk, H. Höchst, C. R. Ast, and K. Kern. Illuminating the dark corridor in graphene: Polarization dependence of angle-resolved photoemission spectroscopy on graphene. *Phys. Rev. B*, 83:121408, Mar 2011. doi:10.1103/PhysRevB.83.121408. URL https://link.aps.org/doi/10.1103/PhysRevB.83.121408. → pages 83, 101

[145] M. S. Nevius, M. Conrad, F. Wang, A. Celis, M. N. Nair, A. Taleb-Ibrahimi, A. Tejeda, and E. H. Conrad. Semiconducting Graphene from Highly Ordered Substrate Interactions. *Physical*

Review Letters, 115(13):136802, Sept. 2015. doi:10.1103/PhysRevLett.115.136802. → pages 85, 86

[146] C. M. Polley, L. I. Johansson, H. Fedderwitz, T. Balasubramanian, M. Leandersson, J. Adell, R. Yakimova, and C. Jacobi. Origin of the $\ensuremath{\pi}$-band replicas in the electronic structure of graphene grown on $4H$-SiC(0001). *Physical Review B*, 99(11): 115404, Mar. 2019. doi:10.1103/PhysRevB.99.115404. → page 85

[147] M. Farjam and H. Rafii-Tabar. Energy gap opening in submonolayer lithium on graphene: Local density functional and tight-binding calculations. *Physical Review B*, 79(4):045417, Jan. 2009. doi:10.1103/PhysRevB.79.045417. URL https://link.aps.org/doi/10.1103/PhysRevB.79.045417. → page 89

[148] K. Sugawara, K. Kanetani, T. Sato, and T. Takahashi. Fabrication of Li-intercalated bilayer graphene. *AIP Advances*, 1(2):022103, Apr. 2011. doi:10.1063/1.3582814. URL https://aip.scitation.org/doi/full/10.1063/1.3582814. → page 89

[149] K. Kanetani, K. Sugawara, T. Sato, R. Shimizu, K. Iwaya, T. Hitosugi, and T. Takahashi. Ca intercalated bilayer graphene as a thinnest limit of superconducting C6Ca. *Proceedings of the National Academy of Sciences*, 109(48):19610–19613, Nov. 2012. ISSN 0027-8424, 1091-6490. doi:10.1073/pnas.1208889109. URL https://www.pnas.org/content/109/48/19610. ISBN: 9781208889109 Publisher: National Academy of Sciences Section: Physical Sciences. → page 89

[150] S.-L. Yang, J. A. Sobota, C. A. Howard, C. J. Pickard, M. Hashimoto, D. H. Lu, S.-K. Mo, P. S. Kirchmann, and Z.-X. Shen. Superconducting graphene sheets in CaC 6 enabled by phonon-mediated interband interactions. *Nature Communications*, 5 (1):3493, Mar. 2014. ISSN 2041-1723. doi:10.1038/ncomms4493. URL https://www.nature.com/articles/ncomms4493. Number: 1 Publisher: Nature Publishing Group. → page 89

[151] A. Bostwick, F. Speck, T. Seyller, K. Horn, M. Polini, R. Asgari, A. H. MacDonald, and E. Rotenberg. Observation of Plasmarons in Quasi-Freestanding Doped Graphene. *Science*, 328(5981):999–1002, May 2010. ISSN 0036-8075, 1095-9203. doi:10.1126/science.1186489. → page 92

[152] A. L. Walter, A. Bostwick, K.-J. Jeon, F. Speck, M. Ostler, T. Seyller, L. Moreschini, Y. J. Chang, M. Polini, R. Asgari, A. H. MacDonald, K. Horn, and E. Rotenberg. Effective screening and the plasmaron bands in graphene. *Physical Review B*, 84(8):085410, Aug. 2011. doi:10.1103/PhysRevB.84.085410. → page 92

[153] V. V. Cheianov and V. I. Fal'ko. Friedel Oscillations, Impurity Scattering, and Temperature Dependence of Resistivity in Graphene. *Physical Review Letters*, 97(22):226801, Nov. 2006. doi:10.1103/PhysRevLett.97.226801. → pages 98, 100

[154] S. W. Jung, S. H. Ryu, W. J. Shin, Y. Sohn, M. Huh, R. J. Koch, C. Jozwiak, E. Rotenberg, A. Bostwick, and K. S. Kim. Black phosphorus as a bipolar pseudospin semiconductor. *Nature Materials*, 19(3):277–281, Mar 2020. ISSN 1476-4660. doi:10.1038/s41563-019-0590-2. URL https://doi.org/10.1038/s41563-019-0590-2. → page 101

[155] M. D. Johannes and I. I. Mazin. Fermi surface nesting and the origin of charge density waves in metals. *Phys. Rev. B*, 77:165135, Apr 2008. doi:10.1103/PhysRevB.77.165135. URL https://link.aps.org/doi/10.1103/PhysRevB.77.165135. → pages 101, 102

[156] D. M. Basko and I. L. Aleiner. Interplay of Coulomb and electron-phonon interactions in graphene. *Physical Review B*, 77(4): 041409, Jan. 2008. doi:10.1103/PhysRevB.77.041409. URL https://link.aps.org/doi/10.1103/PhysRevB.77.041409. Publisher: American Physical Society. → page 102

[157] S. Y. Zhou, D. A. Siegel, A. V. Fedorov, and A. Lanzara. Kohn anomaly and interplay of electron-electron and electron-phonon interactions in epitaxial graphene. *Phys. Rev. B*, 78:193404, Nov 2008. doi:10.1103/PhysRevB.78.193404. URL https://link.aps.org/doi/10.1103/PhysRevB.78.193404. → page 102

[158] I. Gierz, T. Suzuki, R. T. Weitz, D. S. Lee, B. Krauss, C. Riedl, U. Starke, H. Höchst, J. H. Smet, C. R. Ast, and K. Kern. Electronic decoupling of an epitaxial graphene monolayer by gold intercalation. *Physical Review B*, 81(23):235408, June 2010. doi:10.1103/PhysRevB.81.235408. → page 110

[159] J. Warmuth, A. Bruix, M. Michiardi, T. Hänke, M. Bianchi, J. Wiebe, R. Wiesendanger, B. Hammer, P. Hofmann, and A. A. Khajetoorians. Band-gap engineering by Bi intercalation of graphene on Ir(111). *Physical Review B*, 93(16):165437, Apr. 2016. doi:10.1103/PhysRevB.93.165437. → page 110

[160] E. Monazami, L. Bignardi, P. Rudolf, and P. Reinke. Strain Lattice Imprinting in Graphene by C60 Intercalation at the Graphene/Cu Interface. *Nano Letters*, 15(11):7421–7430, Nov. 2015. ISSN 1530-6984. doi:10.1021/acs.nanolett.5b02851. → page 110

[161] V. W. Brar, Y. Zhang, Y. Yayon, T. Ohta, J. L. McChesney, A. Bostwick, E. Rotenberg, K. Horn, and M. F. Crommie. Scanning tunneling spectroscopy of inhomogeneous electronic structure in monolayer and bilayer graphene on SiC. *Applied Physics Letters*, 91 (12):122102, Sept. 2007. ISSN 0003-6951. doi:10.1063/1.2771084. → page 111

[162] J. A. Morán-Meza, J. Cousty, C. Lubin, and F. Thoyer. Understanding the STM images of epitaxial graphene on a reconstructed 6H-SiC(0001) surface: The role of tip-induced mechanical distortion of graphene. *Physical Chemistry Chemical Physics*, 18(21):14264–14272, May 2016. ISSN 1463-9084. doi:10.1039/C5CP07571H. → pages 111, 112

[163] S. Fiori, Y. Murata, S. Veronesi, A. Rossi, C. Coletti, and S. Heun. Li-intercalated graphene on SiC(0001): An STM study. *Physical Review B*, 96(12):125429, Sept. 2017. doi:10.1103/PhysRevB.96.125429. → pages 111, 119

[164] P. Mallet, F. Varchon, C. Naud, L. Magaud, C. Berger, and J.-Y. Veuillen. Electron states of mono- and bilayer graphene on SiC probed by scanning-tunneling microscopy. *Physical Review B*, 76(4):041403, July 2007. doi:10.1103/PhysRevB.76.041403. → page 111

[165] U. Starke and C. Riedl. Epitaxial graphene on SiC(0001) and SiC$(000\bar{1}$): From surface reconstructions to carbon electronics. *Journal of Physics: Condensed Matter*, 21(13):134016, Mar. 2009. ISSN 0953-8984. doi:10.1088/0953-8984/21/13/134016. → page 111

[166] K. Yagyu, T. Tajiri, A. Kohno, K. Takahashi, H. Tochihara, H. Tomokage, and T. Suzuki. Fabrication of a single layer graphene by

copper intercalation on a SiC(0001) surface. *Applied Physics Letters*, 104(5):053115, Feb. 2014. ISSN 0003-6951, 1077-3118. doi:10.1063/1.4864155. → pages 119, 122, 123, 127

[167] M. Sicot, Y. Fagot-Revurat, B. Kierren, G. Vasseur, and D. Malterre. Copper intercalation at the interface of graphene and Ir(111) studied by scanning tunneling microscopy. *Applied Physics Letters*, 105(19): 191603, Nov. 2014. ISSN 0003-6951. doi:10.1063/1.4901165. → pages 119, 127

[168] M. Omidian, N. Néel, E. Manske, J. Pezoldt, Y. Lei, and J. Kröger. Structural and local electronic properties of clean and Li-intercalated graphene on SiC(0001). *Surface Science*, 699:121638, Sept. 2020. ISSN 0039-6028. doi:10.1016/j.susc.2020.121638. → page 119

[169] Thermo Scientific. Thermo Scientific XPS: Knowledge Base, 2021. → page 119

[170] AlfaVakuo e.U. Personal communications, 2021. → page 119

[171] S. Forti, A. Stöhr, A. A. Zakharov, C. Coletti, K. V. Emtsev, and U. Starke. Mini-Dirac cones in the band structure of a copper intercalated epitaxial graphene superlattice. *2D Materials*, 3(3): 035003, July 2016. ISSN 2053-1583. doi:10.1088/2053-1583/3/3/035003. → pages 122, 127

[172] C. Xia, L. I. Johansson, A. A. Zakharov, L. Hultman, and C. Virojanadara. Effects of Al on epitaxial graphene grown on 6H-SiC(0001). *Materials Research Express*, 1(1):015606, Mar. 2014. ISSN 2053-1591. doi:10.1088/2053-1591/1/1/015606. → page 122

[173] S. Watcharinyanon, L. I. Johansson, C. Xia, J. Ingo Flege, A. Meyer, J. Falta, and C. Virojanadara. Ytterbium Intercalation of Epitaxial Graphene Grown on Si-Face SiC. *Graphene*, 02(02):66–73, 2013. ISSN 2169-3439, 2169-3471. doi:10.4236/graphene.2013.22010. → page 122

[174] L. Daukiya, M. N. Nair, S. Hajjar-Garreau, F. Vonau, D. Aubel, J. L. Bubendorff, M. Cranney, E. Denys, A. Florentin, G. Reiter, and L. Simon. Highly n -doped graphene generated through intercalated terbium atoms. *Physical Review B*, 97(3):035309, Jan. 2018. ISSN 2469-9950, 2469-9969. doi:10.1103/PhysRevB.97.035309. → page 123

[175] F. Schmitt, P. S. Kirchmann, U. Bovensiepen, R. G. Moore, L. Rettig, M. Krenz, J.-H. Chu, N. Ru, L. Perfetti, D. H. Lu, M. Wolf, I. R. Fisher, and Z.-X. Shen. Transient Electronic Structure and Melting of a Charge Density Wave in TbTe3. *Science*, 321(5896):1649–1652, Sept. 2008. ISSN 0036-8075, 1095-9203. doi:10.1126/science.1160778. → page 129

[176] F. Schmitt, P. S. Kirchmann, U. Bovensiepen, R. G. Moore, J.-H. Chu, D. H. Lu, L. Rettig, M. Wolf, I. R. Fisher, and Z.-X. Shen. Ultrafast electron dynamics in the charge density wave material TbTe3. *New Journal of Physics*, 13(6):063022, June 2011. ISSN 1367-2630. doi:10.1088/1367-2630/13/6/063022. → page 129

[177] D. L. Bergman. Realization of a vortex in the Kekule texture of molecular graphene at a Y junction where three domains meet. *Physical Review B*, 87(3):035422, Jan. 2013. doi:10.1103/PhysRevB.87.035422. URL https://link.aps.org/doi/10.1103/PhysRevB.87.035422. Publisher: American Physical Society. → page 130

Appendix A

ARPES data processing

A.1 Angle & energy corrections

This section briefly describes the corrections performed on the ARPES data in Chapter 5. For each combination of energy range, lens mode, and analyzer entrance slit used, two additional data sets are collected: one through a slit array, and the other on a polycrystalline gold sample.

The raw detector data is recorded as a function of electron kinetic energy and pixel number. To convert the pixel number to an angle and correct for distortions, a pattern of narrow slits spaced 1 mm apart is inserted before the analyzer lens, producing bright lines at the detector (Figure A.1(a)). Images are corrected such that the lines are straight in kinetic energy and spaced 1.8° apart in angle (Figure A.1(b)).

The gold data is used to convert the kinetic energy coordinate to binding energy (Figure A.2). First, it is angle-corrected as above (Figure A.2(b)). Next, the Fermi level is fit to the Fermi function convolved with a Gaussian (for resolution effects) at each angle. The position of the Fermi level as a function of angle is fitted to a third-degree polynomial, which is then used to straighten the Fermi level in angle and shift it to zero binding energy (Figure A.2(c)). For metallic samples (i.e. not gapped at the Fermi level), the actual data set can be used for this correction as well.

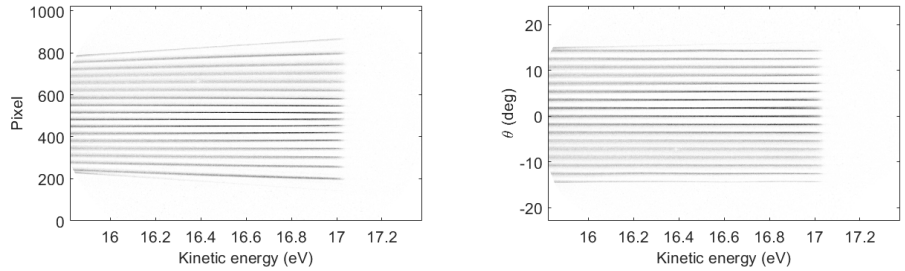

(a) **(b)**

Figure A.1: ARPES angle correction. **(a)** Raw image of the slit array on the detector. **(b)** Image of the slit array after angle correction.

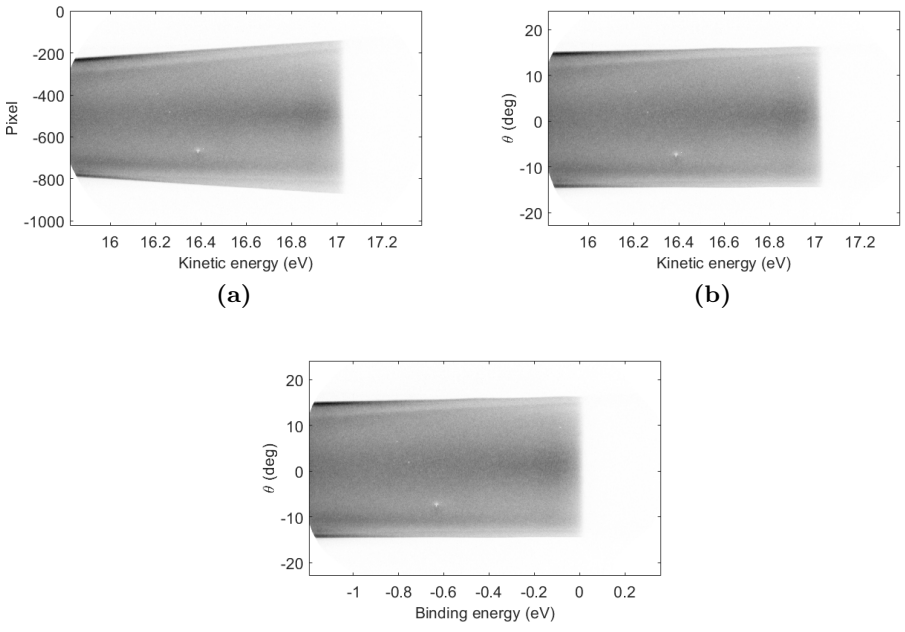

(a) **(b)**

(c)

Figure A.2: ARPES energy correction. **(a)** Raw data from the polycrystalline gold sample on the detector. **(b)** Gold data after angle correction. **(c)** Gold data after angle and energy correction.

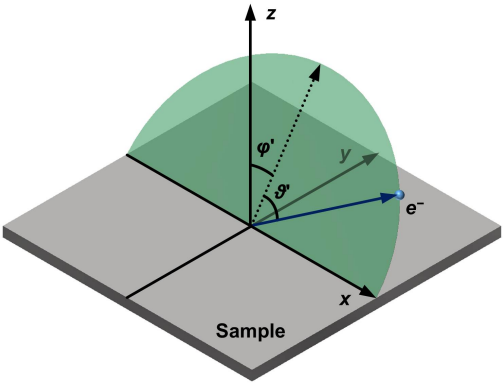

Figure A.3: ARPES manipulator geometry. In the ARPES experiments described in this thesis, the angular coordinates used are different from those in the polar coordinate system. Here, the green semicircle indicates the plane formed by the sample trajectory (dark blue arrow) and the x axis. φ' is the angle between this plane and the z axis, and ϑ' is the angle between the sample trajectory and the projection of the z axis on this plane (dotted arrow).

A.2 Angle-to-momentum conversion

Typically, the angle-to-momentum conversion for ARPES is described in terms of polar coordinates with respect to the sample surface normal as in Section 3.1:

$$k_x = \frac{1}{\hbar}\sqrt{2mE_{kin}}\,\sin\varphi\,\cos\vartheta \tag{A.1}$$

$$k_y = \frac{1}{\hbar}\sqrt{2mE_{kin}}\,\sin\varphi\,\sin\vartheta \tag{A.2}$$

$$k_z = \frac{1}{\hbar}\sqrt{2mE_{kin}}\,\cos\varphi \tag{A.3}$$

where φ and ϑ are the azimuthal and polar angles of the emitted electron, respectively. For real sample manipulators, however, it is easier to use a different set of angular coordinates (φ', ϑ'), as shown in Figure A.3.

In these coordinates, the following conversion is used instead:

$$k_x = \frac{1}{\hbar}\sqrt{2mE_{kin}}\,\sin\vartheta' \tag{A.4}$$

$$k_y = \frac{1}{\hbar}\sqrt{2mE_{kin}}\,\cos\vartheta'\,\sin\varphi' \tag{A.5}$$

$$k_z = \frac{1}{\hbar}\sqrt{2mE_{kin}}\,\cos\vartheta'\,\cos\varphi'. \tag{A.6}$$

This angle-to-momentum conversion was used for all of the ARPES data presented in this thesis.